UNIVERSITY OF CALIFORNIA SAN DIEGO

Adding new ingredients to the recipe of plasma soup: stochasticity, toroidicity, and nonlocality

A dissertation submitted in partial satisfaction of the
requirements for the degree Doctor of Philosophy

in

Physics

by

Mingyun Cao

Committee in charge:

Professor Patrick H. Diamond, Chair
Professor Daniel P. Arovas
Professor Michael L. Norman
Professor George R. Tynan

2025

The Dissertation of Mingyun Cao is approved, and it is acceptable in quality and form for publication on microfilm and electronically.

University of California San Diego

2025

TABLE OF CONTENTS

LIST OF FIGURES

LIST OF TABLES

ACKNOWLEDGEMENTS

First and foremost, I would like to express my deepest gratitude to my advisor, Prof. Patrick H. Diamond. He was the one who led me into the field of magnetic confinement fusion. His meticulously prepared courses laid a solid foundation for my understanding of plasma theory. Under his guidance, I have gained a much deeper appreciation for the process of scientific research and have gradually transformed from a student into an independent researcher. I am especially thankful for Professor Diamond's rigorous feedback on my papers, abstracts, and slides, which significantly improved my academic writing and presentation skills. Although he was sometimes demanding, his pursuit of perfection is something I will aspire to throughout my life.

I am deeply grateful to my parents, Yijun Cao and Yingxia Xu. I have been away from home since middle school, and eventually came to the United States to pursue my Ph.D. I sincerely thank them for their unwavering support and understanding throughout this journey, and for always being there to listen when I needed to share my struggles. It is my greatest fortune to have parents like you.

I would also like to thank my girlfriend, Qianqian Zhang, for her emotional support during times of uncertainty. Over the past few years of our long-distance relationship, we have both worked hard to sustain and nurture our bond. Although we were not physically together, we created many beautiful memories together. Through mutual encouragement and growth, we have become better versions of ourselves.

My heartfelt thanks also go to the other members of my dissertation committee — Prof. Daniel P. Arovas, Prof. Michael L. Norman, and Prof. George R. Tynan — for their guidance and support throughout my Ph.D.

Finally, I want to thank my office mate, Fredy Ramirez, for his help and companionship. Over the past few years, we have faced many challenges together and shared many unforgettable moments.

Chapter 1, in full, is a reprint of the material as it appears in *Plasma Physics and*

Controlled Fusion 64(3):035016 (2022). Cao, Mingyun; Diamond, P.H., IOP Publishing, 2022. The dissertation author was the primary investigator and author of this paper.

Chapter 2, in full, is a reprint of the material as it appears in *Nuclear Fusion* 64(3):036003 (2024). Cao, Mingyun; Diamond, P.H., IOP Publishing, 2024. The dissertation author was the primary investigator and author of this paper.

Chapter 3, in full, is a reprint of the material as it appears in *Physical Review Letters* 134:235101 (2025). Cao, Mingyun; Diamond, P.H., American Physical Society, 2025. The dissertation author was the primary investigator and author of this paper.

VITA

2020	B.S. in Physics, Shanghai Jiao Tong University
2020–2021	Teaching Assistant, University of California, San Diego
2021–2025	Graduate Student Researcher, University of California, San Diego
2022	C.Phil. in Physics, University of California, San Diego
2025	Ph.D. in Physics, University of California, San Diego

PUBLICATIONS

M. Cao, P.H. Diamond. Physics of core-edge coupling by inward turbulence propagation. Physical Review Letters. 2025 Jun 11;134:235101.

M. Cao, P.H. Diamond. Quasi-mode evolution in a stochastic magnetic field. Nuclear Fusion. 2024 Jan 24;64(3):036003.

M. Cao, P.H. Diamond. Instability and turbulent relaxation in a stochastic magnetic field. Plasma Physics and Controlled Fusion. 2022 Feb 7;64(3):035016.

M.A. Malkov, I.V. Moskalenko, P.H. Diamond, M. Cao. Very local impact on the spectrum of cosmic-ray nuclei below 100 TeV. Advances in Space Research. 2024 Nov 1;74(9):4264-75.

T. Long, P.H. Diamond, R. Ke, Z. Chen, M. Cao, X. Xu, M. Xu, R. Hong, W. Tian, J. Yuan, Y. Liu. On how structures convey non-diffusive turbulence spreading. Nuclear Fusion. 2024 May 3;64(6):064002.

T. Long, P.H. Diamond, R. Ke, Z. Chen, X. Xu, W. Tian, R. Hong, M. Cao, Y. Liu, M. Xu, L. Wang. The role of shear flow collapse and enhanced turbulence spreading in edge cooling approaching the density limit. Nuclear Fusion. 2024 Apr 25;64(6):066011.

P.H. Diamond, R. Singh, T. Long, R. Hong, R. Ke, Z. Yan, M. Cao, G.R. Tynan. How the birth and death of shear layers determine confinement evolution: from the L$\rightarrow$ H transition to the density limit. Philosophical Transactions of the Royal Society A. 2023 Feb 20;381(2242):20210227.

W. Guo, M. Jiang, P.H. Diamond, C.C. Chen, M. Cao, H. Li, T. Long. Theory of mean E×B shear in a stochastic magnetic field: ambipolarity breaking and radial current. Plasma Physics and Controlled Fusion. 2022 Oct 18;64(12):124001.

ABSTRACT OF THE DISSERTATION

Adding new ingredients to the recipe of plasma soup: stochasticity, toroidicity, and nonlocality

by

Mingyun Cao

Doctor of Philosophy in Physics

University of California San Diego, 2025

Professor Patrick H. Diamond, Chair

In this dissertation, we advance the theoretical framework of plasma turbulence by introducing stochasticity, toroidicity, and nonlocality.

In Chapter 1, an analysis of instability dynamics in a stochastic magnetic field is presented for the case of the resistive interchange mode. Small-scale convective cells are driven by the beat of the large-scale test mode and small-scale magnetic perturbations. In turn, these cells promote the turbulent mixing of the large-scale mode. A non-trivial correlation develops between the magnetic perturbations and the cells, indicating that turbulence "locks on" to the ambient stochasticity. It is also shown that the net effect of the stochastic magnetic field is to slow down the mode growth through magnetic braking, enhanced turbulent mixing, and electrostatic

scattering.

In Chapter 2, we present another multi-scale model of quasi-mode dynamics in a stochastic magnetic field. The resemblance between a quasi-mode and a ballooning mode in the mode structure enables us to obtain useful insights into how toroidicity affects the plasma dynamics in a background stochastic magnetic field. Owning to the broader mode structure of the quasi-mode, several results from Chapter 1 are modified. The turbulent viscosity and turbulent diffusivity produced by small-scale convective cells are found to be larger. A new mechanism for the stabilization of instabilities by ambient stochasticity is discovered—i.e., via a reduction in the effective drive.

Recent experiments observed that regular, intense gradient relaxation events produced blobs and voids in pairs close to the separatrix. While blobs propagate outward and detach from the bulk plasma, voids move inward, and so stir the core plasma. In Chapter 3, we demonstrate that the Cherenkov emission of drift waves from voids can lead to substantial inward turbulent spreading. This nonlocal effect results in a broad turbulent layer of width $\sim 100\,\rho_s$, for typical parameters. The model shows promise to resolve several questions surrounding the shortfall problem and the enhanced turbulence in the edge-core coupling region in tokamaks.

Introduction

With the development of human civilization, the demand for energy has been increasing rapidly. Especially in recent years, with the rise of emerging technologies, such as artificial intelligence, the energy consumption has further increased. To address the issues of climate change and energy shortage, we need a reliable, sustainable and clean new energy source. The power of nuclear fusion has the potential to meet all these demands. Let's take deuterium-tritium fusion (DTF) as an example, whose reaction equation is

$$ {}^{2}_{1}\mathrm{D} + {}^{3}_{1}\mathrm{T} \rightarrow {}^{4}_{2}\mathrm{He} + {}^{1}_{0}\mathrm{n}. \tag{1} $$

In DTF, a deuterium nucleus ($^{2}_{1}$D) merges with a tritium nucleus ($^{2}_{1}$T) into a helium-4 nucleus ($^{4}_{2}$He) and a neutron ($^{1}_{0}$n). One fact about DTF is that the mass of its products is slightly less than that of its reactants. According to the mass-energy equivalence formula

$$ E = mc^2, \tag{2} $$

even a tiny mass defect implies a huge release of energy, as $c^2 \approx 9.0 \times 10^{16}$ J/kg is a big number. It has been calculated that 1 gram of DTF fuel can provide as much energy as 1 ton of coal [1]. On the top of its high energy density, fusion energy also has the advantage that its fuels are abundant on Earth. The mass density of deuterium is around 33 g/m^3 in seawater. Regarding tritium, although it hardly exist in nature, it can be bred from the nuclear reaction between lithium-6 ($^{6}_{3}$Li) and neutron. In seawater, the mass density of lithium is about $0.1 - 0.2$ g/m^3 [2],

of which the relative abundance of lithium-6 is 7.5%. The reserves of deuterium and lithium in seawater are enough to supply energy to humanity for millions of years [3]. Furthermore, as DTF in principle does not involve long-lived nuclear waste and carbon dioxide, fusion energy is more environment-friendly compared to fission energy and fossil energy [4].

However, heavy is the head that wears the crown. Since the first fusion reaction was created in a laboratory in the 1930s [5], people have spent nearly a century striving to harness it as a viable energy source. However, up to now, a fusion reactor has still not been built. The main difficulty lies in the fact that the temperature required for the fusion reaction is extremely high. Strong force, as the underlying mechanism for fusion, is a short-range interaction. This means that two nuclei need to be close enough to fuse together. As they approach each other, since both nuclei are positively charged, there is a repulsive electromagnetic force between them that prevents them from getting closer. This is the so-called Coulomb barrier. To overcome this barrier, the only way is to give nuclei a sufficiently high initial velocity, i.e., to heat the fusion fuels to a high enough temperature. Even for the easiest DTF, this temperature is as high as 10 keV ($\sim$ 100 million degrees)! At such a high temperature, the fusion fuel will be fully ionized into plasma, which is composed of positively charged nuclei and negatively charged electrons. Plasma is also referred to as the fourth state of matter. Obviously, there is no material on Earth that can be used to construct a "furnace" for fusion plasmas.

0.1 Magnetic confinement fusion

The goal of controlled fusion is to achieve the self-sustained burning (fusion power $\geq$ loss power) of fusion fuels in the reactor. This requires us to confine the hot plasma of a certain density in a certain space for a certain period of time. Quantitatively speaking, the triple product of plasma density n, plasma temperature T, and energy confinement time τ_E must be greater than a threshold value. This is called the Lawson criterion. Especially, for DTF, Lawson criterion

demands

$$nT\tau_E \geq 3 \times 10^{21} \text{ keV s/m}^3. \tag{3}$$

As a tangible container is unrealistic, we need to consider building an intangible one instead. We can take advantage of the characteristic that plasma is composed of charged particles. One observation is that charged particles will orbit around the magnetic field lines, i.e., the cyclotron motion. Therefore, in magnetic fields, While charges particle can still stream freely in the direction parallel to magnetic field lines, their movement in the direction perpendicular to the magnetic field lines is restricted. Therefore, in principle, if the configuration of the magnetic field is ingenious enough, fusion plasmas will be confined in the field for a long time. This is the basic idea of magnetic confinement fusion. Based on this principle, many experimental schemes for magnetic confinement fusion have been proposed. Among them, the tokamak is undoubtedly the most successful one.

Tokamak, which stands for "**to**roidal **cha**mber with **ma**gnetic **c**oils", was invented by Anderi Sakharov and Igor Tamm in 1951. As illustrated in figure 1, the shape of a tokamak is a torus, resembling a "doughnut". The magnetic field in a tokamak mainly consists of a strong toroidal magnetic field generated by toroidal field coils and a poloidal magnetic field excited by toroidal plasma electric current. Thus the field lines of the total magnetic field are helices winding around the device. The tokamak holds the record for the highest fusion triple product. In Joint European Torus (JET), the triple product reached 4.7×10^{20} keV s/m^3, which is still one order of magnitude lower than what the Lawson criterion requires, but is at least one order of magnitude higher than the records in other types of fusion devices [6]. In this light, the first fusion device achieving self-sustained burning is very likely to be a tokamak.

0.2 Transport in tokamaks

Because of collisions between particles, the plasma confinement in tokamaks is not perfect, yielding a finite energy confinement time τ_E. Compared to other engineering parameters,

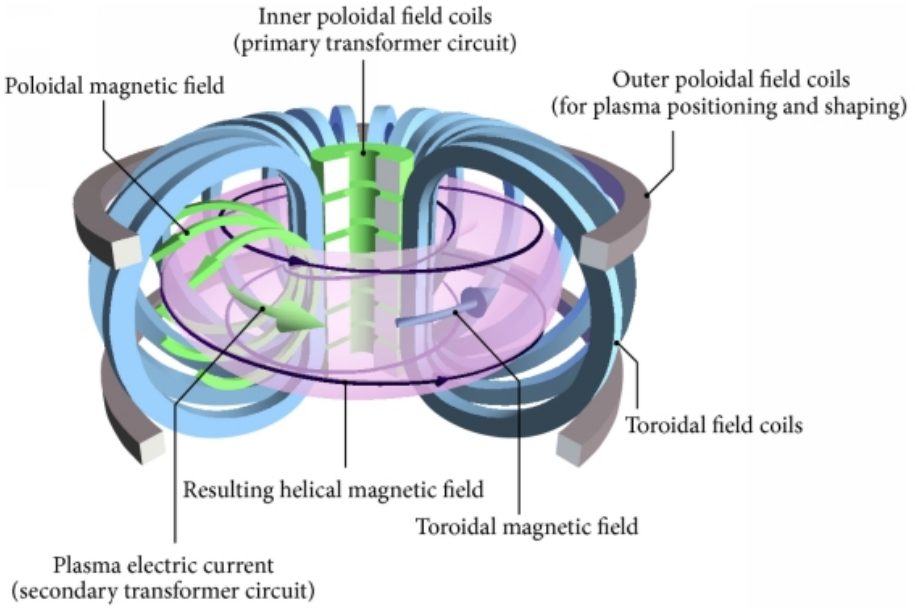

Figure 1. The schematic diagram of tokamaks. Image courtesy of EUROfusion.

τ_E is the highest leverage parameter for capital cost of fusion reactors [7]. As a result, improving the confinement performance of the device has long been the primary task in the field of magnetic confinement fusion.

0.2.1 Anomalous transport

If we approximate the migration of the plasmas from the core to the boundary of the device as a diffusion process, then τ_E will be inversely proportional to diffusivity D, i.e.,

$$\tau_E = \frac{a^2}{D}, \tag{4}$$

where a is the minor radius of the tokamak (the radius of the poloidal cross section). For an electron, the step size and waiting time of its random walk is the electron gyroradius ρ_e and the reciprocal of the electron-ion collision rate $1/\nu_{ei}$, respectively. The resulting scaling of the diffusivity is

$$D_c = \rho_e^2 \nu_{ei} = c_s \rho_s \frac{\nu_{ie}}{\omega_{ci}}, \tag{5}$$

where $c_s = (T_e/m_i)^{1/2}$ is the ion sound speed (T_e is the electron temperature, m_i is the ion mass), $\omega_{ci} = |e|B_0/m_i$ is the ion gyrofrequency (B_0 is the mean magnetic field in the device), $\rho_s = c_s/\omega_{ci}$ is the ion sound speed gyroradius, and ν_{ie} is the ion-electron collision rate. D_c is named as classical diffusion coefficient. As $\rho_e \propto 1/B_0$, it follows that $D_c \propto 1/B_0^2$. If we take into consideration the toroidal shape of tokamaks, the classical diffusivity will be enhanced by a factor of $(1+q^2)$ (in the collisional regime), yielding the neoclassical diffusion coefficient D_{neo} [8]. Here q is called safety factor and is usually around $3-4$. However, in the early days of magnetic confinement fusion development, what people actually obtained in their machines was Bohm diffusivity, which scales as

$$D_B \sim c_s \rho_s. \tag{6}$$

As a comparison to equation 5, D_B is much larger than D_c by a factor of ω_{ci}/ν_{ie}. And the fact that $D_B \propto 1/B_0$—instead of $1/B_0^2$—almost sentences magnetic confinement fusion to death, as it prevents achieving long enough τ_E with a feasible magnetic field. It was not until the 1960s that Bohm diffusion is not an inexorable law and could be overturned in tokamaks [9]. The actual transport beyond the neoclassical prediction is given the name "anomalous transport".

It has been well recognized that the anomalous transport should be attributed to plasma microturbulence [10]. According to mixing length model, the scaling of the turbulent diffusivity could be approximated as the product of the characteristic fluctuating velocity $\tilde{v}$ and the mixing length l_{mix} of the turbulence, i.e., [11]

$$D_t \sim \tilde{v} l_{\text{mix}}. \tag{7}$$

In fusion plasmas, a sensible approximation of $\tilde{v}$ is the electron diamagnetic drift velocity $v_* = c_s \rho_s / L_n$, where L_n is the characteristic length of the mean density gradient. As for l_{mix}, it must lie between ρ_s and L_n, and can thus be denoted as $L_n(\rho_s/L_n)^\alpha$ $(0 < \alpha < 1)$. As a result,

we obtain

$$D_t \sim c_s \rho_s \left(\frac{\rho_s}{L_n} \right)^{\alpha}. \tag{8}$$

Clearly, when $\alpha = 0$, the diffusivity given in equation 8 becomes the Bohm diffusivity; when $\alpha = 1$, a new scaling called gyro-Bohm emerges as $D_{gB} \sim v_* \rho_s$, by which the B^{-2} rule is restored. In practice, the observed diffusivity is between D_B and D_{gB}.

Due to the advantage of tokamak over other types of fusion devices in confinement performance, tokamak has become the primary candidate for future magnetic confinement fusion reactors. In the 1970s, ion temperature of 6.5 keV was achieved in a tokamak by using neutral beam injection [12]. But disappointingly, it emerged that the energy confinement time τ_E decreased with increasing heating power [13]. The development of controlled fusion once again hit a low point.

0.2.2 Discovery of the H-mode

Fortunately, in 1982, a "miracle" happened. On the tokamak ASDEX, it was discovered that the energy confinement time was significantly enhanced by a factor of 2 when the input neutral beam heating power exceeded a threshold value [14]. This new operating regime is termed high-confinement mode (H-mode) to distinguish it from the previous low-confinement mode (L-mode). Immediately, this exciting result stimulated extensive research on the H-mode. Nowadays, it has been widely acknowledged that the spontaneous transition from L-mode to H-mode is caused by the suppression of the edge turbulence by zonal flow [15].

In magnetically confined plasmas, zonal flow is a mesoscopic, poloidally and toroidally symmetric shear flow in the poloidal direction, as illustrated in figure 2. The mechanism of zonal flow suppressing the anomalous transport is eddy tilt. Eddies, also known as convective cells are present in plasma turbulence. Inside these eddies, plasma can be convected efficiently. As shown in figure 3, with the presence of a shear flow, eddies will be tilted. The radial extent of eddies, which can be regarded as the step size of the diffusion process, becomes narrower,

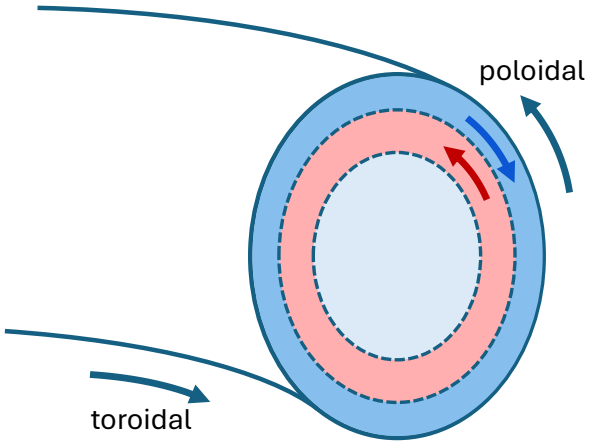

Figure 2. Illustration of the zonal flow in magnetically confined plasmas.

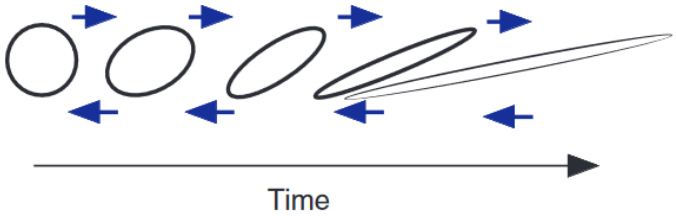

Figure 3. Twist of convective cells by a shear flow. Note that the radial extent of eddies is decreased, thereby suppressing the plasma transport. Reprinted from [16].

hence reducing the effective transport. According to this picture, the emergence of the H-mode is due to a sudden increase in the magnitude of zonal flows at the boundary region when $P > P_{LH}$. This amplified zonal flow serves as an edge transport barrier (ETB), which notably improves the confinement performance.

0.2.3 Zonal flow generation: the predator-prey model

Since its discovery, H-mode has captured widespread attention. Numerous studies attempted to figure out the mechanism of L-H transition. So far, the most accepted theory is the amplification of zonal flows by modulational instability of drift waves [17]. Drift wave is a collective mode driven by density gradient in magnetically confined plasmas. A more general concept of drift waves include a series of plasma modes at the scale of ion gyroradius, such as

ion temperature gradient mode (ITG), trapped electron mode (TEM), etc. The driving of zonal flows by drift waves can be formulated by the predator-prey model, in which the zonal flow is the predator and the drift wave is the prey.

In this section, the simplest model for the dynamics of drift wave–zonal flow interaction is derived from the modified Hasegawa-Mima equation. which is effectively the continuity equation for perturbed ion guiding center density n_{ig} [18], i.e.,

$$\frac{\partial}{\partial t} n_{ig} + \hat{\boldsymbol{z}} \times \nabla \varphi \cdot \nabla n_{ig} = 0. \tag{9}$$

Here $n_{ig} = n_0 + \delta n_{ig}$ (n_0 is the mean plasma density and δn_{ig} is the perturbed ion guiding center density). Since plasma is quasi-neutral, i.e., the number of positive and negative charges is equal, δn_{ig} should satisfy

$$\delta n_{ig} + n_0 \nabla_\perp^2 \varphi = \delta n_e = n_0 (\varphi - \bar{\varphi}), \tag{10}$$

where φ is the electrostatic potential nondimensionalized by $T_e/|e|$, $\bar{\varphi} = \int_0^{L_y} \varphi \mathrm{d}y / L_y$ is the zonally-averaged electrostatic potential. The second term on the L.H.S. stands for the density of the polarization charge. The R.H.S. is the density of adiabatic electrons. For simplicity, the spatial and temporal scales are nondimensionalized by ρ_s and $1/\omega_{ci}$ respectively. Plugging equation 10 into equation 9, we obtain

$$\left(\frac{\partial}{\partial t} + \hat{\boldsymbol{z}} \times \nabla \bar{\varphi} \cdot \nabla + v_* \frac{\partial}{\partial y} \right) \tilde{\varphi} - \left(\frac{\partial}{\partial t} + \hat{\boldsymbol{z}} \times \nabla \bar{\varphi} \cdot \nabla \right) \nabla_\perp^2 \varphi = 0, \tag{11}$$

where $\tilde{\varphi} = \varphi - \bar{\varphi}$, $v_* = -\nabla(\ln n_0)$ is the electron diamagnetic drift velocity. Equation 11 is the modified Hasegawa-Mima equation. By taking the zonal averaging of this equation, we obtain

$$\left(\partial_t + \hat{\boldsymbol{z}} \times \nabla \bar{\varphi} \cdot \nabla\right) \left(1 - \nabla^2\right) \tilde{\varphi} + \left(\boldsymbol{v}_* + \hat{\boldsymbol{z}} \times \nabla \nabla^2 \bar{\varphi}\right) \cdot \nabla \tilde{\varphi} = \widetilde{P} \hat{\boldsymbol{z}} \times \nabla \tilde{\varphi} \cdot \nabla \nabla^2 \tilde{\varphi}, \tag{12}$$

$$\frac{\partial}{\partial t} \nabla_\perp^2 \bar{\varphi} = -\overline{\hat{\boldsymbol{z}} \times \nabla \tilde{\varphi} \cdot \nabla \nabla^2 \tilde{\varphi}} = -\frac{\partial^2}{\partial x^2} \overline{\tilde{v}_x \tilde{v}_y} = \frac{\partial^2}{\partial x^2} \overline{\partial_y \tilde{\varphi} \partial_x \tilde{\varphi}}. \tag{13}$$

Equation 12 and equation 13 are the fluctuating and zonally-averaged components of the modified Hasegawa-Mima equation, which are responsible for the dynamics of drift waves and zonal flows, respectively. As indicated by equation 13, zonal flow is driven by the Reynolds stress $\overline{\tilde{v}_x \tilde{v}_y}$. Taylor identity is adopted in the derivation of equation 13 [19].

If we drop the self-interaction term (the R.H.S.), equation 12 becomes

$$\left(\partial_t + \hat{\boldsymbol{z}} \times \nabla \bar{\varphi} \cdot \nabla\right)\left(1 - \nabla^2\right)\tilde{\varphi} + v_* \partial_y \tilde{\varphi} = 0. \tag{14}$$

By taking the Fourier transform of equation 14 in space, we obtain [20]

$$\partial_t \tilde{\varphi}_{\boldsymbol{k}} + i\omega_{\boldsymbol{k}} \tilde{\varphi}_{\boldsymbol{k}} + \int d^2 p L_{\boldsymbol{p},\boldsymbol{k}-\boldsymbol{p}} \bar{\varphi}_{\boldsymbol{p}} \tilde{\varphi}_{\boldsymbol{k}-\boldsymbol{p}}, \tag{15}$$

where $\boldsymbol{k}$ and $\boldsymbol{q}$ are the wave numbers of drift waves and zonal flows, $\omega_{\boldsymbol{k}} = k_y v_* / (1 + k_\perp^2)$ is the frequency of drift waves, and

$$L_{\boldsymbol{k_1},\boldsymbol{k_2}} = -\frac{\hat{\boldsymbol{z}} \cdot \boldsymbol{k}_1 \times \boldsymbol{k}_2}{1 + (\boldsymbol{k}_1 + \boldsymbol{k}_2)^2}\left(1 + k_2^2\right). \tag{16}$$

As drift wave turbulence is a kind of microturbulence and zonal flow is a mesoscale flow, the ordering of spatial scales is $k\rho_s \sim 1 \gg q\rho_s \sim 0.1$. By multiplying equation 15 by $\tilde{\varphi}_{-\boldsymbol{k}+\boldsymbol{q}}$, adding the resulting equation to its conjugate equation, taking the ensemble average (denoted by $\langle\rangle$) and inverse Fourier transform with respect to $\boldsymbol{q}$, and defining

$$N(\boldsymbol{x}, \boldsymbol{k}, t) = (1 + k^2)^2 \int d^2 q \langle \tilde{\varphi}_{-\boldsymbol{k}+\boldsymbol{q}} \tilde{\varphi}_{\boldsymbol{k}} \rangle \exp(i\boldsymbol{q} \cdot \boldsymbol{x}) = (1 + k^2)^2 |\varphi_{\boldsymbol{k}}|^2, \tag{17}$$

we obtain the wave-kinetic equation

$$\frac{\partial}{\partial t} N + \frac{\partial}{\partial \boldsymbol{k}}\left(\omega_{\boldsymbol{k}} + \boldsymbol{k} \cdot \bar{\boldsymbol{v}}\right) \cdot \frac{\partial}{\partial \boldsymbol{x}} N - \frac{\partial}{\partial \boldsymbol{x}}\left(\omega_{\boldsymbol{k}} + \boldsymbol{k} \cdot \bar{\boldsymbol{v}}\right) \cdot \frac{\partial}{\partial \boldsymbol{k}} N = 0. \tag{18}$$

A density modulation term $\nabla\omega_{\boldsymbol{k}} \cdot \nabla_{\boldsymbol{k}} N$ is added in the derivation. Here N is called wave action density, which is a conserved action-like invariant. When k_y is a constant, we have

$$N = (1+k^2)^2 |\varphi_{\boldsymbol{k}}|^2 \propto (1+k^2)^2 \frac{|\varphi_{\boldsymbol{k}}|^2}{\omega_*} = \frac{E_{\boldsymbol{k}}}{\omega_{\boldsymbol{k}}}, \tag{19}$$

where $\omega_* = k_y v_*$ and $E_{\boldsymbol{k}} = (1+k^2)|\varphi_{\boldsymbol{k}}|^2$ is the energy density of drift waves. This form allows us to interpret N as the "quantum number" of drift waves. Hereafter we adopt the standard expression for the wave action, i.e., $N = E_{\boldsymbol{k}}/\omega_{\boldsymbol{k}}$.

Since N is a slowly varying function of $\boldsymbol{x}$ and $\boldsymbol{k}$ (recall we take the ensemble average in the definition of N), we can further decompose it into a macroscopic component N_0, and a mesoscopic component $\bar{N}$, i.e.,

$$N = N_0 + \bar{N}. \tag{20}$$

$\bar{N}$ is the modulational response to the zonal flow $\bar{v}$. According to equation 18, $\bar{N}$ is given by

$$\bar{N}_q = -\frac{-qk_y\bar{v}_q}{\Omega - qv_g + i\gamma}\frac{\partial N_0}{\partial k_x}. \tag{21}$$

Here Ω and γ are the frequency and growth rate of $\bar{N}_q$. $v_g = d_{\boldsymbol{k}}\omega_{\boldsymbol{k}}$ and k_y are the characteristic group velocity and poloidal wave vector of drift waves. The evolution equation for N_0 is

$$\frac{\partial}{\partial t}N_0 = \frac{\partial}{\partial k_x}\left\langle k_y \partial_x \bar{v}\bar{N}\right\rangle. \tag{22}$$

Since $N = E_{\boldsymbol{k}}/\omega_{\boldsymbol{k}}$, substituting this relation into equation 21 and integrating over the wave vector of N_0, we obtain

$$\frac{d}{dt}E_0 = 2\sum_q \int \frac{\gamma}{(\Omega - qv_g)^2 + \gamma^2}\frac{q^2k_xk_y^2}{(1+k^2)^2}|\bar{v}|^2\frac{\partial N_0}{\partial k_x}d^2k. \tag{23}$$

Note that an integration-by-parts and the expression $v_g = -2k_xk_y/(1+k^2)v_*$ are used in this

derivation.

Regarding the evolution of the zonal flow, equation 13 yields

$$\frac{\partial}{\partial t} q^2 \bar{\varphi}_q = q^2 \int \frac{k_x k_y}{(1+k^2)^2} \bar{N}_q d^2 k. \tag{24}$$

By multiplying equation 24 by $\bar{\varphi}_q$, plugging into equation 21, taking the real part, and summing over q, we have

$$\frac{d}{dt} |\bar{v}|^2 = -2 \sum_q \int \frac{\gamma}{(\Omega - q v_g)^2 + \gamma^2} \frac{q^2 k_x k_y^2}{(1+k^2)^2} |\bar{v}|^2 \frac{\partial N_0}{\partial k_x} d^2 k. \tag{25}$$

Equation 23 and equation 25 together constitute the simplest dynamic model of drift wave–zonal flow interaction. Clearly, by adding up these two equations, it is evident that the total energy of drift waves and zonal flows is conserved, i.e.,

$$\frac{d}{dt} \left(E_0 + |\tilde{v}|^2 \right) = 0. \tag{26}$$

This energy conservation law implies that, when the energy of turbulence decreases, the energy of zonal flows will increase, providing a possible mechanism by which drift wave turbulence can drive zonal flows

0.3 New elements of plasma turbulence research

After decades of research, significant progress have been made in the improving confinement performance. Apart from aforementioned H-mode, good confinement has been achieved in some other advanced operating modes, such as improved-confinement mode [21], radiatively-improved mode [22], etc. Their advantages and disadvantages are summarized in table 1.

Nevertheless, it should be recognized that good confinement is not the only requirement for controlled fusion. Because there is the input of fusion fuels and the output of fusion

Table 1. Advantages and disadvantaged of some advanced operating modes for tokamaks.

advanced operating mode	advantage	disadvantage
improved-confinement mode	good energy confinement no impurity accumulation no edge-localized modes	narrow accessible window
radiatively-improved mode	stable H-mode like confinement high plasma density	impurity accumulation operational complexity
quiescent high-confinement mode	manageable heat load steady-state operation	impurity accumulation

energy, the fusion device is not an isolated system. From an engineering perspective, the plasma-wall interaction (PWI) is inevitable. This necessitates careful control of boundary conditions, particularly the heat flux on the divertor, where impurities and helium ash are exhausted. Moreover, just as coal must be heated to ignite, fusion fuels also require auxiliary heating to reach ignition. However, the available auxiliary heating power is always limited. As a consequence, good confinement is supposed to be achieved in conjunction with manageable boundary control and practical power handling. These demands motivate a deeper investigation into plasma turbulence.

Most well-known theories of plasma turbulence are set up in a slab configuration with a regular magnetic field. In these theories, plasma turbulence is conventionally modeled as an ensemble of waves. For example, the predator-prey model examines the interaction between a packet of drift waves and zonal flows. Similarly, the theory of Langmuir turbulence describes the interaction between a gas of small-scale Langmuir waves and ion acoustic waves [23]. But, these approximations do not always hold suitable. In tokamaks, the magnetic fields at the edge could become chaotic rather than regular due to externally-prescribed resonant magnetic perturbations (RMPs) [24] or intrinsically-driven edge harmonic oscillations (EHOs) [25]. Some novel phenomena, such as density pump-out [24], can only be explained when the effects of

the background stochastic magnetic field are taken into account. The toroidal geometric shape of tokamaks also plays a non-negligible role. It has been demonstrated that the toroidicity effect may have significant impacts on the mode structure and nonlinear coupling of plasma instabilities [26, 27]. In this sense, there exists a gap between complex simulations and simple models based on a slab configuration. An "intermediately-complex" theory is necessary to capture the essential physics underlying geometric effects. Last but not least, while representing turbulence as a superposition of plasma waves is analytically convenient, it is not conceptually accurate. Besides collective modes, plasma turbulence also contains mesoscopic and long-lived coherent structures known as blobs and voids [28]. The convective motions of these coherent structures cause the plasma turbulence to manifest non-local characteristics. Therefore, based on the above discussion, we need to incorporate new elements into the existing framework of plasma turbulence theory. Since plasma turbulence is often conceived as a multi-ingredient "soup", our task can be viewed as adding new ingredients to the recipe of plasma soup!

In this section, we present fundamental theories on stochastic magnetic fields, toroidicity effects and coherent structures.

0.3.1 Stochastic magnetic fields in a tokamak

As depicted in figure 1, the main magnetic field in a tokamak is composed of a toroidal magnetic field generated by toroidal field coils and a poloidal field driven by poloidal plasma current, i.e.,

$$\boldsymbol{B} = B_0\hat{\boldsymbol{\phi}} + B_\theta(r)\hat{\boldsymbol{\theta}}. \tag{27}$$

where $\hat{\boldsymbol{\phi}}$ and $\hat{\boldsymbol{\theta}}$ denote toroidal and poloidal directions, respectively. B_θ is a function of the radial coordinate r and $B_\theta \ll B_0$. The equation of the field lines is

$$\frac{rd\theta}{B_\theta} = \frac{Rd\phi}{B_0}, \tag{28}$$

where R is the major radius of the device, and ϕ and θ are toroidal and poloidal angles, respectively. From equation 28, we can define the winding rate of magnetic field lines as

$$q = \frac{d\phi}{d\theta} = \frac{rB_0}{RB_\theta}. \tag{29}$$

q is also named as safety factor. In tokamaks, the envelopes of magnetic field lines with the same winding rate form nested magnetic surfaces, also known as flux surfaces (see figure 4). Since, by definition, magnetic field lines do not cross magnetic surfaces, we have

$$\boldsymbol{B} \cdot \nabla f = 0, \tag{30}$$

where f is the magnetic flux density.

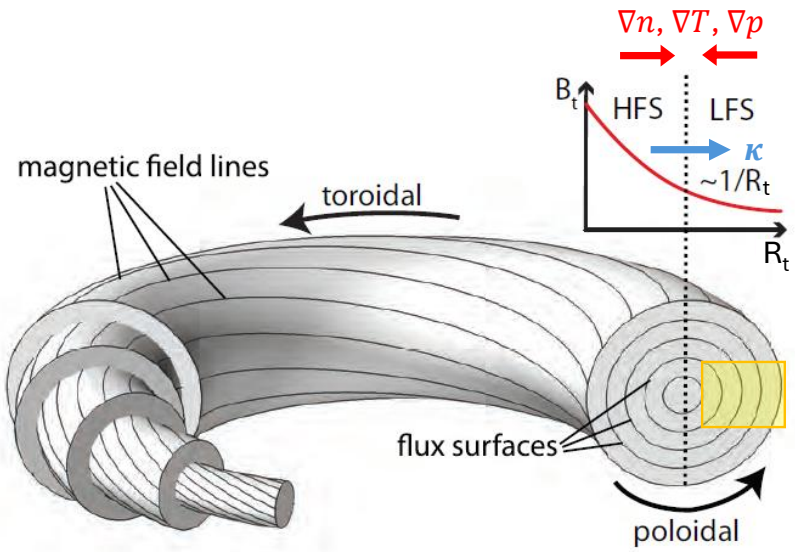

Figure 4. Nested flux surfaces (magnetic surfaces) in a tokamak. Modified from [29].

However, magnetic surfaces are not always as regular as shown in figure 4. Besides the main field, perturbed magnetic fields are also present in fusion devices. Some plasma instabilities, such as tearing modes, can generate intrinsic perturbed magnetic fields. In addition, perturbed magnetic fields may emerge as a result of external excitation. In H-mode, there are instabilities

called edge-localized modes (ELMs) [30]. ELMs release heat and particles in a quasi-periodic way, causing severe damage the device walls. In experiments, a set of external coils is often installed to drive resonant magnetic perturbations (RMPs) to mitigate or suppress ELMs. Rational (or resonant) surfaces, where q is a rational number, are susceptible to destruction by perturbed magnetic fields, giving rise to a stochastic layer. In contrast, irrational surfaces (or nonresonant surfaces), on which q is an irrational number, tend to remain well-preserved. This phenomenon can be explained by exploiting the similarity between the magnetic field and a Hamiltonian system.

In the presence of perturbed magnetic fields, the total magnetic field is written as

$$\boldsymbol{B} = B_0\hat{\boldsymbol{\phi}} + B_\theta(r)\hat{\boldsymbol{\theta}} + \tilde{\boldsymbol{B}}_\perp, \tag{31}$$

where $\tilde{\boldsymbol{B}}_\perp$ denotes the perturbed magnetic fields perpendicular to $B_0\hat{\boldsymbol{\phi}}$ and $\tilde{B}_\perp/B_0 \ll 1$. Note that the parallel perturbed field $\tilde{\boldsymbol{B}}_\parallel$ is neglected, given that it is a higher-order quantity. Substituting equation 31 into equation 30 yields

$$\frac{\partial f}{\partial z} + \boldsymbol{b}_\perp \cdot \nabla f = 0, \tag{32}$$

where $dz = Rd\phi$ and

$$\boldsymbol{b}_\perp = (B_\theta\hat{\boldsymbol{\theta}} + \tilde{\boldsymbol{B}}_\perp)/B_0 = (B_\theta/B_0)\hat{\boldsymbol{\theta}} + \tilde{\boldsymbol{b}}_\perp. \tag{33}$$

According to Maxwell's equations, the magnetic field is divergence-free, which results in

$$\nabla \cdot \boldsymbol{b}_\perp = 0. \tag{34}$$

Recall that one characteristic of a Hamiltonian system is that its phase flow $\boldsymbol{V}$ is also divergence-free, i.e.,

$$\nabla \cdot \boldsymbol{V} = 0. \tag{35}$$

Consequently, the evolution of the phase space distribution function ρ follows the Liouville equation

$$\frac{\partial \rho}{\partial t} + \boldsymbol{V} \cdot \nabla f = 0. \tag{36}$$

Apparently, equation 32 and equation 36, as well as equation 34 and equation 35, share the same mathematical structure. From this perspective, the magnetic field is effectively a Hamiltonian system, with the spatial coordinate z playing the role of time t. According to the Kolmogorov–Arnold–Moser theorem, if an integrable Hamiltonian system—such as the unperturbed magnetic field here—is subjected to a weak perturbation, resonant surfaces are destroyed while nonresonant surfaces survive. In figure 5, panels (a), (b), and (c) show zoom-ins of the yellow-shaded region in figure 4. In panel (a), the blue and brown lines represent unperturbed nonresonant and resonant surfaces. As shown in panel (b), the introduction of a weak perturbed field leads to the formation of magnetic island chains on resonant surfaces. When the magnetic perturbation is strong enough, as illustrated in panel (c), island chains located on different resonant surfaces may overlap. In the overlapping region, the field lines are no longer deterministic, but rather chaotic. This chaotic magnetic field is commonly called the stochastic magnetic field. If we restore the geometry in figure 5 from a slab to a circular shape, the variation of resonant surfaces indicates that, when the magnetic perturbations in a tokamak are sufficiently strong, a stochastic layer will be generated in the outer part of the plasma. The condition for the formation of the stochastic layer is given by the Chirikov criterion, namely

$$\sigma_{\text{Chirikov}} = \frac{\delta_1 + \delta_2}{\Delta_{12}} > 1, \tag{37}$$

where δ_1 and δ_1 are the half widths of two separate resonant surfaces and Δ_{12} denotes the distance between them.

In a stochastic magnetic field, the distance between two initially infinitesimally close

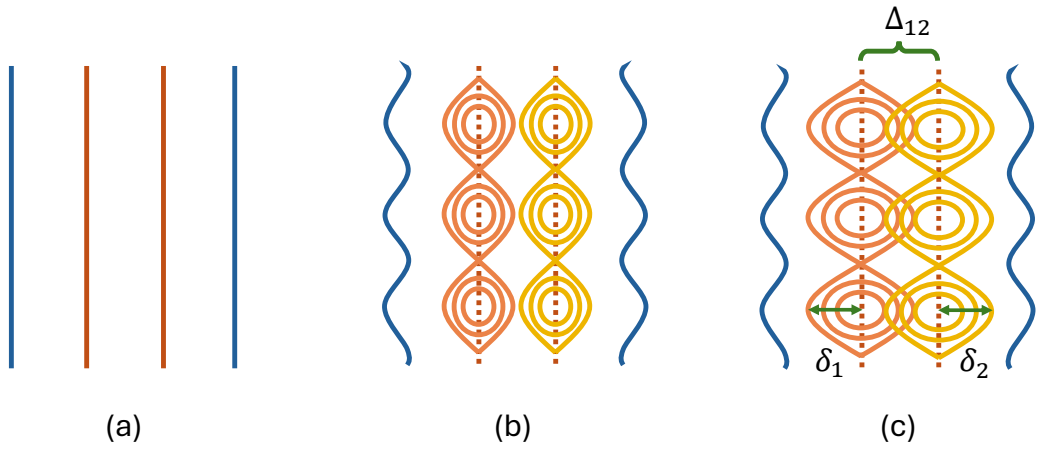

Figure 5. The destruction of resonant surfaces by magnetic perturbations: (a) no perturbed fields; (b) weak perturbed fields; (c) stronger perturbed fields.

field lines grows exponentially as they extend along the z-direction, following the relation

$$d = d_0 \exp\left(-\frac{z}{l_c}\right), \tag{38}$$

where l_c is the de-correlation length of the stochastic magnetic field. Its reciprocal, $1/l_c$, corresponds to the Lyapunov index in chaos theory. Given the fundamental difference between stochastic and regular magnetic fields, plasma dynamics must be reexamined to account for the presence of stochasticity and its impact on transport and confinement.

0.3.2 Influence of toroidicity on plasma dynamics

The most prominent feature of a tokamak must be its toroidal shape. However, many theoretical models fail to capture this aspect. For example, the theory of stochastic magnetic fields in section 0.3.1 is not based on a truly toroidal configuration. With the coordinate transformation $z = R\phi$ and the assumption of a uniform B_0, the geometry adopted there is, in fact, a periodic cylinder. As suggested in figure 4, the toroidal magnetic field in a toroidal geometry is not a constant, but instead scales as $B_0 \propto 1/R_t$, where R_t is the distance from the toroidal axis (the vertical axis at the center of the torus). As a result, the magnetic field on the inboard side of a

tokamak is stronger than that on the outboard side. The inboard side is also referred to as the high-field side (HFS), while the outboard side is called the low-field side (LFS). Concomitantly, in this configuration, the main magnetic field acquires a curvature $\boldsymbol{\kappa}$, which is directed outward from the toroidal axis. In a tokamak, thermodynamic quantities Q—such as temperature, density, and pressure— typically peak in core. Consequently, we have $\boldsymbol{\kappa}\cdot\nabla Q > 0$ on the HFS, and $\boldsymbol{\kappa}\cdot\nabla Q < 0$ on the LFS. This implies that it is easier for plasma instabilities to grow on the LFS, thereby breaking the poloidal symmetry of the system. As illustrated in figure 6, plasma instabilities tend to be concentrated on the low-field side of the torus.

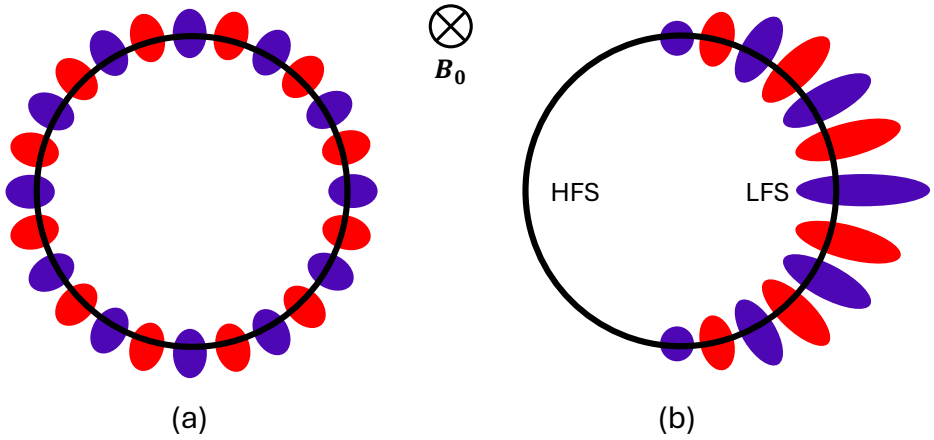

Figure 6. Illustration of the magnitude of plasma instabilities in (a) a cylindrical geometry and (b) a toroidal geometry. In the cylindrical case, the system has a poloidal symmetry. The toroidal geometry breaks this symmetry, causing the instabilities to be concentrated on the low-field side.

Toroidicity effect (or equivalently ballooning effect) can substantially modify the mode structures of plasma instabilities. Here, the drift-acoustic mode is taken as an example, whose dynamics can be described by the ion continuity equation

$$\frac{\partial}{\partial t}n + \nabla\cdot[(\boldsymbol{v}_D + \tilde{\boldsymbol{v}})n] = 0, \tag{39}$$

and the ion momentum equation in the direction parallel to the main magnetic field

$$\frac{\partial}{\partial t}\tilde{v}_{\parallel} = -\nabla_{\parallel}\varphi. \tag{40}$$

Here $\tilde{\boldsymbol{v}}$ includes the $E \times B$ drift velocity, the polarization drift velocity, and perturbed parallel velocity, i.e., $\tilde{\boldsymbol{v}} = \tilde{\boldsymbol{v}}_{E\times B} + \tilde{\boldsymbol{v}}_{pol} + \tilde{\boldsymbol{v}}_{\parallel} = -\nabla\varphi \times \hat{\boldsymbol{z}} - d_t \nabla_{\perp}\varphi + \tilde{\boldsymbol{v}}_{\parallel}$. Since the main magnetic field is nonuniform, ions also acquire a magnetic drift velocity $\boldsymbol{v_D}$, which is expressed as

$$\boldsymbol{v_D} = \left(v_{\parallel}^2 + \frac{1}{2}v_{\perp}^2\right)\omega_{ci}\boldsymbol{\kappa} \times \hat{\boldsymbol{z}} = v_D(\cos\theta\hat{\boldsymbol{\theta}} + \sin\theta\hat{\boldsymbol{r}}), \tag{41}$$

where $\kappa = 1/R$, $v_{\parallel}$ and $v_{\perp}$ are ion thermal velocities in the parallel and perpendicular directions. The Fourier expansion of φ is given as

$$\varphi = \sum_m \varphi_m(x)\exp\left[i\omega t + i(m\theta - n\phi)\right], \tag{42}$$

where integers m and n are poloidal and toroidal mode numbers, respectively. The poloidal harmonic $\varphi_m(x)$ is a spatially-localized function x. Here $x = r - r_{m,n}$ is the radial distance from the resonant surfaces where $q = m/n$. The poloidal and parallel wavenumbers are given by $k_y = m/r$ and $k_{\parallel} = -k_y x/L_s$, where L_s is the characteristic length of the magnetic shear.

By linearizing and combining equations 39 and 40, and applying the Fourier expansion of φ, the eigenmode equation for the drift-acoustic mode is derived as

$$\left[-\frac{\partial^2}{\partial x^2} + k_y^2 + \left(1 - \frac{\omega_*}{\omega}\right) - \frac{k_y^2 x^2}{L_s^2\omega^2}c_s^2\right]\varphi_m + \hat{\mathrm{T}}_1(\varphi_{m+1} + \varphi_{m-1}) + \hat{\mathrm{T}}_2(\varphi_{m+1} - \varphi_{m-1}) = 0, \tag{43}$$

where $\hat{\mathrm{T}}_1$ and $\hat{\mathrm{T}}_2$ are two differential operators proportional to v_D. As depicted in figure 2.2, poloidal harmonics with the same toroidal mode number n but different poloidal mode number m are located at different resonant surfaces. Equation 43 shows that toroidicity couples these poloidal harmonics together, resulting in a radially-extended and ballooning-like mode structure.

This broad mode structure makes the plasma transport more efficient. Therefore, toroidicity is an indispensable factor when studying plasma instabilities in stochastic magnetic fields.

0.3.3 Convective transport by coherent structures

The conventional understanding of transport in a tokamak is rooted in a local, quasi-linear description. More specifically, the relationship between fluxes and profile gradients follow a Fickian formulation, namely

$$\Gamma_Q = -D\nabla Q. \tag{44}$$

However, this diffusive description of transport is subjected to challenge by experimental observations. For instance, as reported from J-TEXT [31], if a Fickian model is used to calculate the turbulence spreading diffusivity defined as $\chi_I \equiv -\langle \tilde{v}_r \tilde{n}^2 \rangle / \partial_r \langle \tilde{n}^2 \rangle$, nonphysical singular values appear (see panel (e) in figure 7). These results imply that convective transport does exist in magnetically confined fusion plasmas. In tokamaks, coherent structures—including density blobs and density voids—could provide a mechanism for the convective transport.

The definition of blobs and voids varies across theories, simulations, and experiments. But generally, blobs and voids are plasma filaments characterized by a monopole density distribution with a peak amplitude $2-3$ times higher than the root-mean-square fluctuation level of the background plasma. Their structures are elongated along the main magnetic magnetic field, with much slower variation in the parallel direction relative to the perpendicular. Typically, the perpendicular scales of blobs and voids are on the order of 10 ρ_s, lying between the microscopic gyroradius and the macroscopic device dimensions. Hence, they are also designated as "mesoscale structures".

Regarding the formation of coherent structures, recent experimental results support the physical picture that blobs and voids are generated in pairs from edge gradient relaxation events (GREs) very close to the last closed flux surface (LCFS) [32]. As shown in figure 8, each time the edge density gradient collapses, a pair of a blob and a void is emitted. Subsequently, the blob

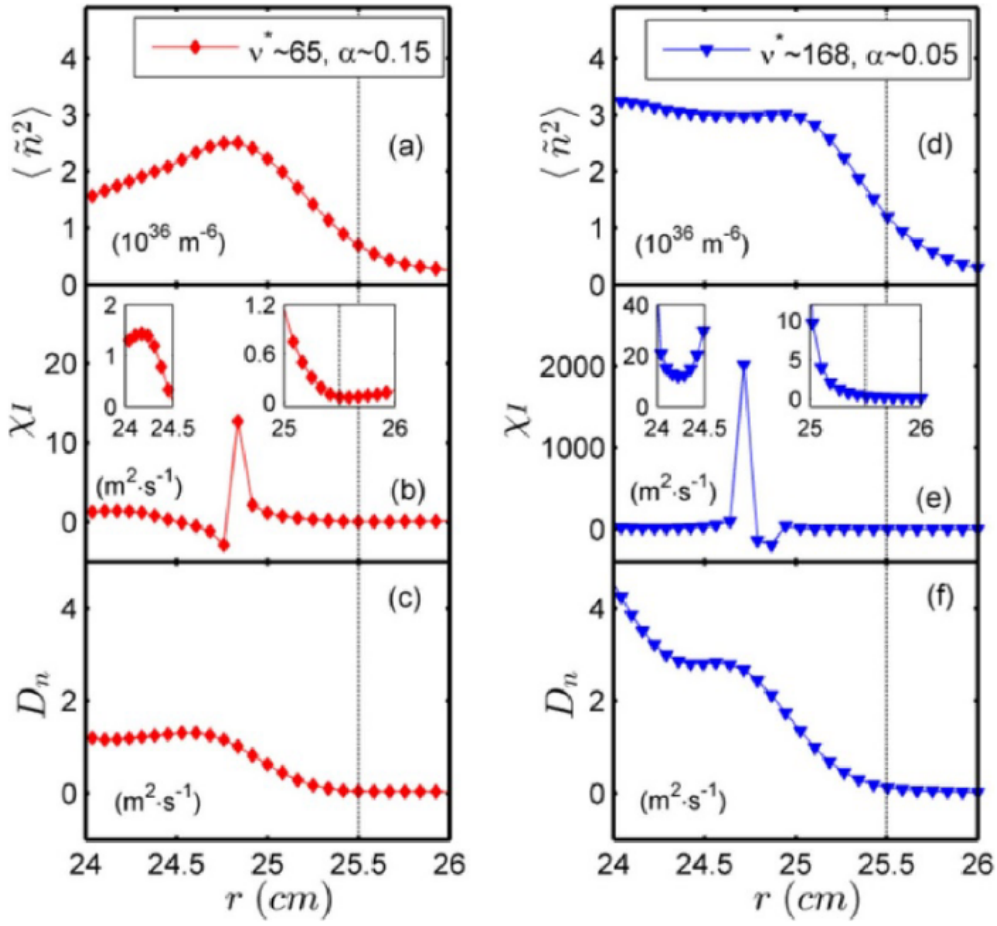

Figure 7. Measurements of turbulence intensity (a,d), turbulence spreading diffusivity (b,e), and turbulence particle diffusivity D_n (c,f) for discharge with lower collisionality ν^* and higher adiabaticity α (left column) and discharge with higher collisionality ν^* and lower adiabaticity α (right column).Reprinted from [31].

propagates outward, detaching from the bulk plasma, while the void moves inward, stirring the core plasma.

Figure 9 schematically illustrate the mechanism of the convective motion of coherent structures. Due to curvature and gradient of the main magnetic field, ions and electrons within the coherent structure drift in opposite directions, with velocity

$$\boldsymbol{v_D} = \frac{2T}{qB}\boldsymbol{\kappa} \times \hat{\boldsymbol{z}}. \tag{45}$$

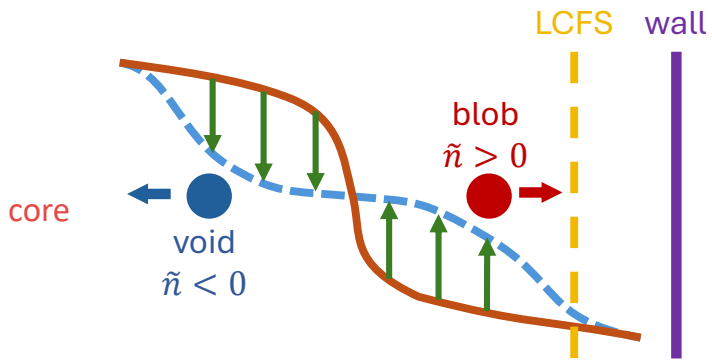

Figure 8. Generation of blob-void pairs from edge gradient relaxation events close to the LCFS.

As a result, the accumulation of positive and negative charges at opposite ends of the structure gives rise to a polarization electric field inside it. This polarization field further drives an $\boldsymbol{E} \times \boldsymbol{B}$ drift velocity that convects the structure radially [33].

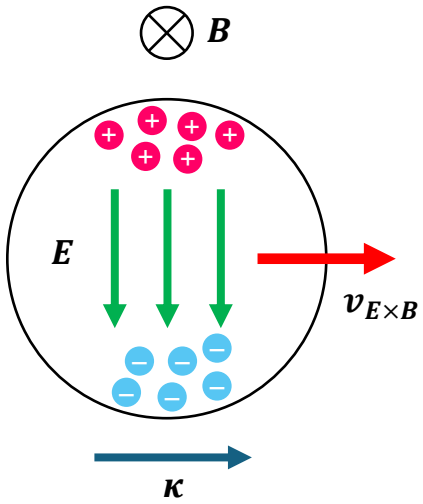

Figure 9. Mechanism of the convection motion of coherent structures. Magnetic drifts induce the polarization of the structure, creating an internal electric field. The resulting $\boldsymbol{E} \times \boldsymbol{B}$ drift then moves blobs outward and void inward.

The convection velocity of coherent structures can be derived heuristically from a two-field model [34]. Since plasma is quasi-neutral, the plasma current density is divergence-free, i.e.

$$\nabla \cdot \boldsymbol{J} = 0. \tag{46}$$

Here $\boldsymbol{J}$ contains the magnetic drift current $\boldsymbol{J}_B$, the polarization current $\boldsymbol{J}_p$, and the parallel current $\boldsymbol{J}_\parallel$. In the strongly collisional regime, $\boldsymbol{J}_\parallel$ is neglected. For isothermal plasmas, the balance of $\boldsymbol{J}_B$ and $\boldsymbol{J}_p$ yields

$$\left(\frac{\partial}{\partial t}+\hat{\boldsymbol{z}}\times\nabla\varphi\cdot\nabla\right)\nabla_\perp^2\varphi+\hat{\boldsymbol{z}}\cdot(\hat{\boldsymbol{\kappa}}\times\nabla\ln n)=0. \tag{47}$$

Equation 47 is in the dimensionless form, where $\hat{\kappa}=\rho_s/R$ is the dimensionless magnetic curvature. To close the model, the evolution of n is given by the continuity equation

$$\left(\frac{\partial}{\partial t}++\hat{\boldsymbol{z}}\times\nabla\varphi\cdot\nabla\right)\ln n=0. \tag{48}$$

This two-field model is identical to the model for the evolution of interchange modes. In the study of blobs and voids, an analytical approach known as the "correspondence principle" is proposed [35]. This principle relates the spatiotemporal scales of coherent structures and interchange modes through the following mapping:

$$\gamma\rightarrow\frac{u_x}{\Delta},\ k_{bot}\rightarrow\frac{1}{\Delta},k_\parallel\rightarrow\frac{1}{L_\parallel}, \tag{49}$$

where γ, $k_\perp$, and $k_\parallel$ are the growth rate, parallel wave vector, and perpendicular wave vector of interchange instabilities, and u_x, Δ, and $L_\parallel$ are the radial convection speed, perpendicular size and parallel extent of coherent structures. Accordingly, the scaling of the convection speed of coherent structure is

$$\frac{u_x}{c_s}\sim\left(\frac{2\Delta}{R}\frac{\delta n}{n_0}\right)^{\frac{1}{2}}, \tag{50}$$

where δn is the density perturbation associated with the coherent structure. It should be noted that scaling in equation 50 is only an upper-bound estimate of the structure convection speed. In reality, coherent structures are subjected to secondary instabilities, such as Kelvin-Helmholtz instability, which can greatly slow down the motion of coherent structures [34].

Voids generated just inside the separatrix and propagating inward can couple the edge

region to the core. Clearly, a nonlocal theory is required to describe this phenomenon.

0.4 Organization of remaining chapters

In this dissertation, we extend the existing framework of plasma turbulence theory by introducing some new elements. We investigate the effects of a background stochastic magnetic field on the dynamics of plasma instability, and take geometric effects into account. We also study the inward turbulence spreading induced by voids in tokamaks, which gives rise to the nonlocal nature of plasma turbulence.

In Chapter 1, an analysis of instability dynamics in a stochastic magnetic field is presented for the tractable case of the resistive interchange. We demonstrate that, due to the size disparity between the test mode and magnetic perturbations, small-scale convective cells are driven to maintain the quasi-neutrality of the plasma at all orders. The turbulent viscosity and diffusivity generated by these cells are calculated by fluctuation-dissipation type analyses. It is also shown that a non-trivial correlation between the ambient magnetic perturbations and these cells develops. This correlation provides a qualitative explanation for why turbulence becomes more ”noisy” when ELMs are suppressed by stochastic magnetic fields in experiments. We calculate the correction of the growth rate of the large-scale interchange mode. It turns out that the mode growth is slowed down by a magnetic braking effect.

In Chapter 2, we present a multi-scale model of quasi-mode evolution in a stochastic magnetic field. As the quasi-mode resembles the ballooning mode, we obtain useful insights into how toroidicity affects the plasma dynamics in a stochastic background. As a result of the broad mode structure of the quasi-mode, the turbulent viscosity and diffusivity produced by the small-scale convective cells are larger than those in our study on resistive interchange modes in Chapter 1. The correlation between the magnetic perturbations and these cells is also modified due to the change in the mode structure. We discover a new mechanism by which stochastic magnetic fields suppress mode growth: the reduction in the effective drive.

In Chapter 3, we develop a model that incorporates density voids generated from edge gradient relaxation events into turbulence dynamics. Through this model, we demonstrate that the previously overlooked process of drift wave emission from inward-moving voids may help resolve a long-standing issue: why the fluctuation level in the edge-core coupling region is higher than predicted. These emitted drift waves, which are regulated ultimately by a self-generated shear flow, drive substantial inward turbulence spreading, leading to the formation of a broad turbulent layer. The width of this turbulent layer is calculated for the first time. The shearing rate of the void-driven zonal flow and the void lifetime are estimated as well.

In Chapter 4, we conclude this dissertation by summarizing the key results presented in the preceding chapters and outlining possible directions for future research.

Chapter 1

Instability and Turbulent Relaxation in a Stochastic Magnetic Field

1.1 Introduction

The dynamics of instability, relaxation, and turbulence are (taken collectively) fundamental to magnetic confinement physics. Here, 'relaxation' includes the evolution of plasma free energy (in the presence of sources and sinks), and the resulting transport [36]. Relaxation determines plasma confinement and possible bifurcations between different states thereof [37]. Recently, a new element has been added to this already challenging problem. Good confinement is no longer deemed sufficient. Rather, good confinement must be achieved along with good power handling and boundary control [38]. Hence, plasma relaxation must be addressed in a base state which is either three dimensional or even stochastic. A specific example of this is the Resonant Magnetic Perturbation, or RMP [24]. The development of RMP was motivated by the desire to mitigate or suppress ELM-driven relaxation by inducing a stochastic layer at the plasma edge. The hope was that mitigation could be achieved without excessive degradation of confinement. One consequence of inducing such extrinsic stochasticity is that turbulence evolution and transport bifurcation now occur in a background with chaotic magnetic fields, and so the theory must address this. In the case of RMP plasmas, models of pedestal transport [39], the L-H transition [40], flow and electric field shear evolution [41], and turbulence dynamics [42] all must be re-formulated to account for the presence of extrinsic stochasticity and its effects.

These problems present many challenges, starting with the need to revisit fundamental instability dynamics in a stochastic background. That problem constitutes the primary motivation for this paper. We note here, in passing, that the case of RMP is not unique. Stellarator confinement [43], magnetic island evolution [44], and the dynamics of disruptions [45] all require us to confront the coexistence and synergy of instability, turbulence and magnetic stochasticity.

As noted above, the very first question we must answer is how ambient magnetic stochasticity impacts instability evolution. This is something of a classic problem in MFE theory, and early interest in it was motivated by the persistence of MHD-like phenomena in high temperature plasmas, where decoupling of field and fluid by resistivity was ineffective. Magnetic braiding by stochastic fields—which was hypothesized to produce electron heat transport [46], or, equivalently, electron viscosity [47]—was a natural alternative candidate. Of this genre of work, the paper of Kaw, et al. [48] is especially well known. This analysis invoked anomalous electron viscosity to trigger tearing mode growth. That calculation followed the idea of 'low-$\boldsymbol{k}$ mode meets high-$\boldsymbol{k}$ ambient background'—i.e., a problem in disparate scale interaction of a low-$\boldsymbol{k}$ coherent fluctuation (single mode) with high-$\boldsymbol{k}$ turbulence. Several other works pursued and developed the electron viscosity/hyper-resistivity idea [49, 50, 51]. All such papers focused on magnetic stochasticity-as-anomalous-dissipation, and did not address relevant issues such as stochasticity effects on mode structure (i.e. the large-scale mode lives in an effective potential which is random), self-consistency effects, and closure of the microscale $\leftrightarrow$ macroscale feedback loop. All treated the effects of stochasticity using a quasilinear-type approach in which quasi-neutrality was not maintained at all orders in the analysis. More generally, these analyses were not systematic.

A clue to the importance of maintaining $\nabla \cdot \boldsymbol{J} = 0$ at all orders of the calculation may be found in the theory of stochastic field induced heat transport proposed by Kadomtsev and Pogutse [52]. There, $\nabla \cdot \boldsymbol{q} = 0$ was maintained throughout the analysis, and forced consideration of static temperature fluctuations on small scales, which were induced by the imposed magnetic perturbations. Temperature fluctuations are generated by the interaction of magnetic perturbations

and the mean temperature profile. The effects of these temperature fluctuations was to cause a dramatic reduction in the effective cross-field heat conductivity, due to a cancellation between leading terms in the heat flux. The message was clear —maintaining $\nabla \cdot \boldsymbol{q} = 0$ revealed the importance of considering accompanying small-scale temperature perturbations induced by $\tilde{\boldsymbol{b}}$, which in turn forced a significant departure from kinematic expectations. In the problem considered here, $\tilde{\boldsymbol{b}}$ induces small-scale *potential* fluctuations, which have important effects.

In this paper, we present the theory of a simple instability in a static, ambient stochastic magnetic field. The instability studied is the electrostatic resistive interchange, and this choice is motivated by the desire for simplicity. The problem is framed as one where we seek to determine the evolution of a particular low-m mode in a fixed, stochastic background. However, maintenance of quasi-neutrality throughout the analysis brings a surprise! We show that the interaction of the imposed magnetic perturbations and the large-scale structure must necessarily drive a spectrum of small-scale convective cells. *Thus, what one thinks of as a problem of a single electrostatic mode in a stochastic background is actually a multi-scale convective cell turbulence problem!* We see that small-scale magnetic stochasticity drives small-scale convective turbulence as a consequence of quasi-neutrality. Enhanced transport—represented by a turbulent viscosity and thermal diffusivity—results. The analysis employs the method of averaging to derive coupled small-scale fluctuations and mean field (i.e., large-scale cell) equations. Thus the analysis has features in common with that for multi-scale problems [16, 53, 54, 55]. An interesting finding of this calculation is that small scales exert a magnetic braking effect on large scales. This effect resembles—but is not identical—to the magnetic braking predicted for tearing modes by Rutherford [56]. The analysis incorporates multi-scale feedback loops, which couple the dynamics of the large-scale envelope and small-scale cells. The structure of the analysis is shown in FIG. 1.1. At large scale, there is a single resistive interchange mode driven by magnetic curvature and mean pressure gradient. When a stochastic magnetic field is imposed, to maintain $\nabla \cdot \boldsymbol{J} = 0$ at all scales, the beat of the large-scale cell and the stochastic magnetic field drives small-scale convective cells, which further generate a turbulent viscosity

and a turbulent diffusivity. The effects of the stochastic magnetic field on the large-scale cell are: 1, stochastic magnetic field itself can effectively enhance the plasma inertia and then oppose the mode growth—i.e., a magnetic braking effect; 2, the resultant turbulent viscosity can slow down the mode growth; 3, small-scale convective cells can modify the large-scale cell via electrostatic scattering. The growth of small-scale convective cells is saturated by the turbulent viscosity, and adiabatically modulated by the beats mentioned above. Thus large scales and small scales interact. We discuss the relation of our results to previous simulations and current experiments.

The remainder of this paper is organized as follows. We first elaborate on the construction of our model in Sec. 1.2. Quantitative results, including the stochasticity induced correction to the growth of the large-scale mode, the scaling of the turbulent viscosity ν, and the correlation $\langle \tilde{b}_r \tilde{v}_r \rangle$, are also given in Sec. 1.2. In Sec. 1.3, we discuss the physical interpretations of the growth rate correction, with an emphasis on the magnetic braking effect. Conclusion and discussion are in Sec. 1.4. Exact solutions of the eigenmode equation Eq.(1.9), and a brief introduction for Kadomtsev and Pogutse's 1979 work are provided in the Appendix.

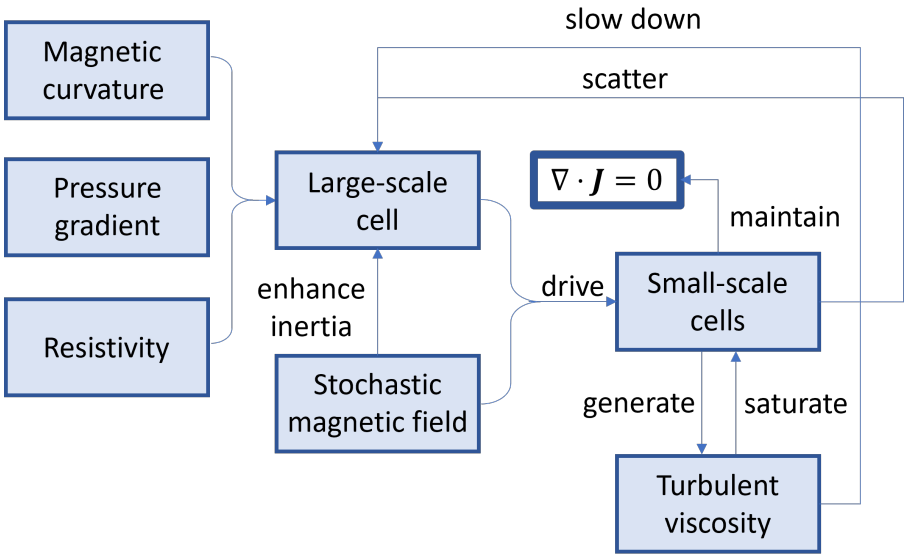

Figure 1.1. Multi-scale feedback loops of small and large scale interaction.

1.2 Model development

Using the quasi-neutrality condition, a model for a large-scale single resistive interchange mode in a stochastic field background is derived and developed in this section. We start with a model of resistive interchange instability driven by magnetic curvature and mean pressure gradient in a smooth magnetic field, and then introduce the stochastic magnetic field by rewriting the parallel gradient operator with the random bending effect included—i.e., $\nabla_{\parallel} \to \nabla_{\parallel}^{(0)} + \tilde{\boldsymbol{b}} \cdot \nabla_{\perp}$. But as will be discussed later, the effects of a stochastic magnetic field are more involved than that. To maintain quasi-neutrality, i.e., $\nabla \cdot \boldsymbol{J} = 0$, small-scale convective cells must be generated. These constitute intrinsically multi-scale microturbulence. The basic equations in our model are vorticity equation, pressure equation, and electrostatic Ohm's law of resistive MHD

$$\left(\frac{\partial}{\partial t} + \tilde{\boldsymbol{v}} \cdot \nabla\right) \nabla_{\perp}^2 (\bar{\varphi} + \tilde{\varphi}) = \frac{\eta S}{\tau_A} \nabla_{\parallel} J_{\parallel} - \frac{\kappa B_0}{\rho_0} \frac{\partial \left(\bar{p}_1 + \tilde{p}_1\right)}{\partial y}, \tag{1.1}$$

$$\left(\frac{\partial}{\partial t} + \tilde{\boldsymbol{v}} \cdot \nabla\right) \left(\bar{p}_1 + \tilde{p}_1\right) - \frac{\nabla(\bar{\varphi} + \tilde{\varphi}) \times \hat{\mathbf{z}}}{B_0} \cdot \nabla p_0 = 0, \tag{1.2}$$

$$\eta J_{\parallel} = -\nabla_{\parallel} \left(\bar{\varphi} + \tilde{\varphi}\right). \tag{1.3}$$

Because the large-scale mode has a much longer time scale than the small-scale convective cells—i.e., there is a time-scale separation. We can use the method of averaging to separate the dynamics of different scales and derive the full set of equations for the model, which is listed as follows:

$$\left(\frac{\partial}{\partial t}+\tilde{\boldsymbol{v}}\cdot\nabla\right)\nabla_{\perp}^{2}\bar{\varphi}= -\frac{S}{\tau_A}\left[\nabla_{\parallel}^{(0)^2}\bar{\varphi}+\underbrace{\left(\nabla_{\perp}\cdot\langle\tilde{\boldsymbol{b}}\tilde{\boldsymbol{b}}\rangle\right)\cdot\nabla_{\perp}\bar{\varphi}}_{(a)}+\underbrace{\left\langle\nabla_{\parallel}^{(0)}\tilde{\boldsymbol{b}}\cdot\nabla_{\perp}\tilde{\varphi}\right\rangle}_{(b)}+\underbrace{\left\langle\left(\tilde{\boldsymbol{b}}\cdot\nabla_{\perp}\right)\nabla_{\parallel}^{(0)}\tilde{\varphi}\right\rangle}_{(c)}\right]-\frac{\kappa B_0}{\rho_0}\frac{\partial\bar{p}_1}{\partial y}, \tag{1.4}$$

$$\left(\frac{\partial}{\partial t}+\tilde{\boldsymbol{v}}\cdot\nabla\right)\bar{p}_1-\frac{\nabla\bar{\varphi}\times\hat{\boldsymbol{z}}}{B_0}\cdot\nabla p_0=0, \tag{1.5}$$

$$\left(\frac{\partial}{\partial t}+\tilde{\boldsymbol{v}}\cdot\nabla\right)\nabla_{\perp}^{2}\tilde{\varphi}=-\frac{S}{\tau_A}\left[\nabla_{\parallel}^{(0)^2}\tilde{\varphi}+\underbrace{\left(\tilde{\boldsymbol{b}}\cdot\nabla_{\perp}\right)\nabla_{\parallel}^{(0)}\bar{\varphi}}_{(\alpha)}+\underbrace{\nabla_{\parallel}^{(0)}\left(\tilde{\boldsymbol{b}}\cdot\nabla_{\perp}\right)\bar{\varphi}}_{(\beta)}\right]-\frac{\kappa B_0}{\rho_0}\frac{\partial\tilde{p}_1}{\partial y}, \tag{1.6}$$

$$\left(\frac{\partial}{\partial t}+\tilde{\boldsymbol{v}}\cdot\nabla\right)\tilde{p}_1-\frac{\nabla\tilde{\varphi}\times\mathbf{z}}{B_0}\cdot\nabla p_0=0. \tag{1.7}$$

In Eq.(1.4), $\bar{\varphi}$ and $\bar{p}$ are the electrostatic potential and pressure of the large-scale mode, $\tilde{\varphi}$ and $\tilde{p}$ are electrostatic potential and pressure fluctuations of the small-scale convective cells, and $\tilde{\boldsymbol{v}}$ is the $\boldsymbol{E}\times\boldsymbol{B}$ velocity fluctuation due to $\tilde{\varphi}$. Since we are studying the dynamics of a single mode, the coupling between large-scale modes is not considered. ρ_0 is the plasma mass density, which is a constant. $\boldsymbol{B}_0=B_0\boldsymbol{b}_0=B_\phi\hat{\boldsymbol{\phi}}+B_\theta(r)\hat{\boldsymbol{\theta}}$ $(B_\phi\gg B_\theta)$ is the mean field, and $\tilde{\boldsymbol{b}}=\tilde{\boldsymbol{B}}_\perp/B_0$ is the direction of perturbed magnetic field. $\boldsymbol{B}_0$ and $\tilde{\boldsymbol{B}}_\perp$ together constitute the magnetic field configuration in this paper. Here we follow a standard low-β, normal aspect ratio ordering [57], in which $\tilde{B}_\perp/B_0\sim\mathscr{O}(\varepsilon)$ but $\tilde{B}_\parallel/B_0\sim\mathscr{O}(\varepsilon^2)$. Thus it is reasonable to neglect stochastic $\tilde{B}_\parallel$ and its related effects, which should surely be revisited when considering stochasticity in a spherical torus [58]. $\boldsymbol{\kappa}=-\kappa\hat{\boldsymbol{r}}$ is the magnetic curvature, which has a dimension of length^{-1}. $p_0(r)$ is the mean pressure profile, which is the only source of the free energy in this model. Two characteristic time scales are adopted: $\tau_A=a(4\pi\rho_0)^{1/2}/B_0$ is the Alfvén time, and $\tau_R=4\pi a^2/\eta$ is the resistive diffusion time (a is the characteristic width of the system, η is the plasma resistivity). The ratio of τ_R to τ_A is denoted by S. Several different gradient operators are used in this model, and their definitions are as follows: $\nabla=\nabla_\parallel^{(0)}\boldsymbol{b}_0+\nabla_\perp$ is the gradient operator,

$\nabla_\perp = \partial_r \hat{\boldsymbol{r}} + (\partial_\theta / r)\hat{\boldsymbol{\theta}}$ is the perpendicular gradient, $\nabla_\parallel^{(0)} = \boldsymbol{b}_0 \cdot \nabla$ is the parallel gradient along the mean field $\boldsymbol{B}_0$, and $\nabla_\parallel = \nabla_\parallel^{(0)} + \tilde{\boldsymbol{b}} \cdot \nabla_\perp$ is the parallel gradient along the total field $\boldsymbol{B}_0 + \tilde{\boldsymbol{B}}_\perp$.

The bracket appearing in Eq.(1.4) is defined as the averaging over toroidal and poloidal directions, i.e.,

$$\langle A \rangle = \left(\frac{1}{2\pi}\right)^2 \iint d\theta d\phi e^{-i(m\theta - n\phi)} A, \tag{1.8}$$

where m and n are the mode numbers of the low m, large-scale mode. After this averaging, only structures whose scales are comparable to that of the large-scale mode can be retained. Thus $\bar{\varphi} = \langle \varphi \rangle = \langle (\bar{\varphi} + \tilde{\varphi}) \rangle$, $\bar{p}_1 = \langle p_1 \rangle = \langle (\bar{p}_1 + \tilde{p}_1) \rangle$.

The geometric configuration of plasma is taken to be a periodic cylinder.

1.2.1 Resistive interchange Mode in a normal magnetic field

In the absence of magnetic perturbation (no $\tilde{\boldsymbol{b}}$, no $\tilde{\varphi}$), Eq.(1.1), Eq.(1.2), and Eq.(1.3) reduce to

$$\underbrace{\frac{\rho_0}{B_0^2}\frac{\partial}{\partial t}\nabla_\perp^2 \varphi}_{-\nabla_\perp \cdot \boldsymbol{J}_{pol}} = \underbrace{\boldsymbol{b}_0 \cdot \nabla J_{\parallel(0)}}_{\nabla_\parallel^{(0)} J_{\parallel(0)}} - \underbrace{\frac{\kappa}{B_0}\frac{\partial p_1}{\partial y}}_{-\nabla_\perp \cdot \boldsymbol{J}_{PS}}, \tag{1.9}$$

$$\frac{\partial p_1}{\partial t} - \frac{\nabla \varphi \times b_0}{B_0} \cdot \nabla p_0 = 0, \tag{1.10}$$

$$\eta J_{\parallel(0)} = -\boldsymbol{b}_0 \cdot \nabla \varphi = -\nabla_\parallel^{(0)} \varphi. \tag{1.11}$$

In Eq.(1.9), $\boldsymbol{J}_{pol}$ denotes the polarization current, and $\boldsymbol{J}_{PS}$ is the Phirsch–Schluter current. Eq.(1.9) is just the expanded form of $\nabla \cdot \boldsymbol{J} = 0$, so quasi-neutrality is naturally maintained at lowest order.

The Fourier series for φ and p_1 are

$$\varphi = \sum_{\boldsymbol{k}} \varphi_{\boldsymbol{k}}(x) e^{\gamma_{\boldsymbol{k}} t + i(m\theta - n\phi)},$$

$$p_1 = \sum_{\boldsymbol{k}} p_{1\boldsymbol{k}}(x)\, e^{\gamma_{\boldsymbol{k}} t + i(m\theta - n\phi)},$$

where $\boldsymbol{k}$ denotes a set of mode number (m,n) and $x = r - r_{mn}$ is a coordinate denoting the distance from the position of the resonant surface r_{mn}. Plugging in these series, Eq.(1.9), Eq.(1.10), and Eq.(1.11) then reduce to the following eigenmode equation ([59, 60, 61])

$$-\gamma_{\boldsymbol{k}} \frac{\partial^2 \varphi_{\boldsymbol{k}}}{\partial x^2} + \frac{S}{\tau_A} \frac{k_\theta^2}{L_S^2} x^2 \varphi_{\boldsymbol{k}} + \left(\gamma_{\boldsymbol{k}} k_\theta^2 - \frac{\kappa p_0 k_\theta^2}{\rho_0 L_p \gamma_{\boldsymbol{k}}} \right) \varphi_{\boldsymbol{k}} = 0, \tag{1.12}$$

where

$$L_p = |(1/p_0)(\mathrm{d}p_0/\mathrm{d}r)|^{-1} \qquad L_s = s/Rq,$$
$$s = |\mathrm{d}\ln(q)/\mathrm{d}\ln(r)| \qquad k_\theta = m/r_{mn},$$

and R is the major radius of the torus.

Eq.(1.12) can be solved exactly, and its eigen solutions are listed in Appendix.(1.A). In this paper, we merely use the growth rate of "ground state" in two limiting cases:

- $k_r \gg k_\theta$ (slow interchange ordering)

$$\gamma_{\boldsymbol{k}} = S^{-\frac{1}{3}} \tau_A^{\frac{1}{3}} \tau_p^{-\frac{2}{3}} \tau_\kappa^{-\frac{2}{3}} \tilde{k}_\theta^{\frac{2}{3}}; \tag{1.13}$$

- $k_r \ll k_\theta$ (fast interchange ordering)

$$\gamma_{\boldsymbol{k}} = \tau_p^{-\frac{1}{2}} \tau_\kappa^{-\frac{1}{2}}, \tag{1.14}$$

where

$$\tau_p = L_p/c_s \quad \tau_\kappa = 1/c_s\kappa \quad \tilde{k}_\theta = k_\theta L_s.$$

Detailed calculations of the above results can also be find in Appendix.(1.A).

1.2.2 Model with a static stochastic magnetic field

In this section, we discuss the effects of the stochastic magnetic field.

With RMP, magnetic field lines become chaotic in the edge layer. So the total magnetic

field consists of a main field and a perturbed field, i.e., $\boldsymbol{b}_{tot} = \boldsymbol{b_0} + \tilde{\boldsymbol{b}}$. More specifically, $\tilde{\boldsymbol{b}}$ is composed of a series of small magnetic perturbations strongly localized at resonant surfaces, as shown in FIG. 1.2. When these $\tilde{b}_{r_{\boldsymbol{k}_1}}$ are sufficiently densely packed so magnetic islands overlap, the field becomes stochastic. Therefore, the way we introduce stochastic magnetic field is by modifying the parallel gradient $\nabla_{\parallel}^{(0)}$ to $\nabla_{\parallel}$, which refers to $\nabla_{\parallel} \to \nabla_{\parallel}^{(0)} + \tilde{\boldsymbol{b}} \cdot \nabla_{\perp}$.

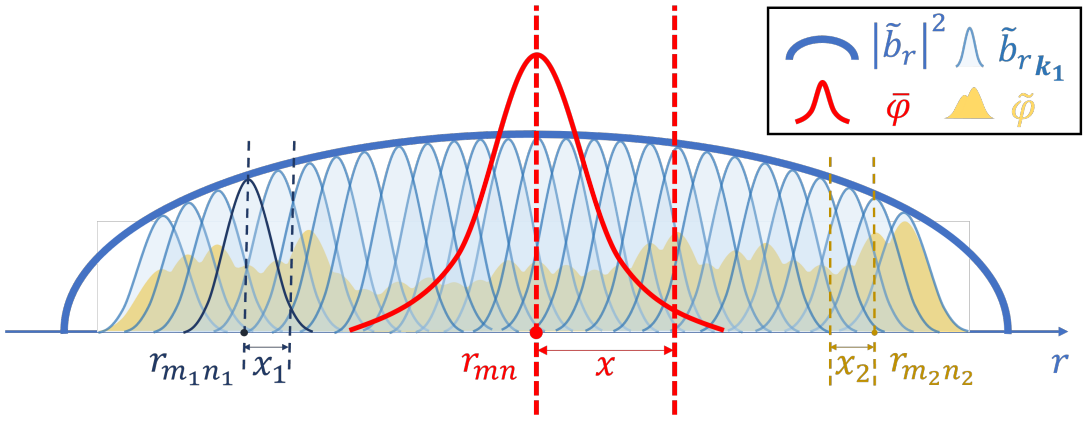

Figure 1.2. Basic configuration of the model: thick blue line represents the profile of stochastic magnetic field and small humps are perturbed magnetic fields at different resonant surfaces; red line represents the large-scale mode; yellow lump is the resultant microturbulence.

With this change, the parallel current density given by Eq.(1.11) is modified to

$$\boldsymbol{J}_{\parallel} = -\frac{1}{\eta}\left[\nabla_{\parallel}^{(0)} + \tilde{\boldsymbol{b}} \cdot \nabla_{\perp}\right] \bar{\varphi}(\boldsymbol{b}_0 + \tilde{\boldsymbol{b}}), \tag{1.15}$$

N.B. here $\boldsymbol{J}_{\parallel}$ refers to current along the wandering field. This will necessarily render $\nabla \cdot \boldsymbol{J} = 0$ a stochastic differential equation. Since the scale of the single mode is much larger than that of the stochastic magnetic field, Eq.(1.15) indicates that the stochastic magnetic field can induce a small-scale current $\tilde{\boldsymbol{J}}_{\parallel}$, and its divergence is

$$\widetilde{\nabla_{\parallel} \boldsymbol{J}_{\parallel}} = -\frac{1}{\eta}\Big[\underbrace{\left(\tilde{\boldsymbol{b}} \cdot \nabla_{\perp}\right) \nabla_{\parallel}^{(0)} \bar{\varphi}}_{(\alpha)} + \underbrace{\nabla_{\parallel}^{(0)} \left(\tilde{\boldsymbol{b}} \cdot \nabla_{\perp}\right) \bar{\varphi}}_{(\beta)}\Big]. \tag{1.16}$$

The quasi-neutrality condition requires $\nabla \cdot \boldsymbol{J} = 0$ at all scales, which means $\tilde{\boldsymbol{J}}_{\parallel}$ should also be

divergence-free. To clarify, we need to use the Fourier series of $\tilde{\boldsymbol{b}}$ and $\bar{\varphi}$:

$$\tilde{\boldsymbol{b}} = \sum_{\boldsymbol{k}_1} \tilde{\boldsymbol{b}}_{\boldsymbol{k}_1}(x_1)\, e^{i(m_1\theta - n_1\phi)},$$
$$\bar{\varphi} = \bar{\varphi}_{\boldsymbol{k}}(x) e^{\gamma_{\boldsymbol{k}} t + i(m\theta - n\phi)},$$

where $x_1 = r - r_{m_1 n_1}$, $x = r - r_{mn}$, as illustrated in FIG. 1.2. Plugging these Fourier series into Eq.(1.16), terms labelled as (α) and (β) are then equal to

$$\begin{aligned}
&\left(\tilde{\boldsymbol{b}}\cdot\nabla_\perp\right)\nabla_\parallel^{(0)}\bar{\varphi} \\
=&\sum_{\boldsymbol{k}_1}\left[\tilde{b}_{r_{\boldsymbol{k}_1}}(x_1)\, e^{i(m_1\theta - n_1\phi)}\partial_x\left(ik_\parallel\bar{\varphi}_{\boldsymbol{k}}(x)e^{i(m\theta-n\phi)}\right)\right] + \\
&\sum_{\boldsymbol{k}_1}\left[+\tilde{b}_{\theta_{\boldsymbol{k}_1}}(x_1)\, e^{i(m_1\theta - n_1\phi)}\partial_y\left(ik_\parallel\bar{\varphi}_{\boldsymbol{k}}(x)e^{i(m\theta-n\phi)}\right)\right] \\
\approx&\sum_{\boldsymbol{k}_1}\tilde{b}_{r_{\boldsymbol{k}_1}}(x_1)\,\partial_x\left(ik_\parallel\bar{\varphi}_{\boldsymbol{k}}(x)\right)e^{i[(m_1+m)\theta-(n_1+n)\phi]},
\end{aligned} \tag{1.17}$$

and

$$\begin{aligned}
&\nabla_\parallel^{(0)}\left(\tilde{\boldsymbol{b}}\cdot\nabla_\perp\right)\bar{\varphi} \\
=&\nabla_\parallel^{(0)}\sum_{\boldsymbol{k}_1}\left[\tilde{b}_{r_{\boldsymbol{k}_1}}(x_1)\, e^{i(m_1\theta - n_1\phi)}\partial_x\left(\bar{\varphi}_{\boldsymbol{k}}(x)e^{i(m\theta-n\phi)}\right)\right] + \\
&\nabla_\parallel^{(0)}\sum_{\boldsymbol{k}_1}\left[\tilde{b}_{\theta_{\boldsymbol{k}_1}}(x_1)\, e^{i(m_1\theta - n_1\phi)}\partial_y\left(\bar{\varphi}_{\boldsymbol{k}}(x)e^{i(m\theta-n\phi)}\right)\right] \\
\approx&\sum_{\boldsymbol{k_1}} i\left(k_{1\parallel}+k_\parallel\right)\tilde{b}_{r_{\boldsymbol{k_1}}}(x_1)\,\partial_x\bar{\varphi}_{\boldsymbol{k}}(x)e^{i[(m_1+m)\theta-(n_1+n)\phi]},
\end{aligned} \tag{1.18}$$

in which the slow interchange ordering approximation has been used. In order for $\widetilde{\nabla_\parallel J_\parallel} = 0$ to be true, the equation

$$\left[k_{1\theta}\left(x + r_{mn} - r_{m_1 n_1}\right)\partial_x\bar{\varphi} + k_\theta\bar{\varphi}\right] = 0 \tag{1.19}$$

must be true for arbitrary $\boldsymbol{k}_1$, which is clearly impossible. It means that the current density fluctuation along perturbed field lines $\tilde{\boldsymbol{J}}_\parallel$ is not itself divergence free. Thus to maintain $\nabla\cdot\boldsymbol{J} = 0$, a small-scale electrostatic potential fluctuation $\tilde{\varphi}$ and a small-scale pressure fluctuation $\tilde{p}_1$ must be

driven, which can make extra contributions to $\tilde{\boldsymbol{J}}_\perp$ so as to keep $\widetilde{\nabla_\parallel J_\parallel} + \widetilde{\nabla_\perp \cdot J_\perp} = 0$, as illustrated in FIG. 1.3.

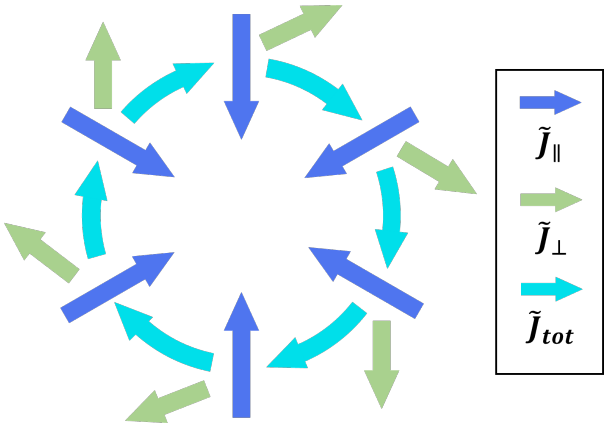

Figure 1.3. The balance between $\tilde{\boldsymbol{J}}_\parallel$ and $\tilde{\boldsymbol{J}}_\perp$. A current density fluctuation $\tilde{\boldsymbol{J}}_\perp$ is driven to balance $\tilde{\boldsymbol{J}}_\parallel$, so that the total current density fluctuation $\tilde{\boldsymbol{J}}_{tot}$ is divergence free.

Physically, the appearance of $\tilde{\varphi}$ signals the presence of small-scale convective cells. Therefore, this system owns a multi-scale nature and actually contains three players: a large-scale single cell (large red ellipse), a prescribed background stochastic magnetic field (small blue arrows), and small-scale convective cells (small orange ellipsis), i.e., the intrinsic multi-scale microturbulence (see FIG. 1.4). These convective cells are driven by the beating of the large-scale mode and the stochastic field. This fact brings us back to Eq.(1.1), Eq.(1.2) and Eq.(1.3), which further yield the full set of model equations Eq.(1.4a)$\sim$ Eq.(1.4d), by using method of averaging. This idea is similar to that of Kadomtsev and Pogutse's study in 1979, in which small-scale temperature fluctuations are generated to maintain $\nabla \cdot \boldsymbol{q} = 0$ ($\boldsymbol{q}$ is electron heat flux) at all scales in a stochastic magnetic field [52]. See Appendix.(1.B) for more details.

For simplicity, the fast interchange ordering approximation is applied to $\tilde{\varphi}$, as it is small scale. Thus the fundamental scale ordering is

$$\underbrace{\frac{1}{k_{1\theta}} \ll w_{\boldsymbol{k}_1}}_{fast} \ll \underbrace{w_{\boldsymbol{k}} \ll \frac{1}{k_\theta}}_{slow}, \tag{1.20}$$

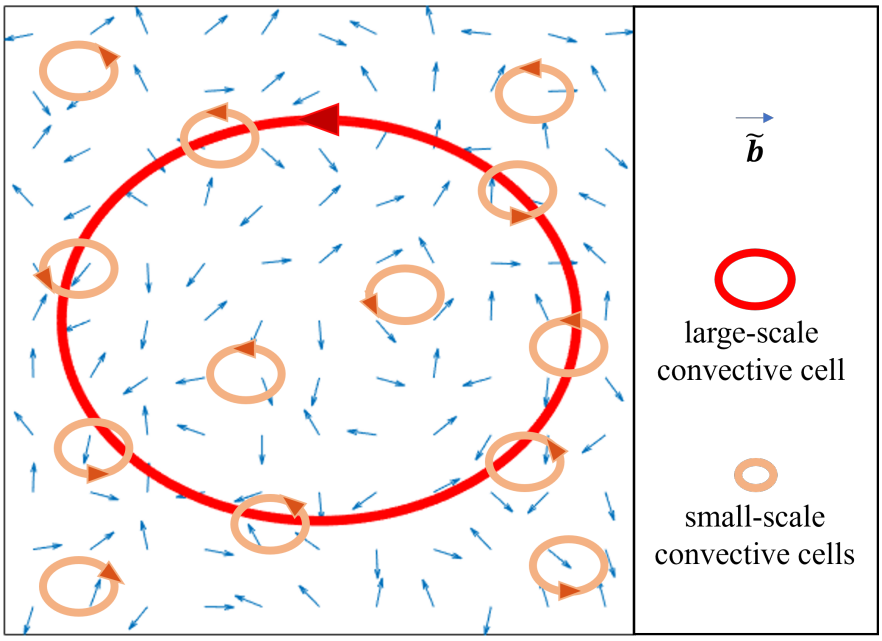

Figure 1.4. Illustration of three main players in this model: large-scale single cell, prescribed background static stochastic magnetic field, and small-scale convective cells.

where $w_{\boldsymbol{k}_1}$ and $w_{\boldsymbol{k}}$ are characteristic radial widths of $\bar{\varphi}_{\boldsymbol{k}}$ and $\tilde{\varphi}_{\boldsymbol{k}_1}$, respectively.

Moreover, this convective cell microturbulence will generate a turbulent viscosity ν and a turbulent diffusivity χ. Due to the separation of temporal scales, and since the large-scale cell is evolving very slowly, the small-scale cells are considered in a stationary state, saturated by ν and χ. In this light, we can approximate the nonlinear operator $\tilde{v}\cdot\nabla$ in Eq.(1.4) by a renormalized diffusion operator $-\nu\nabla_\perp^2$. We further take ν and χ as equal, as their physical mechanisms are both random advection. As will be seen in Sec. 1.2.4, the scaling of ν is calculated through nonlinear closure theory.

Obviously, Eq.(1.4a) and Eq.(1.4c) are coupled to each other, since implies large and small scale dynamics are connected: the beat of $\tilde{\boldsymbol{b}}$ and $\bar{\varphi}$ serves as the drive for $\tilde{\varphi}$, while $\tilde{\varphi}$ modifies the evolution of $\bar{\varphi}$. This relation is illustrated in the feedback loop FIG. 1.1.

1.2.3 Response of $\tilde{\varphi}$ to $\tilde{\boldsymbol{b}}$

To calculate the growth rate of $\bar{\varphi}$, we need to deal with the correlations on the R.H.S. of Eq.(1.4a). This requires us to find the relation between $\tilde{\varphi}$ and $\tilde{\boldsymbol{b}}$, which is implicit in Eq.(1.4c). We can use Eq.(1.4d) to eliminate $\tilde{p}_1$ in Eq.(1.4c). The Fourier series of $\tilde{p}$ and $\tilde{\varphi}$ are

$$\tilde{p} = \sum_{\boldsymbol{k}_2} \tilde{p}_{\boldsymbol{k}_2}(x_2) e^{\gamma_{\boldsymbol{k}} t + i(m_2\theta - n_2\phi)},$$
$$\tilde{\varphi} = \sum_{\boldsymbol{k}_2} \tilde{\varphi}_{\boldsymbol{k}_2}(x_2) e^{\gamma_{\boldsymbol{k}} t + i(m_2\theta - n_2\phi)},$$

where

$$x_2 = r - r_{m_2 n_2}.$$

N.B. the growth rates of $\tilde{p}_{\boldsymbol{k}_2}$ and $\tilde{\varphi}_{\boldsymbol{k}_2}$ are $\gamma_{\boldsymbol{k}}$, instead of $\gamma_{\boldsymbol{k}_2}$. The growth of $\tilde{\varphi}$ and $\tilde{p}$ can be viewed at two different time scales. On a short time scale ($\sim 1/\gamma_{\boldsymbol{k}_2}$), $\tilde{\varphi}$ and $\tilde{p}$ are driven by the magnetic curvature and pressure gradient, and damped by ν and χ. Because of the damping of ν and χ, $\tilde{\varphi}$ and $\tilde{p}$ can relax to a stationary state at this time scale. But on a much longer time scale ($\sim 1/\gamma_{\boldsymbol{k}}$), because large scale and small scales interact, the magnitudes of $\tilde{p}$ and $\tilde{\varphi}$ are adiabatically modulated by the magnitude of $\bar{\varphi}$. Therefore, even though fast interchange approximation is applied to $\tilde{\varphi}$ and $\tilde{p}$, their actual growth rates are the same as those of $\bar{\varphi}$ and $\bar{p}$, due to the turbulent viscous and thermal diffusive stresses induced by ν and χ. Then plugging these series into Eq.(1.4d) and utilizing the approximation $\gamma_{\boldsymbol{k}} \ll \nu k_{2\theta}$, we get

$$\tilde{p}_{1\boldsymbol{k}_2} = -\frac{i p_0}{\chi k_{2\theta} B_0 L_p} \tilde{\varphi}_{\boldsymbol{k}_2}. \tag{1.21}$$

By combining Eq.(1.17), Eq.(1.18), Eq.(1.4c), and Eq.(1.21), we obtain an equation whose L.H.S. is homogeneous in $\tilde{\varphi}$, and whose R.H.S is the $\tilde{\boldsymbol{b}}\bar{\varphi}$ drive:

$$\begin{aligned}&\left[-2\nu k_{2\theta}^2\frac{\partial^2}{\partial x_2^2}+\frac{S}{\tau_A}\frac{k_{2\theta}^2x_2^2}{L_s^2}-\left(\frac{1}{\chi\tau_p\tau_\kappa}-\nu k_{2\theta}^4\right)\right]\tilde{\varphi}_{\boldsymbol{k}_2}(x_2)\\&=i\frac{S}{\tau_A}\left[\left(\partial_x k_\parallel\right)\bar{\varphi}_{\boldsymbol{k}}(x)+\left(k_{2\parallel}+k_\parallel\right)\partial_x\bar{\varphi}_{\boldsymbol{k}}(x)\right]\tilde{b}_{r_{(k_2-k)}},\end{aligned}\tag{1.22}$$

The operator on the L.H.S. of Eq.(1.22) looks like that for a quantum harmonic oscillator. So we define the following quantities:

$$M_{\boldsymbol{k}_2}=\frac{1}{4\nu k_{2\theta}^2},\Omega_{\boldsymbol{k}_2}=\sqrt{\frac{8\nu Sk_{2\theta}^4}{\tau_AL_s^2}},\Lambda_{\boldsymbol{k}_2}=\frac{1}{\chi\tau_p\tau_\kappa}-\nu k_{2\theta}^4.$$

Then the corresponding Green's function for Eq.(1.22) is

$$G\left(x_2,x_2'\right)=\sum_l\frac{\psi_{\boldsymbol{k}_2}^l(x_2)\,\psi_{\boldsymbol{k}_2}^l(x_2')}{\Lambda_{\boldsymbol{k}_2}^l-\Lambda_{\boldsymbol{k}_2}},\tag{1.23}$$

where

$$\begin{aligned}\psi_{k_2}^l(x_2)&=\frac{w_{k_2}^{1/2}}{\pi^{1/4}}\frac{1}{\sqrt{2^ll!}}H_l(w_{k_2}x_2)\,e^{-\frac{\left(w_{k_2}x_2\right)^2}{2}},\\w_{k_2}&=\left(\frac{S}{2\tau_A\nu L_s^2}\right)^{1/4},\quad\Lambda_{k_2}^l=\sqrt{\frac{8\nu Sk_{2\theta}^4}{\tau_AL_s^2}}\left(l+\frac{1}{2}\right).\end{aligned}$$

By making use of this Green's function, the solution to Eq.(1.22) is

$$\tilde{\varphi}_{\boldsymbol{k}_2}=-i\frac{S}{\tau_A}\int\left[\partial_{x'}\left(Gk_{2\parallel}\tilde{b}_{r_{(\boldsymbol{k}_2-\boldsymbol{k})}}\right)+k_\parallel\partial_{x'}\left(G\tilde{b}_{r_{(\boldsymbol{k}_2-\boldsymbol{k})}}\right)\right]\bar{\varphi}_{\boldsymbol{k}}dx_2'\tag{1.24}$$

As $\bar{\varphi}_{\boldsymbol{k}}$ varies much more slowly than $\tilde{b}_{r_{(\boldsymbol{k}_2-\boldsymbol{k})}}$ (see Fig.1), it is reasonable to move $\bar{\varphi}_{\boldsymbol{k}}$ out of the integral in Eq.(1.24), and approximate it by its value at $x=0$. Then the first term of the integrand vanishes, because it is a total derivative. Using integration by parts, the response of $\tilde{\varphi}_{\boldsymbol{k}_2}$ to $\tilde{b}_{r_{(\boldsymbol{k}_2-\boldsymbol{k})}}$

is then approximately

$$\tilde{\varphi}_{\boldsymbol{k}_2} \approx -i\frac{k_\theta}{L_s}\frac{S}{\tau_A}\sum_l \frac{\psi^l_{\boldsymbol{k}_2}(x_2)}{\Lambda^l_{\boldsymbol{k}_2}-\Lambda_{\boldsymbol{k}_2}}\bar{\varphi}_{\boldsymbol{k}}(0)\int \psi^l_{\boldsymbol{k}_2}\tilde{b}_{r_{(\boldsymbol{k}_2-\boldsymbol{k})}}dx_2'. \tag{1.25}$$

1.2.4 Corrected growth rate and scaling of turbulent Viscosity

Utilizing the result of Eq.(1.25), we can simplify the correlations which appear in Eq.(1.4a), and calculate the correction to the single mode's growth rate. As will be seen, the turbulent viscosity ν still appears in the expression for the growth rate as an unknown quantity. It can be calculated by using closure theory.

Correlation (a), (b), and (c)

The three correlations we need to calculate are

$$\begin{aligned}(a) &= \left(\nabla_\perp \cdot \langle\tilde{\boldsymbol{b}}\tilde{\boldsymbol{b}}\rangle\right)\cdot\nabla_\perp\bar{\varphi},\\ (b) &= \left\langle \nabla^{(0)}_\parallel \tilde{\boldsymbol{b}}\cdot\nabla_\perp\tilde{\varphi}\right\rangle,\\ (c) &= \left\langle \left(\tilde{\boldsymbol{b}}\cdot\nabla_\perp\right)\nabla^{(0)}_\parallel\tilde{\varphi}\right\rangle.\end{aligned} \tag{1.26}$$

Consistent with the slow interchange ordering at large scale, $\tilde{b}_\theta\partial_y\bar{\varphi} \ll \tilde{b}_r\partial_r\bar{\varphi}$, and $\tilde{\boldsymbol{b}}\cdot\nabla_\perp\bar{\varphi} \approx b_r\partial_r\bar{\varphi}$. Therefore, correlation (a) can be rewritten as

$$(a) = (ik_\theta)\left|\tilde{b}_\theta\tilde{b}_r\right|\partial_x\bar{\varphi} + \partial_x\left(\left|\tilde{b}_r^2\right|\partial_x\bar{\varphi}\right) \approx \left|\tilde{b}_r^2\right|\partial_x^2\bar{\varphi}, \tag{1.27}$$

as $1/k_\theta$ is largest scale of the ordering in Eq.(1.20), and $\left|\tilde{b}_r^2\right|$ varies more slowly than $\bar{\varphi}$ does.

For correlation (b),

$$(b) = \sum_{\boldsymbol{k}_2} ik_\parallel (ik_\theta)\tilde{b}_{\theta_{\boldsymbol{k}-\boldsymbol{k}_2}}\tilde{\varphi}_{k_2} + \sum_{k_2} ik_\parallel\partial_x\left[\tilde{b}_{r_{\boldsymbol{k}-\boldsymbol{k}_2}}\tilde{\varphi}_{\boldsymbol{k}_2}\right] \approx \sum_{\boldsymbol{k}_2} ik_\parallel\partial_x\left[\tilde{b}_{r_{\boldsymbol{k}-\boldsymbol{k}_2}}(x_1)\,\tilde{\varphi}_{\boldsymbol{k}_2}(x_2)\right], \tag{1.28}$$

Similarly, for correlation (c),

$$(c) = \sum_{\boldsymbol{k}_2} \partial_x \left[ik_{2\|} \tilde{b}_{r_{\boldsymbol{k}-\boldsymbol{k}_2}} \tilde{\varphi}_{\boldsymbol{k}_2} \right] + \sum_{\boldsymbol{k}_2} (ik_\theta)\, ik_{2\|} \tilde{b}_{\theta_{\boldsymbol{k}_1}} \tilde{\varphi}_{\boldsymbol{k}_2} \approx \sum_{\boldsymbol{k}_2} \partial_x \left[ik_{2\|} \tilde{b}_{r_{\boldsymbol{k}-\boldsymbol{k}_2}} \tilde{\varphi}_{\boldsymbol{k}_2} \right]. \tag{1.29}$$

By using the dense packing approximation (see FIG. 1.2), the summation over $\boldsymbol{k_2}$ can be replaced by an integral. More specifically,

$$\sum_{\boldsymbol{k}_2(m_2,n_2)} = \iint dm_2 dn_2 = \frac{R}{L_s} \int dk_{2\theta}\, |k_{2\theta}| \int r dx. \tag{1.30}$$

Because Eq.(1.29) is a total derivative, it vanishes after writing the sum as an integral. Therefore, the correlations (a), (b), and (c) are:

$$(a) \approx \left| \tilde{b}_r^2 \right| \partial_x^2 \bar{\varphi}, \quad (b) \approx -\frac{S}{\tau_A} \frac{Rk_\theta^2}{L_s^3} \bar{\varphi}_{\boldsymbol{k}}(0)\, (x + r_{mn}) \times I, \quad (c) \approx 0 \tag{1.31}$$

where

$$I = \int dk_{2\theta} \frac{|k_{2\theta}|}{\Lambda^0_{k_2} - \Lambda_{k_2}} \left[\int dx_2' b_{r_{k-k_2}} \psi^0_{k_2} \right]^2.$$

Here, only the first term of the Green's function in Eq.(1.23) is kept, since the magnitude of $\psi^l_{\boldsymbol{k}_2}$ decreases exponentially with l. If the spatial shape of each $\tilde{b}_{r_{\boldsymbol{k}_2}}(x_2)$ is approximately Gaussian, then I can be simplified to an integral over $k_{2\theta}$ which is

$$\int dk_{2\theta}\, |k_{2\theta}| \frac{\pi^{\frac{1}{2}} c^2 Z^2 (k_\theta - k_{2\theta})\, w_{\boldsymbol{k}_2}}{\Lambda^0_{\boldsymbol{k}_2} - \Lambda_{\boldsymbol{k}_2}} \left(\frac{1}{o^2_{\boldsymbol{k}_2}} + \frac{w^2_{\boldsymbol{k}_2}}{2} \right)^{-1},$$

where c, $Z(k_{2\theta})$ and $o_{\boldsymbol{k}_2}$ are a normalization factor, spectrum and the characteristic width of $\tilde{b}_{r_{\boldsymbol{k}_2}}$ respectively. Because the width of $\tilde{b}_{\boldsymbol{k}_2}$ is much smaller than the width of $\tilde{\varphi}_{\boldsymbol{k}_2}$, i.e., $o_{\boldsymbol{k}_2} \ll 1/w_{\boldsymbol{k}_2}$, we can approximate I as

$$\int dk_{2\theta}\, |k_{2\theta}| \frac{\pi^{\frac{1}{2}} c^2 Z^2 (k_\theta - k_{2\theta})\, w_{\boldsymbol{k}_2} o^2_{\boldsymbol{k}_2}}{\Lambda^0_{\boldsymbol{k}_2} - \Lambda_{\boldsymbol{k}_2}}.$$

Since we have obtained the linear response of $\tilde{\varphi}_{\boldsymbol{k}_2}$ to $\tilde{b}_{r_{(\boldsymbol{k}-\boldsymbol{k}_2)}}$ in Sec. 1.2.3, the correlation of $\tilde{b}_r$ and $\tilde{v}_r$ then is

$$\left\langle \tilde{b}_r \tilde{v}_r \right\rangle = \pi^{\frac{1}{2}} \frac{\tilde{k}_\theta R r_{mn}}{L_s^3 B_0} \frac{S}{\tau_A} \bar{\varphi}_{\boldsymbol{k}}(0) \int dk_{2\theta} \left| k_{2\theta} \right| k_{2\theta} \frac{c^2 Z^2 \left(k_\theta - k_{2\theta} \right) w_{\boldsymbol{k}_2} o_{\boldsymbol{k}_2}^2}{\Lambda_{\boldsymbol{k}_2}^0 - \Lambda_{\boldsymbol{k}_2}}. \tag{1.32}$$

Eq.(1.32) indicates that $\langle \tilde{b}_r \tilde{v}_r \rangle$ is non-trivial in this model. $\langle \tilde{b}_r \tilde{v}_r \rangle \neq 0$ *means the electrostatic turbulence phase locks to the ambient magnetic perturbations.* This is a direct result of Eq.(1.22), because $\tilde{b}_{r_{(\boldsymbol{k}-\boldsymbol{k}_2)}}$ is the drive of $\tilde{\varphi}_{\boldsymbol{k}_2}$. Thus, the statistics of $\tilde{b}_r$ and $\tilde{v}_r$ are not independent.

Corrected growth rate of $\bar{\varphi}$

Substituting Eq.(1.31) into Eq.(1.4a), and taking the Fourier transform of Eq.(1.4a) and Eq.(1.4b), we get

$$\begin{aligned}
&- \frac{S}{\tau_A} \frac{k_\theta^2}{L_s^2} \frac{d^2}{dk_x^2} \hat{\tilde{\varphi}}_{\boldsymbol{k}} \left(k_x \right) + \gamma_{\boldsymbol{k}} k_x^2 \hat{\tilde{\varphi}}_{\boldsymbol{k}} \left(k_x \right) - \frac{\kappa p_0}{L_p \rho_0} \frac{k_\theta^2}{\gamma_{\boldsymbol{k}}} \hat{\tilde{\varphi}}_{\boldsymbol{k}} \left(k_x \right) \\
= &- \nu k_x^4 \hat{\tilde{\varphi}}_{\boldsymbol{k}} \left(k_x \right) - \frac{S}{\tau_A} \left| \tilde{b}_r \right|^2 k_x^2 \hat{\tilde{\varphi}}_{\boldsymbol{k}} \left(k_x \right) - \frac{\kappa p_0 \chi k_\theta^2}{\rho_0 L_p \gamma_{\boldsymbol{k}}^2} k_x^2 \hat{\tilde{\varphi}}_{\boldsymbol{k}} \left(k_x \right) \\
&- \left(\frac{S}{\tau_A} \right)^2 \frac{R k_\theta^2}{L_s^3} \bar{\varphi}_{\boldsymbol{k}}(0) i \sqrt{2\pi} \delta^{(1)} \left(k_x \right) I \\
&- \left(\frac{S}{\tau_A} \right)^2 \frac{R k_\theta^2}{L_s^3} \bar{\varphi}_{\boldsymbol{k}}(0) r_{mn} \sqrt{2\pi} \delta \left(k_x \right) I.
\end{aligned} \tag{1.33}$$

Since the stochastic magnetic field background is weak and the resultant turbulent viscosity ν is also small, we can treat the R.H.S. of Eq.(1.33) as a small perturbation. So Eq.(1.33) can be written as

$$\hat{H}_0 \hat{\tilde{\varphi}}_{\boldsymbol{k}}(k_x) = \hat{H}_1 \hat{\tilde{\varphi}}_{\boldsymbol{k}}(k_x), \tag{1.34}$$

where

$$\hat{H}_0 = -\frac{S}{\tau_A}\frac{k_\theta^2}{L_s^2}\frac{d^2}{dk_x^2} + \gamma_k k_x^2 - \frac{\kappa p_0}{L_p \rho_0}\frac{k_\theta^2}{\gamma_k},$$

$$\begin{aligned}\hat{H}_1 = &-\nu k_x^4 - \frac{S}{\tau_A}\left|\tilde{b}_r\right|^2 k_x^2 - \frac{\kappa p_0 \chi k_\theta^2}{\rho_0 L_p \gamma_k^2} k_x^2 \\ &- \left(\frac{S}{\tau_A}\right)^2 \frac{R k_\theta^2}{L_s^3} i\sqrt{2\pi}\delta^{(1)}(k_x) I \int dx' \delta(x') \mathscr{F}^{-1} \\ &- \left(\frac{S}{\tau_A}\right)^2 \frac{R k_\theta^2}{L_s^3} r_{mn}\sqrt{2\pi}\delta(k_x) I \int dx' \delta(x') \mathscr{F}^{-1}.\end{aligned}$$

We can then attain the corrected growth rate $\gamma_{\boldsymbol{k}}$ by doing perturbation theory. As equation $\hat{H}_0 \hat{\bar{\varphi}}_{\boldsymbol{k}}^{(0)}(k_x) = 0$ is just the Fourier transform of Eq.(1.12), the zeroth-order growth rate is just the growth rate given by Eq.(1.13). Thus the eigenmode solution of the ground state is

$$\hat{\bar{\varphi}}_{\boldsymbol{k}}^{(0)}(k_x) = \bar{\varphi}_{\boldsymbol{k}}^{(0)}(x=0) w_{\boldsymbol{k}} e^{-\frac{w_{\boldsymbol{k}}^2 k_x^2}{2}}, \tag{1.35}$$

where $w_{\boldsymbol{k}} = \left(\frac{\tau_A \gamma_k^{(0)} L_S^2}{S k_\theta^2}\right)^{\frac{1}{4}}$.

By using perturbation theory, the first-order growth rate correction $\gamma_{\boldsymbol{k}}^{(1)}$ is given by the following equation:

$$\gamma_{\boldsymbol{k}}^{(1)} = \frac{\int_{-\infty}^{\infty} \hat{\bar{\varphi}}_{\boldsymbol{k}}^{(0)}(k_x) \hat{H}_1 \hat{\bar{\varphi}}_{\boldsymbol{k}}^{(0)}(k_x) dk_x}{\int_{-\infty}^{\infty} \hat{\bar{\varphi}}_{\boldsymbol{k}}^{(0)}(k_x) \left[\partial_{\gamma_k^{(0)}} \hat{H}_0\right] \hat{\bar{\varphi}}_{\boldsymbol{k}}^{(0)}(k_x) dk_x}. \tag{1.36}$$

Plugging the expressions for $\hat{\bar{\varphi}}_{\boldsymbol{k}}^{(0)}$, $\hat{H}_0$ and $\hat{H}_1$ into Eq.(1.36), the first-order correction to the growth rate of the ground state is

$$\gamma_{\boldsymbol{k}}^{(1)} = -\frac{5}{6}\hat{\nu}\left(\frac{\tau_p \tau_\kappa}{\tau_A^2}\right)^{\frac{1}{3}} S^{\frac{2}{3}} \tilde{k}_\theta^{\frac{2}{3}} - \frac{1}{3}\frac{S}{\tau_A}|\tilde{b}_r|^2 - \frac{2\sqrt{2}}{3}\frac{\hat{I} S^{\frac{4}{3}} \tilde{k}_\theta^{\frac{4}{3}}}{\left(\tau_p \tau_\kappa \tau_A^4\right)^{\frac{1}{3}}}, \tag{1.37}$$

where

$$\hat{\nu} = \nu / L_s^2 \quad \hat{I} = I R r_{mn} / L_s^3.$$

Evidently, the first two terms of the expression for $\gamma_{\boldsymbol{k}}^{(1)}$ are negative definite, while the sign of

the third depends on the sign of I. To determine whether I is positive or negative, the turbulent viscosity ν should be calculated.

Scaling of turbulent viscosity ν

Because ν originates from the $\boldsymbol{E}\times\boldsymbol{B}$ velocity fluctuation $\tilde{\boldsymbol{v}}$, it can be calculated through a simple nonlinear closure theory [62, 63, 64]:

$$\nu = \sum_{\boldsymbol{k}_2} \left|\tilde{v}_{\boldsymbol{k}_2}\right|^2 \tau_{\boldsymbol{k}_2}, \tag{1.38}$$

where $\tau_{\boldsymbol{k}_2}$ is the correlation time. A reasonable estimate of $\tau_{\boldsymbol{k}_2}$ is the reciprocal of the fast interchange growth rate $1/\gamma^{(0)}_{\boldsymbol{k}_2}$. As $\left|\tilde{v}_{\boldsymbol{k}_2}\right| = k_{2\theta}\left|\tilde{\varphi}_{k_2}\right|/B_0$, substituting Eq.(1.25) into Eq.(1.38), we get

$$\nu = \frac{Rr_{mn}}{\pi^{-\frac{1}{2}}L_s^5}\left(\frac{S}{\tau_A}\right)^2 \frac{\tilde{k}_\theta^2\bar{\varphi}^2_{\boldsymbol{k}}(0)}{B_0^2}\int dk_{2\theta}\frac{\left|k_{2\theta}\right|^3 c^2Z^2 w_{\boldsymbol{k}_2}o^2_{\boldsymbol{k}_2}}{\left(\Lambda^0_{\boldsymbol{k}_2}-\Lambda_{\boldsymbol{k}_2}\right)^2\gamma^{(0)}_{\boldsymbol{k}_2}}, \tag{1.39}$$

where both $\Lambda^0_{\boldsymbol{k}_2}$ and $\Lambda_{\boldsymbol{k}_2}$ are functions of ν. So, to extract the scaling of ν, we need a different approach.

Recall in Eq.(1.22) and Eq.(1.23), $\left(\Lambda^0_{\boldsymbol{k}_2}-\Lambda_{\boldsymbol{k}_2}\right)^2$ is equal to

$$\left(\Lambda^0_{\boldsymbol{k}_2}-\Lambda_{\boldsymbol{k}_2}\right)^2 = \Bigg[\underbrace{\sqrt{\frac{2\nu S k^4_{2\theta}}{\tau_A L_s^2}}}_{\Lambda^0_{\boldsymbol{k}_2}} - \underbrace{\left(\frac{\kappa p_0}{\chi\rho_0 L_p}-\nu k^4_{2\theta}\right)}_{\Lambda_{\boldsymbol{k}_2}}\Bigg]^2. \tag{1.40}$$

Because of the fast interchange approximation, $\Lambda^0_{\boldsymbol{k}_2} = 2\nu k^2_{2\theta}/w^2_{\boldsymbol{k}_2} \ll \nu k^4_{2\theta}$. In addition, in the weak-mean-pressure-gradient limit, i.e., $\tau_p \gg 1/\tau_\kappa\nu^2k^4_{2\theta}$, $\nu k^4_{2\theta}$ becomes the dominant term in the bracket of Eq.(1.40). The scaling of ν then is

$$\nu = \left[\pi^{\frac{1}{2}}\frac{Rr_{mn}}{B_0^2}\frac{\tilde{k}^2_\theta}{L_s^5}\left(\frac{S}{\tau_A}\right)^2\bar{\varphi}^2_{\boldsymbol{k}}(0)\int dk_{2\theta}\frac{c^2Z^2w_{\boldsymbol{k}_2}o^2_{\boldsymbol{k}_2}}{\left|k_{2\theta}\right|^5\gamma^{(0)}_{\boldsymbol{k}_2}}\right]^{\frac{1}{3}}. \tag{1.41}$$

This limit can be justified by the following argument.

If we retain the growth rate of $\tilde{\varphi}_{\boldsymbol{k}_2}$ and utilize the fast interchange approximation, Eq.(1.22) is modified to

$$\frac{\partial \tilde{\varphi}}{\partial t} + \lambda \tilde{\varphi} = \hat{D}\left[\tilde{b}_r \bar{\varphi}\right], \tag{1.42}$$

where $\lambda = \nu k_{2\theta}^2 - \left(1/\tau_p \tau_\kappa\right)^{1/2}$, and $\hat{D}\left[\tilde{b}_r \bar{\varphi}\right]$ denotes the drive by $\tilde{b}_r \bar{\varphi}$ beats. The point here is that $\tilde{\varphi}$ is subject to two drives: a linear drive by curvature and pressure gradient, which corresponds to the second term in λ, and a drive by the noise—i.e., $\hat{D}\left[\tilde{b}_r \bar{\varphi}\right]$. As indicated by Eq.(1.38), ν will increase with $|\tilde{\varphi}|$, so $\tilde{\varphi}$ can not grow indefinitely, and there is a point at which ν becomes large enough that both drives saturate. In other words, *the growth of $\tilde{\varphi}$ is over-saturated*. Over-saturation requires $\lambda > 0$—i.e., $\nu k_{2\theta}^2 > \left(1/\tau_p \tau_\kappa\right)^{1/2}$, which is consistent with the limit we used for Eq.(1.41). This is similar to the case of Ref. [53]. Then Eq.(1.42) immediately looks like a generalization of the Langevin equation [65], which further implies a fluctuation-dissipation balance [66]. Here we can see the dual identities of $\tilde{\boldsymbol{b}}$: on the one hand, it serves as part of the noise to excite small-scale cells; on the other hand, the turbulent viscosity ν resulting from it damps small-scale cells. Therefore, as mentioned in Sec. 1.2.3, $\tilde{\varphi}$ and $\tilde{p}$ can reach equilibrium and be adiabatically modulated by the beat of $\tilde{\boldsymbol{b}}\tilde{\varphi}$.

In addition, in this limit $\tau_p \gg 1/\tau_\kappa \nu^2 k_{2\theta}^4$, the integral I is positive, which means the first-order correction to the growth rate given by Eq.(1.37) is negative definite. *So we can conclude the net effect of a stochastic magnetic field on the large-scale mode is to reduce its growth, in proportion to the magnitude of stochastic magnetic field intensity.*

1.3 Analysis: effects of stochastic magnetic field

In the calculation of perturbed growth rate, we defined two operators $\hat{H}_0$ and $\hat{H}_1$, so as to divide the terms in Eq.(1.33) into two groups. All the terms involving the stochastic magnetic field are put in $\hat{H}_1$, so that $\hat{H}_0 \bar{\varphi}_{\boldsymbol{k}}(k_x) = 0$ is just the Fourier transform of Eq.(1.12). Therefore, H_0 gives the zeroth-order growth rate of $\bar{\varphi}_{\boldsymbol{k}}$, which is consistent with the classical linear theory of

the resistive interchange mode. Since the stochastic magnetic field is weak, $\hat{H}_1$ is regarded as a perturbation. To analyze the effects of stochastic magnetic field clearly, we can number the different terms of the expression for $\hat{H}_1$ as

$$\hat{H}_1 = -\underbrace{\nu k_x^4}_{①} - \underbrace{\frac{S}{\tau_A}\left|\tilde{b}_r\right|^2 k_x^2}_{②} - \underbrace{\frac{\kappa p_0 \chi k_\theta^2}{\rho_0 L_p \gamma_k^2} k_x^2}_{③} - \underbrace{\left(\frac{S}{\tau_A}\right)^2 \frac{R k_\theta^2}{L_s^3}\sqrt{2\pi}\left[\delta^{(0)} r_{mn} + i\delta^{(1)}\right] I \int dk_x' \delta^{(0)} \mathscr{F}^{-1}}_{④}. \tag{1.43}$$

Among these four terms, the physics of term ②, which comes from the correlation (a) in Eq.(1.4a), is clearest. Term ② shares the same form with the second term of the expression for $\hat{H}_0$, i.e., they are both quadratic functions of k_x. If we neglect the other perturbations, Eq.(1.33) is rewritten as

$$-\frac{S}{\tau_A}\frac{k_\theta^2}{L_s^2}\frac{d^2}{dk_x^2}\bar{\varphi}_{\boldsymbol{k}} + \left[\gamma_{\boldsymbol{k}} + \frac{S}{\tau_A}\left|\tilde{b}_r\right|^2\right] k_x^2 \bar{\varphi}_{\boldsymbol{k}} - \frac{\kappa p_0}{L_p \rho_0}\frac{k_\theta^2}{\gamma_{\boldsymbol{k}}}\bar{\varphi}_{\boldsymbol{k}} = 0. \tag{1.44}$$

When the magnitude of the stochastic magnetic field is large, the corrected growth rate of the ground state is

$$\gamma_{\boldsymbol{k}} = \frac{\tilde{k}_\theta}{S\left|\tilde{b}_r\right|}\frac{\tau_A}{\tau_p \tau_\kappa}. \tag{1.45}$$

In Eq.(1.45), $\gamma_{\boldsymbol{k}} \propto \left|\tilde{b}_r\right|^{-1}$, so the larger the magnitude of the stochastic magnetic field, the smaller the growth rate of the large-scale mode.

If there is no stochastic field, the growth of $\bar{\varphi}_{\boldsymbol{k}}$ is driven against inertia by torque produced by pressure gradient. Now, the stochastic magnetic field effectively adds to the inertia of plasma and thus stabilizes the growth of mode. This effect is magnetic vorticity damping. By re-expressing

$$\frac{S}{\tau_A}\left|\tilde{b}_{r_{\boldsymbol{k}_2}}\right|^2 = \frac{v_A^2}{\eta}\frac{k_{2\theta}^2}{L_s^2} o_{\boldsymbol{k}_2}^4, \tag{1.46}$$

we can balance it with the linear bending term and obtain

$$\begin{aligned} \frac{v_A^2}{\eta}\frac{k_{2\theta}^2}{L_s^2}\frac{o_{\boldsymbol{k}_2}^4}{(\Delta x)^2}\bar{\varphi}_{\boldsymbol{k}_2} &\sim \frac{v_A^2}{\eta}\frac{k_\theta^2}{L_s^2}(\Delta x)^2\bar{\varphi}_{\boldsymbol{k}_2} \\ o_{\boldsymbol{k}_2} &\sim \left[\frac{k_\theta^2}{k_{2\theta}^2}(\Delta x)^4\right]^{\frac{1}{4}}. \end{aligned} \tag{1.47}$$

Eq.(1.47) offers us a criterion when magnetic vorticity damping becomes a significant effect, and reduces the growth of the mode. This result is a reminiscent of Rutherford's 1973 work on the tearing mode [56]. In that paper, the perturbed magnetic field growing with growth rate γ can induce a perturbed current, which further produces a torque that can drive the tearing mode against plasma inertia. But as the perturbed field grows, the nonlinear force will gradually dominate and produce a torque opposing the growth of the mode. By balancing the torque produced by linear and nonlinear forces, Rutherford noted the system enters the nonlinear regime when the widths of the magnetic islands become comparable to the width of the tearing layer, i.e., when $o_{\boldsymbol{k}_2} \sim \Delta x$. In our model, this corresponds to the condition when Eq.(1.47) holds. The stochastic magnetic field resembles the nonlinear force in Rutherford's model. The difference between Rutherford's model and ours is also significant: the extra factor $(k_\theta^2/k_{2\theta}^2)$ in Eq.(1.47) reflects the multi-scale nature of this problem.

Term ① and term ③ are both related to turbulent viscosity ν (or turbulent diffusivity χ, which is equal to ν in this model). As discussed in Sec. 1.2.2 and Sec. 1.2.4, those small-scale convective cells produce a turbulent viscosity ν. So it is not a surprise to find that the mode is stabilized by this turbulent viscosity (the first term on the R.H.S of Eq.(1.37) is negative).

The physics of term ④ is more complex. It originates from the correlation (b) in Eq.(10a)(BTW, correlation (c) vanishes since it is a total derivative). We can rewrite correlation (b) as

$$\left\langle \nabla_\parallel^{(0)}\tilde{\boldsymbol{b}}\cdot\nabla_\perp\tilde{\varphi}\right\rangle \sim \left\langle \nabla_\parallel^{(0)}\tilde{b}_r\tilde{E}_r\right\rangle \sim \nabla_\parallel^0\left\langle \tilde{J}_{\parallel 0}\right\rangle^{(3)}. \tag{1.48}$$

From Eq.(1.48) we can see, the potential fluctuation produces a fluctuating radial electric field,

which further generates a current parallel to $\boldsymbol{B}_0$. In the final result, the correction to the growth rate from term ④ is the last term in Eq.(1.37), whose sign depends on the sign of I. Since we have taken the limit $L_p \gg c_s/\tau_\kappa \nu^2 k_{2\theta}^4$, I is positive, which means term ④ can also reduce the growth of the mode. This is due to the fact that large-scale mode is electrostatically scattered by small-scale convective cells.

In summary, the interaction between the large-scale mode and small-scale convective cells forms a feedback loop. As illustrated in the FIG. 1.1, the stochastic magnetic field and the large-scale cell together can drive small-scale cells while small-scale cells react on the large-scale cell through two different approaches: electrostatic scattering and turbulent viscosity.

1.4 Conclusion and discussion

In this paper, we presented an in-depth analysis of the theory of instability and turbulent relaxation in a stochastic magnetic field. For tractability, we focus on a comparatively simple, yet relevant and representative, system—namely that of the electrostatic resistive interchange. Here, the static magnetic fluctuations which underpin the stochasticity render parallel gradients $\nabla_\parallel \to \nabla_\parallel^{(0)} + \tilde{\boldsymbol{b}} \cdot \nabla_\perp$, and so modify the basic structure of the eigenmode equation by converting it to a stochastic differential equation. This is, in turn, solved by the method of averaging, which exploits the scale separation between the low-$\boldsymbol{k}$ resistive interchange test mode, and the small-scale magnetic perturbations. The resulting dynamics are intrinsically multi-scale. Our study yields both general results—applicable to any instance of instability in a stochastic background—and quantitative results specific to this problem.

The broadly applicable findings of this paper are:

1. maintaining quasi-neutrality ($\nabla \cdot \boldsymbol{J} = 0$) at all orders reveals that electrostatic convective cell turbulence is driven at small scales by the beat of small-scale magnetic perturbations $\tilde{\boldsymbol{b}}$ and large-scale mean electrostatic potential $\bar{\varphi}$—i.e., via $\tilde{\boldsymbol{b}}\bar{\varphi}$ modulation. This effectively converts the problem to one of turbulent dynamics, and tells as that turbulence with

small-scale structure is generated.

2. the small-scale turbulence in turn modifies the large-scale mode via an effective flow viscosity and thermal diffusivity (computed by closure), as well as electrostatic scattering which is given by correlation (b) in Eq.(1.4a). Thus, the dynamics take on the character of a disparate scale interaction, with large scale $\rightarrow$ small scale modulations and feedback by small scale $\rightarrow$ large scale scattering

3. the stochastic magnetic perturbations produce a magnetic braking effect, which exerts a drag on large-scale vorticity. This effect is similar in structure to the nonlinear $\boldsymbol{J} \times \boldsymbol{B}$ force identified by Rutherford, but in our case it is produced by the stochastic magnetic perturbations.

4. the generation of small-scale cells due to $\tilde{\boldsymbol{b}}\bar{\varphi}$ interaction implies that correlation develops between the electrostatic turbulence and the ambient stochastic field—i.e. $\langle \tilde{b}_r \tilde{v}_r \rangle \neq 0$ is shown. Here $\tilde{\boldsymbol{v}}$ refers to the small-scale cell velocity. Thus, we see that the velocity fluctuations 'lock on' to the ambient static magnetic perturbations. This will necessarily affect the statistics of the turbulence.

We anticipate that results 1– 4 will be of broad interest in the context of RMP experiments.

The specific detailed calculations of this paper are:

1. the net effect of stochastic magnetic fields is to reduce resistive interchange growth—i.e., a trend toward stabilization. The increment is calculated in Eq.(1.37). Note this result is contrary to previous ones, and is a consequence of vorticity damping and diffusion emerging as the principal effects.

2. the turbulent viscosity and turbulent thermal diffusivity driven by the small-scale convective cells are calculated. The specific result is given by Eq.(1.41), with $\nu = \chi$.

3. the width of the magnetic islands when the magnetic braking effect becomes significant is calculated and given by Eq.(1.47). This differs from Rutherford's result by a factor of $k_\theta^2/k_{2\theta}^2$, on account of the multi-scale nature of the problem considered here.

4. the $\langle \tilde{b}_r \tilde{v}_r \rangle$ correlation is calculated explicitly, and given by Eq.(1.32).

Taken together, these results, *which constitute computationally testable predictions*, fully characterize the state of the system.

As for how to invalidate this theory, note that the principal theoretical predictions of this work are the reduction in interchange growth due stochasticity—especially due vorticity damping, the generation of small-scale cells, the development of finite $\langle \tilde{b}_r \tilde{v}_r \rangle$—i.e., correlation between ambient stochasticity and turbulence, and the predicted island size for magnetic braking stabilization to be significant. Thus, the absence of any of these outcomes would constitute a serious strike against the model. Computer simulation studies would be the most direct way to pursue invalidation.

In fact, the above detailed findings for resistive interchange are more general than they might seem. These fundamental results all follow from $\nabla \cdot \boldsymbol{J} = 0$, which applies to resistive interchange, drift waves, ITG, and other models. In particular, for collisional drift waves, the structure of the Ohm's law and the observation that $\nabla_\parallel J_\parallel \neq 0$ with stochastic $\tilde{\boldsymbol{b}}$ together imply $\nabla \cdot \boldsymbol{J}_\perp \neq 0$ at small scales, thus driving small-scale convective cells. Likewise, some magnetic braking effects will enter. Hence many of the results from this resistive interchange study will carry over to drift waves. The distinction between slow interchanges at low k_θ and fast interchanges at high k_θ will not carry over to drift wave turbulence. However, in the latter, adiabaticity $\alpha = k_\parallel^2 v_{the}^2/|\omega|\nu_{ei}$ may vary with k_θ, since $\omega = \omega(k_\theta)$ for drift waves. Further discussion requires analysis beyond the scope of this paper.

Previous simulation work has addressed this subject. Of particular note is the paper by Beyer, et al., which described a study of electrostatic resistive ballooning modes in a background stochastic magnetic field [67]. FIG. 1.5 is a result of that study, and contrasts the pressure

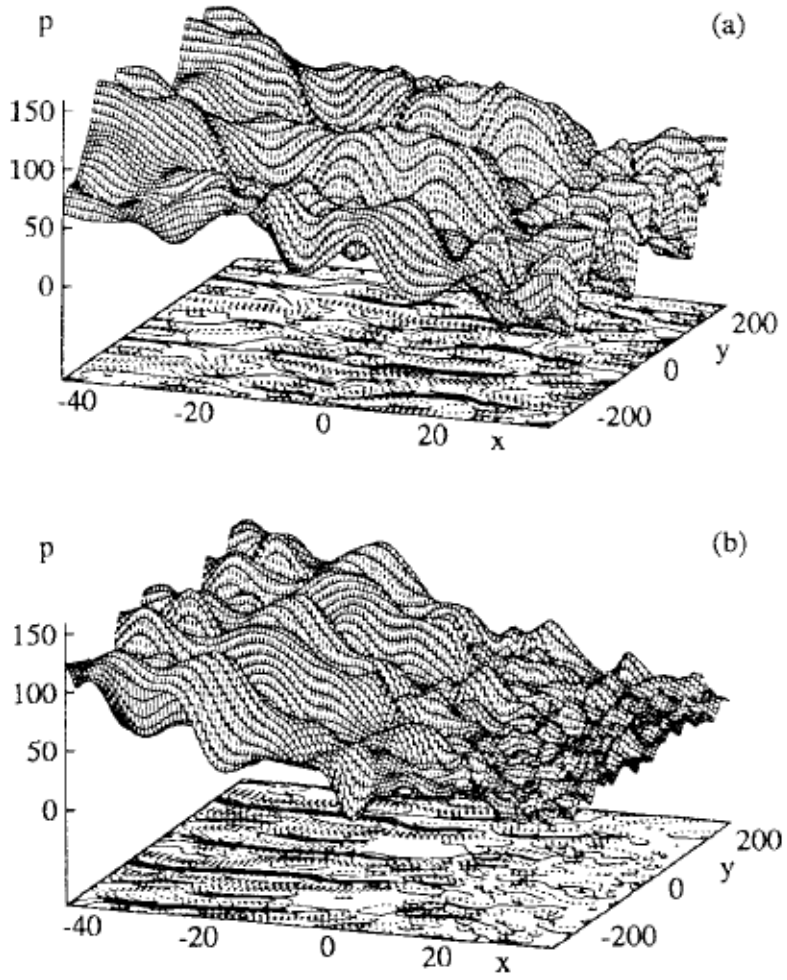

Figure 1.5. Plasma pressure in a sector at the low field side without (a) and with RMP (b) [67]. Clearly large-scale structures are suppressed in the stochastic layer, and spatial roughness increases. Reprinted from [67], with the permission of AIP Publishing.

fluctuation profile in a smooth field with one in a stochastic field. The latter clearly manifests increased small-scale structure and spatial roughness. These are consistent with our findings that small-scale convective cells will be generated by the interaction of $\tilde{\boldsymbol{b}}$ with large-scale mode. The Beyer, et al. study did not analyze this aspect of the results in detail. We have suggested that an interesting continuation and a rather precise test of our theory would be a measurement of the correlation between $\tilde{\boldsymbol{b}}$ and small-scale $\tilde{v}_r$—i.e., $\langle \tilde{b}_r \tilde{v}_r \rangle$ and a comparison to the prediction in Eq.(1.32). Similarly, a comparison of the turbulent flux $\langle \tilde{v}_r \tilde{p} \rangle$ and diffusivity χ driven at small

scales with the prediction of Eq.(1.41) would be of considerable interest.

Experimental studies of such fine scale fluctuation dynamics are understandably challenging. An interesting and relevant result was recently reported by Choi et al. [68], who compared the change in pedestal temperature fluctuation predictability (as deduced from Jensen-Shannon entropy) with RMP switched on and off. These studies focused on the putative stochastic region at the edge of RMP-induced islands in the pedestal. Results indicate that the effect of stochasticity is to reduce the Jensen-Shannon complexity [69] and predictability of the pedestal turbulence. One possible cause of this change would be that correlations between the turbulence and stochastic field develop—i.e., $\langle \tilde{b}_r \tilde{v}_r \rangle \neq 0$—as predicted here. The related generation of small-scale structure, as we suggest, is another possible cause of the drop in predictability. Of course, this finding is not entirely surprising, as it is well known that external noise can suppress or inhibit the instability characteristic of chaotic orbits [70]. Interestingly, however, Choi et al. also report an increase in bicoherence in the pedestal turbulence. We suggest that this may be due to the generation of small-scale cells, which can increase spectral transfer. A possible next step is to determine the change in the measure of fluctuation complexity implied by our results, and to compare this with the experimental findings.

In addition to the suggestions listed above, several other avenues for future research have been identified. One—of particular relevance to tokamak applications—is to consider twisted slicing mode [71] (or equivalently ballooning mode [72]) structure in a stochastic magnetic field. These modes may be thought of as extending along magnetic field lines, which now wander, stochastically. This points towards a natural critical competition between the field line decorrelation length (i.e., the counterpart of the Lyapunov exponent [73]) and the extent of the mode along the field line. A second topic is, of course, a turbulent large-scale state, as opposed to a singe mode case. Here, the presence of the stochastic field and the modulationally generated small-scale convective cells potentially open the possibility of increased nonlinear transfer, by increasing the number of triad interactions. This offers the possibility of reconciling the decrease in complexity/predictability observed in Ref. [68] with the increase in bicoherence

also observed. Finally, extension of this analysis to a kinetic description of microinstabilities should be considered. Here, since $v_\parallel \nabla_\parallel \to v_\parallel (\nabla_\parallel^{(0)} + \tilde{\boldsymbol{b}} \cdot \nabla_\perp))$, ambient stochastic perturbations will scatter particle streaming. These topics will be studied in future publications.

1.A Calculations of the growth rate of "ground state" under slow and fast interchange ordering approximations

The normalized eigen solutions to Eq.(1.12) are

$$\varphi_{\boldsymbol{k}}^{j} = \frac{\alpha_{\boldsymbol{k}}^{1/2}}{\pi^{1/4}} \frac{1}{\sqrt{2^j j!}} H_j(\alpha_{\boldsymbol{k}} x)\, e^{-\frac{(\alpha_{\boldsymbol{k}} x)^2}{2}}, \tag{1.49}$$

where

$$\alpha_{\boldsymbol{k}} = \left(\frac{S k_\theta^2}{\gamma_{\boldsymbol{k}} \tau_A L_s^2} \right)^{\frac{1}{4}},$$

and its corresponding growth rate $\gamma_{\boldsymbol{k}}$ satisfies

$$(2j+1) \sqrt{\frac{\gamma_{\boldsymbol{k}} S k_\theta^2}{\tau_A L_s}} = \left(-\gamma_{\boldsymbol{k}} k_\theta^2 + \frac{\kappa p_0 k_\theta^2}{\rho_0 L_p \gamma_{\boldsymbol{k}}} \right).$$

This is equation is not easy to solve, but in the following two limits, we can get $\gamma_{\boldsymbol{k}}$ easily.

1.A.1 Slow interchange ordering

For slow interchange, k_r is much larger than k_θ, so the term $\gamma_{\boldsymbol{k}} k_\theta^2 \varphi_{\boldsymbol{k}}$ in Eq.(1.12) can be neglected. Then Eq.(1.12) reduces to

$$-\gamma_{\boldsymbol{k}} \frac{\partial^2 \varphi_{\boldsymbol{k}}}{\partial x^2} + \frac{S}{\tau_A} \frac{k_\theta^2}{L_S^2} x^2 \varphi_{\boldsymbol{k}} - \frac{\kappa p_0 k_\theta^2}{\rho_0 L_p \gamma_{\boldsymbol{k}}} \varphi_{\boldsymbol{k}} = 0. \tag{1.50}$$

In this condition, the growth rate of the "ground state" is

$$\gamma_{\boldsymbol{k}} = S^{-\frac{1}{3}} \tau_A^{\frac{1}{3}} \tau_p^{-\frac{2}{3}} \tau_\kappa^{-\frac{2}{3}} \tilde{k}_\theta^{\frac{2}{3}},$$

which is exactly the Eq.(1.13).

1.A.2 Fast interchange ordering

For fast interchange, k_θ is much larger than k_r, so the bending term and first term of Eq.(1.12) can be neglected, which means we just need to balance the last two terms. Then we obtain

$$\gamma_{\boldsymbol{k}} = \tau_p^{-\frac{1}{2}} \tau_\kappa^{-\frac{1}{2}},$$

which is exactly the Eq.(1.14). Here we notice that growth rate of fast interchange is independent of k_θ.

1.B Kadomtsev and Pogutse's model

In K&P's work, they calculated the radial electron heat flux in a stochastic magnetic field. Originally, the heat flux is

$$\boldsymbol{q} = -\chi_\parallel \nabla_\parallel T - \chi_\perp \nabla_\perp T, \tag{1.51}$$

where $\chi_\parallel$ and $\chi_\perp$ are longitudinal and transverse thermal conductivity respectively, and $\chi_\parallel \gg \chi_\perp$. Now with stochastic magnetic field, the heat flux becomes

$$\boldsymbol{q} = -\chi_\parallel \left(\nabla_\parallel^{(0)} + \tilde{\boldsymbol{b}} \cdot \nabla\right) (\bar{T} + \tilde{T}) \left(\boldsymbol{b_0} + \tilde{\boldsymbol{b}}\right) - \chi_\perp \nabla_\perp (\bar{T} + \tilde{T}), \tag{1.52}$$

and the heat flux fluctuation $\tilde{\boldsymbol{q}}$ is

$$\tilde{\boldsymbol{q}} = -\chi_\perp \nabla_\perp \tilde{T} - \chi_\parallel \left(\nabla_\parallel^{(0)} \tilde{T} + \tilde{\boldsymbol{b}} \cdot \nabla \bar{T}\right) \boldsymbol{b_0}. \tag{1.53}$$

N.B. $\bar{T}$ is only a function of x.

Since $\nabla \cdot \boldsymbol{q} = 0$ at all scales, $\tilde{\boldsymbol{q}}$ should also be divergence-free, which gives us

$$-\chi_\parallel {\nabla_\parallel^{(0)}}^2 \tilde{T} - \chi_\perp \nabla_\perp^2 \tilde{T} = \chi_\parallel \nabla_\parallel^{(0)} (\tilde{\boldsymbol{b}} \cdot \nabla \bar{T}). \tag{1.54}$$

Table 1.1. Comparison between K&P's and C&D's Models

Analogy	K&P	C&D
Goal	$\langle q_r \rangle_{NL}$	$\gamma_k^{(1)}$
Base State	T	φ
Stochastic quantity	$\tilde{\boldsymbol{b}}$	$\tilde{\boldsymbol{b}}$
Constraint	$\nabla \cdot \boldsymbol{q} = 0$	$\nabla \cdot \boldsymbol{J} = 0$
Resulting Fluctuations	$\tilde{T}$	$\tilde{\varphi}$

Therefore, the response of $\tilde{T}$ to $\tilde{\boldsymbol{b}}$ is

$$\tilde{T}_{\boldsymbol{k}} = -\frac{\chi_\parallel i k_\parallel \tilde{b}_{r_{\boldsymbol{k}}}}{\chi_\parallel k_\parallel^2 + \chi_\perp k_\perp^2} \frac{\partial (T)}{\partial r}, \tag{1.55}$$

and the mean nonlinear radial flux is

$$\langle q_r \rangle_{NL} = -\chi_\parallel \langle \tilde{b}_r \widetilde{\boldsymbol{b} \cdot \nabla T} \rangle = -\chi_\parallel \frac{\partial \langle T \rangle}{\partial r} \sum_{\boldsymbol{k}} \frac{\chi_\perp k_\perp^2 \left| b_{r_{\boldsymbol{k}}} \right|^2}{\chi_\parallel k_\parallel^2 + \chi_\perp k_\perp^2} = -\sqrt{\chi_\parallel \chi_\perp} \langle \tilde{b}^2 \rangle l_{ac} \left\langle \sqrt{k_\perp^2} \right\rangle \frac{\partial \langle T \rangle}{\partial r}, \tag{1.56}$$

where l_{ac} is the auto-correlation length of the stochastic magnetic field. Immediately, we can see there is a comparison relation between K&P's and C&D's model, as is listed in table.(1.1).

Chapter 1, in full, is a reprint of the material as it appears in *Plasma Physics and Controlled Fusion* 64(3):035016 (2022). Cao, Mingyun; Diamond, P.H., IOP Publishing, 2022. The dissertation author was the primary investigator and author of this paper.

Chapter 2

Quasi-mode Evolution in a Stochastic Magnetic Field

2.1 Introduction

Future magnetic confinement fusion reactors, such as ITER [74], are designed to operate in the high-confinement mode for good plasma performance. As a result, dealing with the edge-localized mode (ELM)—a "side effect" of the H-mode—is one of the major concerns in fusion science today. In experiments, a technique called resonant magnetic perturbation (RMP) is widely adopted to mitigate and suppress ELMs by generating a stochastic magnetic field at the plasma edge [24, 75]. However, as turbulence evolution and transport bifurcation now happen in a background stochastic field, an increase in the L-H transition power threshold has been observed on multiple machines [76, 77, 78]. To get insight into the tripartite trade-off among confinement, heating power, and boundary control, models of turbulence dynamics [42], zonal flow evolution [41], and L-H transition [40] have been reformulated in the presence of extrinsic stochasticity. All these theories are either based on or closely relevant to a fundamental question: how does an ambient stochastic magnetic field modify plasma turbulence and the underlying instability process? This paper entrances previous work on this subject [79] by delving deeper into the geometric complexities.

Experiments play a critical role in illuminating this question. Many intriguing phenomena, such as the significant reduction in the edge plasma density (density pump-out), form part of

our current understanding of plasma confinement with the influence of RMP. In addition, there has been some progress in experimental studies on the effects of stochastic magnetic fields on plasma turbulence. For instance, an increase in the pedestal fluctuation level is observed in the RMP ELM suppression phase [80]. However, due to the technical difficulty in turbulence diagnostics, these studies primarily rely on the spectral analysis, which alone fails to fully capture the changes in the states of turbulence when RMP is implemented. Given that plasma turbulence is intermittent, more information is needed to characterize the effects of stochastic magnetic fields on its statistical behaviors.

In information theory, complexity-entropy analysis is a useful method that can quantify the predictability and structural intricacy of time series and signals. In this approach, Jensen-Shannon complexity C_{JS} serves as a metric of a system's complexity, which is defined as

$$C_{\mathrm{JS}} = HQ. \tag{2.1}$$

Here H is the permutation entropy, a measure of the missing information of a system, and Q is the Jensen-Shannon divergence, a measure of the distance of a system from thermal equilibrium state. C_{JS}, H and Q are all functionals of the signals recorded. As a side note, it can be proved that this permutation entropy H coincides with the Kolmogorov–Sinai entropy for piecewise monotone interval maps [81]. One important feature of this approach is its user-friendliness. For a time series obtained from experiments, the calculation of its Jensen-Shannon complexity is much simpler compared to other metrics, for example, the Kolmogorov-Sinai entropy [82]. Another advantage of this definition is that the number given by C_{JS} aligns with people's intuitive perception of a system's complexity. For instance, the Jensen-Shannon complexity metric reflects the widely-held notion that both the white noise and perfect crystals are 'simple' systems. Specifically, the white noise has a high entropy but low complexity, because there is no discernible structure. In contrast, a perfect crystal has low entropy and also low complexity, as it is perfectly regular. Generally, deterministic chaotic systems, such as the logistic map, always have high

complexity, while noisy signals, like Brownian motion, are associated with low complexity [69]. This fact enables us to distinguish chaos from noise. Consequently, complexity-entropy analysis has been applied to various areas, including hydrology [83], economy [84], semantics [85], etc. As a special case of chaos, turbulence is intrinsically different from noise: the former exhibits a spectral energy flux in the k-space, while the energy emission and absorption in the latter case are *local* in k. Given the significance of turbulence in MFE, the complexity-entropy analysis has also been noticed by the fusion community. Using this approach, the chaotic nature of the edge fluctuations in L-mode, H-mode, and I-mode has been identified [86, 87, 88]. However, as reported by Choi et al., the rescaled Jensen-Shannon complexity of the temperature fluctuations at the pedestal top in the RMP ELM suppression phase is *reduced* relative to that in the natural ELM-free phase and the RMP ELM mitigation phase [68]. *This indicates that the edge plasma turbulence becomes more "noisy" when ELM is suppressed by RMP.* A fundamental change in the statistical dynamics of the turbulence due to stochastic field is thus implied. Additionally—and somewhat paradoxically—an *increase* in the bicoherence of the pedestal turbulence was also observed when system entered the RMP ELM suppression regime, as shown in figure 2.1. These observations further underscore the necessity of studying the fundamentals of plasma instabilities and turbulence in a stochastic magnetic field.

In our previous work [79], we probed this question by developing a multi-scale model which maintains $\nabla \cdot \boldsymbol{J} = 0$ at all scales. The chosen object of that research is the resistive interchange mode [59, 60, 61], primarily due to its tractability. While that model provides *generic* and *valuable* physical insights, its quantitative results may not be especially convincing, due to the geometric simplicity of the interchange modes. As the peeling-ballooning mode is a probable candidate for the origin of ELM [89], the ballooning mode is a more relevant instability to examine. However, apart from the inherent higher complexity of the ballooning mode (compared to the interchange mode), there is another hard nut to crack: *while models for ballooning modes in a tokamak are set up in toroidal geometry* [90], *theories involving resonant magnetic perturbations often are formulated in terms of resonant surfaces in a cylindrical*

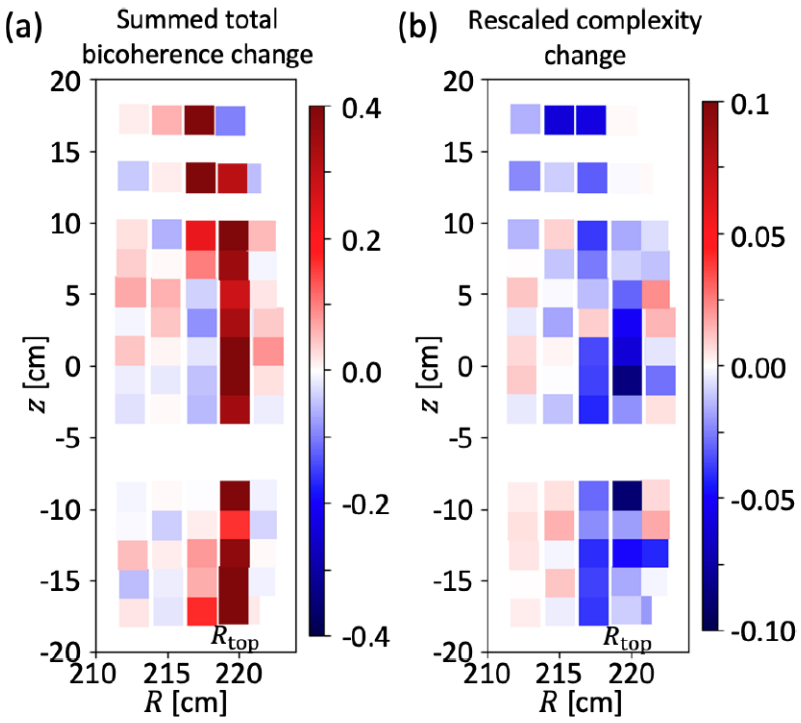

Figure 2.1. Changes of the summed total bicoherence (a) and rescaled complexity (b) of the electron temperature fluctuation between the ELM mitigation and the initial suppression phases. Reprinted from [68], with the permission of AIP Publishing.

geometry [91]. To develop a comprehensive theory that encompasses both the ballooning mode and RMP, these two different geometries must be reconciled. For a stellarator, due to the lack of the toroidal symmetry, system is fully three-dimensional [92]. Therefore, theories of ballooning mode [93, 94] and resonant magnetic perturbations [95, 96] have been established in fully three-dimensional geometries. Meanwhile, codes for MHD simulations are extended to the stellarator geometry, such as M3D-C^1 [97], are developed. While it may seem that there is no problem of geometry disparity in the case of stellarator, a direct theoretical study on the ballooning mode in a stochastic magnetic field in a fully three-dimensional geometry is intimidating and intractable. To get results which may be readily understood, we need to compromise on the geometric complexity and choose to study this reduced problem. For the reasons given above, in this work, we will work on the cylindrical geometry model, and the strategy for the geometry reconciliation

is to replace the ballooning mode with its counterpart in a cylinder, i.e., the quasi-mode. Figure 2.2 is an illustration of the mode structures of the quasi-mode and the ballooning mode. It can be seen from figure 2.2(a) that a quasi-mode, denoted by red envelope curves, is composed of vertically localized (resistive) interchange modes, represented by yellow columns. Likewise, as shown in figure 2.2(b), a ballooning mode, denoted by the red dotted curve, is a coupling of localized poloidal harmonics (blue hills). Hence, we conclude that *a quasi-mode in a cylinder resembles a ballooning mode in a torus.* As both the quasi-mode and the stochastic magnetic field reside in a cylindrical geometry, studying a quasi-mode in a stochastic magnetic field is manageable.

In this paper, we present a theory of the quasi-mode in a static, ambient stochastic magnetic field. We need to emphasize that here we mainly focus on the strong chaos regime, in which the Chirikov island overlap parameter is large, i.e.,

$$\sigma_{\text{Chirikov}} = \frac{\delta_{m,n} + \delta_{m',n'}}{\Delta_{m,n;m',n'}} \gg 1, \tag{2.2}$$

where $\delta_{m,n}$ and $\delta_{m',n'}$ are the half width of the magnetic islands at $q(r_{m,n}) = m/n$ and $q(r_{m',n'}) = m'/n'$ resonant surfaces, and $\Delta_{m,n,m',n'}$ is the distance between these two surfaces. This assumption indicates RMP current is relatively high in experiments. Hence, while the flux surfaces in the core remain unperturbed, the edge stochastic magnetic field can be regarded as strongly chaotic. In reality, however, with the application of RMP, there is no such thing as a sharp boundary separating the core region filled with nested flux surfaces from the edge region where field lines are chaotic. Between these two regions, there is an intermediate region, referred to as "critical chaos", in which structures like island chains and cantori (broken KAM surfaces) exist [98]. As island chains can degrade confinement and cantori can serve as effective barriers to field-line transport [99], these structures usually have non-negligible effects. To maintain the analytical tractability of our model, we suppose the field lines in the chaotic layer are truly chaotic and don't take the effects of island chains and cantori into consideration. The structure of

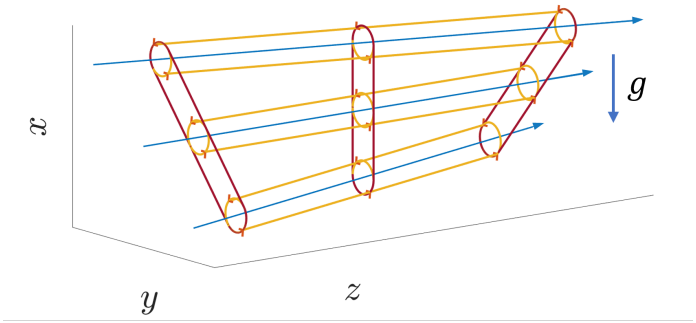

(a)

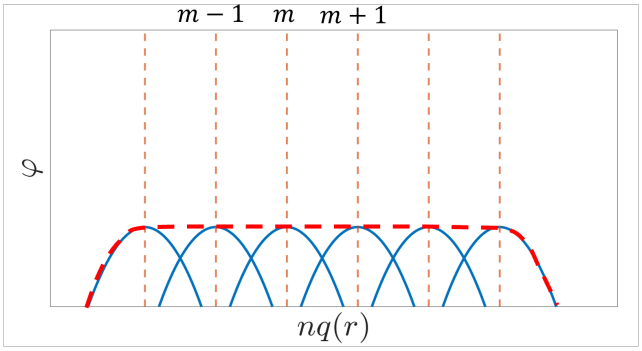

(b)

Figure 2.2. The similarity between quasi-mode and ballooning mode. (a) A depiction of the quasi-mode. The blue lines are magnetic field lines. The yellow columns are fluid filaments of gravitational interchange modes at different horizontal surfaces. The red envelope curves of these fluid filaments represent the convective cells of the quasi-mode. So a quasi-mode can be viewed as a wave-packet of gravitational interchange modes. (b) A simple sketch of the ballooning mode. The blue hills are poloidal harmonics localized at a sequence of resonant surfaces. Ballooning mode (red dotted curve) is a coupling of these harmonics due to toroidicity effect.

our model can be summarized by the flowchart in figure 2.3. At the large-scale, a quasi-mode is driven by the magnetic curvature and the mean density gradient. When a background stochastic magnetic field is imposed, to maintain $\nabla \cdot \boldsymbol{J} = 0$, small-scale convective cells, also referred to as the microturbulence, are driven by the beat of the quasi-mode with the stochastic magnetic field. This microturbulence has a finite correlation with the magnetic perturbations, which can account for the reduced complexity observed in Choi's experiments. We can think of it as the suppression of the instability characteristic of a chaotic system by external noise [100]. The microturbulence further leads to the emergence of a turbulent viscosity and a turbulent diffusivity.

The effects of the stochastic magnetic field on the quasi-mode are mainly reflected in three distinct ways: (1) stochastic magnetic fields can enhance the effective plasma inertia and reduce the effective drive, thus opposing the mode growth; (2) the turbulent viscosity and the turbulent diffusivity produced by the microturbulence can damp the quasi-mode by increasing mixing; (3) the microturbulence can react to the evolution of the quasi-mode, consequently leading to the formation of a feedback loop in the system. Though this reaction tends to destabilize the quasi-mode, its effect can be proved to be negligible as compared to (1). Combining (1), (2), and (3), the net effect of stochastic magnetic field on the quasi-mode is to slow the mode growth.

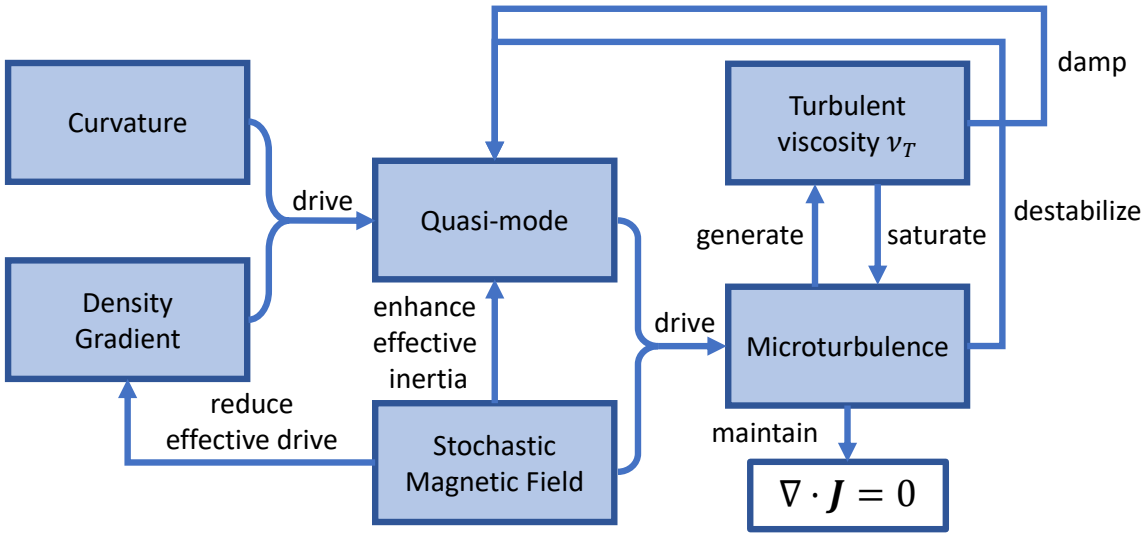

Figure 2.3. Multi-scale feedback loops of quasi-mode and small-scale convective cells.

The remainder of this paper is organized as follows. In section 2.2, we briefly review the basics of the quasi-mode and demonstrate the resemblance between the quasi-mode and the ballooning mode. The model of the quasi-mode in an externally prescribed stochastic magnetic field is then formulated in section 2.3. Quantitative results, including the correction to the growth of the quasi-mode mode, the correlation $\langle \tilde{v}_x \tilde{\boldsymbol{b}} \rangle$, and the scaling of the turbulent viscosity ν_T, are also given in this section. In section 2.4, we pin down the sign of the growth rate correction and discuss its underlying physics. The consistency between our theory and existing simulations and experiments is also discussed there. This paper concludes with the lessons we have learned about

the dynamics of the quasi-mode and what we can infer about the dynamics of the ballooning mode, and with suggestions for future experimental and theoretical investigations. Expressions for the operators in this work, as well as a detailed calculating procedure of the Jensen-Shannon complexity, are attached in the Appendix.

2.2 Revisiting of the quasi-mode

As mentioned in section 2.1, one challenge in studying the ballooning mode in a stochastic magnetic field is the difference in geometries upon which theories of the ballooning mode and resonant magnetic perturbations are based. The similarities between the quasi-mode and the ballooning mode allow us to study quasi-mode first and then extend the results to the ballooning mode. To elucidate the validity of this idea, fundamentals of the quasi-mode and the relation between the quasi-mode and the ballooning mode are discussed quantitatively in this section.

2.2.1 Physical picture of the quasi-mode

The quasi-mode was first identified by Roberts and Taylor in 1965 [71]. In a nutshell, a quasi-mode is an effective wave-packet of gravitational interchange modes in a sheared magnetic field, as depicted in figure 2.2. The term "quasi-mode" implies that it is not an eigenmode, so it will eventually disperse. But as will be discussed in section 2.2.3, the interchange modes constituting the quasi-mode are highly degenerate. So the quasi-mode is capable of maintaining its shape before entering the nonlinear regime, and it is fair to treat quasi-mode as a "true mode". Unlike the gravitational interchange mode, which is localized at a specific horizontal surface, the convective cells of the quasi-mode (red envelopes in figure 2.2) have a broad mode structure in the x (vertical) direction. Since the main magnetic field has a small but finite shear, the fluid filaments or "flux tubes" (yellow columns in figure 2.2) must rotate around the vertical axis x when rising or falling. This rotation allows them to keep aligned with the local magnetic field so as to minimize the field distortion. Another name for the quasi mode, "twisted slicing mode", originates from this twisted interchange motion of the fluid filaments.

When the system is infinitely extended in the z direction, the quasi-mode, unlike gravitational interchange modes which are spatially periodic in z, exhibits a finite mode length in the direction of the main field. As illustrated in figure 2.4, the vertical and twisted sheets, filled alternately in red and blue, represent the envelope surfaces of the convective cells of the quasi-mode at various positions along the main field line. These convective cells correspond to the red envelope curves shown in figure 2.2. The colors red and blue represent the upward and downward motions of the plasma, respectively. The darker the shade, the faster the motion. From the change in color, it is evident that the plasma motion slows down (exponentially) as it moves away from the origin along the z axis. The length and direction of each arrow in figure 2.4 denote the magnitude and direction of the velocity field at the corresponding spatial position.

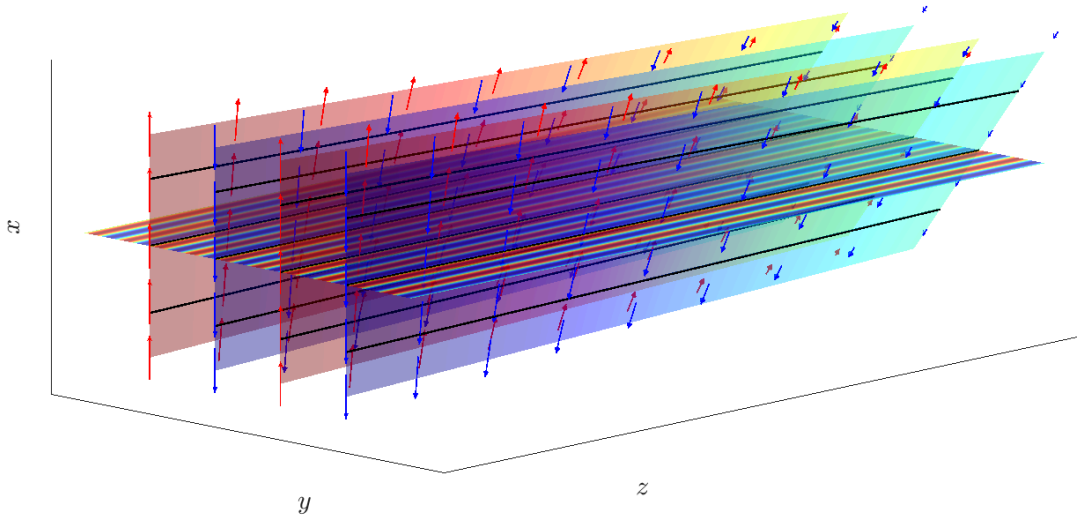

Figure 2.4. The velocity field of the quasi-mode and the graphic example of one of the magnetic perturbations. The vertical twisted sheets are envelope surfaces of the convective cells of the quasi-mode. The arrows are the visualization of the velocity field. The horizontal plane is a simple sketch of the magnetic perturbation at one particular resonant surface.

The finite mode length of the quasi-mode in the main field direction can be explained from the viewpoint of energy conservation. In the presence of magnetic shear, fluid filaments will rotate with respect to x axis as they move vertically. The rotational kinetic energy of

these filaments would diverge if their mode length is equal to the length of the system (i.e., infinity). Hence, the mode length of the quasi-mode automatically adjusts to a finite value Δ. This adjustment is dictated by a balance among the rate of the release of the gravitational potential energy, the rate of the resistive dissipation, and the rate of the increase of the rotational kinetic energy. The underlying rationale is that to have a finite rotational kinetic energy, the quasi-mode must possess a finite length in z. This condition subsequently leads to an increase in the resistive dissipation. The increase in the rotational kinetic energy and dissipation is at the expense of the gravitational potential energy.

2.2.2 Quantitative description of the quasi-mode

The dynamics of both the gravitational interchange mode and the quasi-mode are governed by the same set of equations, i.e., resistive MHD equations. In this work, an incompressible plasma subject to a uniform gravitational field in the negative x direction is considered, as shown in figure 2.2. A uniform magnetic field B_0 is exerted in the z direction, along with a transverse field $B_y = sxB_0$, where s is a constant. The magnetic shear is assumed to be weak, i.e., $sx \ll 1$.

The linearized equations for the quasi-mode are the momentum equation, the induction equation, and the continuity equation

$$\rho_0 \frac{\partial \boldsymbol{v}}{\partial t} = -\nabla p + \frac{1}{4\pi}(\nabla \times \boldsymbol{B}) \times \boldsymbol{B_0} + \frac{1}{4\pi}(\nabla \times \boldsymbol{B_0}) \times \boldsymbol{B} + \rho \boldsymbol{g}, \tag{2.3}$$

$$\frac{\partial \boldsymbol{B}}{\partial t} = (\boldsymbol{B}_0 \cdot \nabla)\boldsymbol{v} - (\boldsymbol{v} \cdot \nabla)\boldsymbol{B}_0 + \frac{\eta}{4\pi}\nabla^2 \boldsymbol{B}, \tag{2.4}$$

$$\frac{\partial \rho}{\partial t} = -\boldsymbol{v} \cdot \nabla \rho_0 = -v_x \alpha \rho_0. \tag{2.5}$$

Note that the Ampère's law $\nabla \times \boldsymbol{B} = 4\pi \boldsymbol{J}$ is used to eliminate $\boldsymbol{J}$ in equation (2.3). In equations (2.3) through (2.5), $\boldsymbol{B}_0 = (0, sx, 1)B_0$ is the main field. $\boldsymbol{g} = -g\hat{\boldsymbol{x}}$ is the "gravity", which can be identified in terms of the pressure p_0 and the magnetic curvature R_c by $g \sim 2p_0/\rho_0 R_c$. η is the plasma resistivity, which is assumed to be uniform in the system. α characterizes the gradient of

the mean density, which acts as the source of free energy. In this case, ρ_0 increases linearly with x, so α is a constant. The Boussinesq approximation allow us to treat ρ_0 as uniform in equations (2.3) and (2.5). In equation (2.4), the ratio of $\partial_t \boldsymbol{B}$ to $\eta\nabla^2\boldsymbol{B}/4\pi$ is of order $\beta = 8\pi p_0/B_0^2$. In the limit of $\beta \ll 1$, we can eliminate the term $\partial_t \boldsymbol{B}$, leading to the equation

$$\boldsymbol{B}_0 \cdot \nabla \boldsymbol{v} + \frac{\eta}{4\pi}\nabla^2 \boldsymbol{B} = 0, \tag{2.6}$$

where the term $\boldsymbol{v} \cdot \nabla \boldsymbol{B}_0$ is also disregarded due to the slow spatial variation of $\boldsymbol{B}_0$. Applying operator $(\nabla \times \nabla \times)$ to equation (2.3) yields

$$\rho_0 \frac{\partial \nabla^2 \boldsymbol{v}}{\partial t} = \frac{1}{4\pi}\boldsymbol{B}_0 \cdot \nabla\left(\nabla^2 \boldsymbol{B}\right) - \left[\nabla(\nabla \cdot \rho \boldsymbol{g}) - \nabla^2 \rho \boldsymbol{g}\right]. \tag{2.7}$$

Substituting equation (2.5) and (2.6) into equation (2.7) and taking the dot product with $\hat{\boldsymbol{x}}$, we obtain the following eigenmode equation

$$\rho_0 \eta \frac{\partial^2 \nabla^2 v_x}{\partial t^2} + (\boldsymbol{B}_0 \cdot \nabla)^2 \frac{\partial v_x}{\partial t} - \alpha g \rho_0 \eta \left(\frac{\partial^2}{\partial y^2} + \frac{\partial^2}{\partial z^2}\right) v_x = 0, \tag{2.8}$$

where $\boldsymbol{B}_0 \cdot \nabla = B_0\left(\frac{\partial}{\partial z} + sx\frac{\partial}{\partial y}\right)$. In order to exploit the linear magnetic shear and simplify the operator $\boldsymbol{B}_0 \cdot \nabla$, a twisted coordinate system, defined by the following transformation, is introduced:

$$\xi = x, \quad \chi = y - sxz, \quad \zeta = z. \tag{2.9}$$

The operators appearing in equation (2.8) also need to be transformed accordingly (see 2.B). For the quasi-mode, instead of employing the Fourier expansion in the z direction, a more generalized form of the solutions is adopted, as shown below:

$$v_x = v(\zeta)\exp(\gamma_{\boldsymbol{k}} t + ik_x \xi + ik_y \chi). \tag{2.10}$$

Plugging equation (2.10) into equation (2.8), we get

$$\left(1+\varepsilon^2 q\right)\frac{1}{k_y^2}\frac{\partial^2 v}{\partial\zeta^2}-\frac{2\varepsilon^2 qis\xi}{k_y}\frac{\partial v}{\partial\zeta}-\varepsilon^2\left[q\left(1+s^2\xi^2\right)+\frac{\gamma_k^2}{\alpha g}s^2\zeta^2-\frac{\gamma_k^2}{\alpha g}\left(\frac{k_x^2}{k_y^2}-2s\zeta\frac{k_x}{k_y}\right)\right]v=0, \tag{2.11}$$

where

$$\varepsilon^2=\frac{\alpha g\rho_0\eta}{\gamma_k B_0^2},\quad q=\frac{\gamma_k^2}{\alpha g}-1. \tag{2.12}$$

In the regime where $\varepsilon\ll 1$ (long mode length of the quasi-mode in the z direction), $k_x/k_y\ll 1$ (broad mode structure of the quasi-mode in the x direction), and $s\xi\ll 1$ (weak magnetic shear), equation (2.11) is simplified to

$$\frac{d^2v}{d\zeta^2}-\frac{\gamma_k\tau_A}{S}\left(sk_y\right)^2\zeta^2 v+\frac{\gamma_k\tau_A k_y^2}{S}\left(\frac{\alpha g}{\gamma_k^2}-1\right)v=0, \tag{2.13}$$

where S is the Lundquist number defined as the ratio of the resistive diffusion time, $\tau_R=4\pi a/\eta$, to the Alfvén time, $\tau_A=a/(B_0/4\pi\rho_0)^{1/2}$. As equation (2.13) is similar in form to the equation for a quantum harmonic oscillator, its solutions are given by

$$v=v_j(\zeta)=2^{-\frac{j}{2}}H_j\left(\frac{\zeta}{\Delta}\right)\exp\left(-\frac{\zeta^2}{2\Delta^2}\right), \tag{2.14}$$

where H_j are the Hermite polynomials, Δ is the characteristic mode length along the main field. In the case of the slow interchange, i.e. $\gamma_k^2\ll\alpha g$, the growth rate of this mode is

$$\gamma_k^{(j)}=(\alpha g)^{\frac{2}{3}}\left(\frac{\tau_A k_y^2}{Ss^2}\right)^{\frac{1}{3}}(2j+1)^{-\frac{2}{3}}, \tag{2.15}$$

and the corresponding Δ is

$$\Delta_j=\frac{1}{(\alpha g)^{\frac{1}{6}}}\left(\frac{S}{\tau_A k_y^2}\right)^{\frac{1}{3}}\frac{1}{s^{\frac{1}{3}}}(2j+1)^{\frac{1}{6}}. \tag{2.16}$$

As the wavenumber k_x is irrelevant in equations (2.15) and (2.16) due to the fact that $k_x \ll k_y$, the x-dependence of the solutions can be replaced by any slowly varying function $g(x)$, leading to the solutions of equation (2.13) in the form of

$$v_x(x,y,z) = g(x)v_j(z)\exp\left[ik_y(y-sxz)\right]. \tag{2.17}$$

In section 2.3, *the function $g(x)$ is taken as a constant*, which is a reasonable approximation as long as we are not close to the system boundary.

2.2.3 Relation between quasi-mode and ballooning mode

The quasi-mode can be used as a surrogate for the ballooning mode because their share similar mode structures. More specifically, both of them are composed of localized modes. It can be shown that the expression for the quasi-mode given by equation (2.17) is just a linear superposition of the vertically localized gravitational interchange modes. Now we seek solutions of equation (2.8) that are periodic in z and of the form

$$v_x = v_g(x)\exp\left(\tilde{\gamma}_{\boldsymbol{k}}t + ik_y y + ik_z z\right). \tag{2.18}$$

By adopting this form and solving equation (2.8), the eigenmodes are given by

$$v_g(X) = u_j(X) = 2^{-\frac{j}{2}}H_j\left(\frac{X}{\delta_{\boldsymbol{k}}}\right)\exp\left(-\frac{X^2}{2\delta_{\boldsymbol{k}}^2}\right), \tag{2.19}$$

with their growth rates in the slow interchange limit given as

$$\tilde{\gamma}_{\boldsymbol{k}}^{(j)} = (\alpha g)^{\frac{2}{3}}\left(\frac{\tau_A\tilde{k}^4}{Ss^2k_y^2}\right)^{\frac{1}{3}}(2j+1)^{-\frac{2}{3}}, \tag{2.20}$$

where

$$X = x + \frac{k_z}{sk_y}, \quad \delta_{\boldsymbol{k}} = \left(\frac{\gamma_{\boldsymbol{k}} \tau_A}{Ss^2 k_y^2} \right)^{\frac{1}{4}}, \quad \tilde{k}^2 = k_y^2 + k_z^2. \tag{2.21}$$

These modes are localized around resonant surfaces where $\boldsymbol{k} \cdot \boldsymbol{B}_0 = 0$. For two modes with the same k_y but localized at different heights separated by x_0, their growth rates differs only by $\delta\gamma/\gamma \sim (sx_0)^2 \ll 1$. The strong degeneracy of these localized gravitational interchange modes leads to a long "life-time" of the quasi-mode. Consequently, the sum of a series of interchange modes in the "ground state" ($j = 0$), each sharing the same k_y but centered at various resonant surfaces, can be written as

$$u(x,y,z,t) = \exp(ik_y y) \int f(k_z) \exp\left[ik_z z - \frac{(x-x_0)^2}{2\delta_0^2} \right] \exp(\gamma_{\boldsymbol{k}} t) dk_z, \tag{2.22}$$

where $f(k_z)$ is a slowly varying weight function, and $x_0 = -k_z/sk_y$. If we let $f(k_z)dk_z = -g(x_0)dx_0$, equation (2.22) reduces to

$$u(x,y,z,t) \cong \delta\sqrt{2}\pi g(x) \exp\left[ik_y(y - sxz) - \frac{(sk_y\delta_0 z)^2}{2} + \gamma t \right]. \tag{2.23}$$

The equivalence between equation (2.17) and equation (2.23) clearly exhibits the relation between the quasi-mode and the gravitational interchange mode. Note that $1/\Delta \cong sk_y\delta_{\boldsymbol{k}} \ll k_y$, suggesting that the narrower the interchange mode, the longer the quasi-mode.

Analogous to the quasi-mode, which acts as a wave-packet of the interchange modes, the ballooning mode is a coupling of poloidal harmonics localized at a sequence of resonant surfaces (see figure 2.2). There are two different but equivalent methods to investigate the "land of ballooning": ballooning mode representation [101] and Bloch eigenmode equation [102]. Here the former one is adopted to illuminate the similarity between the ballooning mode and the quasi-mode.

The most persistent instabilities in toroidal axisymmetric plasmas are those characterized by a short wavelength perpendicular to the magnetic field and a long wave lengths parallel to it,

such as the ballooning mode. The ordinary representation of this kind of modes is in the eikonal form [103]

$$\varphi(r,\chi,\phi) = F(r,\chi)\exp\left[in(\phi - \int^{\chi} \nu d\chi)\right], \tag{2.24}$$

where χ is a poloidal, angle-like coordinate, $F(r,\chi)$ is a slowly varying function, ν is a parameter containing the information of magnetic geometry and related to the 'safety factor' by $q = 2\pi \oint \nu d\chi$. Note that the expression for the quasi-mode, given by equation (2.17), indeed takes this eikonal form. But in equation (2.17), the poloidal wavenumber k_y takes the place of the toroidal mode number n in equation (2.24). This is because in a torus, the toroidal symmetry is preserved whereas the poloidal symmetry is broken by the toroidicity effect. Hence, only the toroidal mode number n continues to be a valid "quantum" number. It can be proved that in the presence of magnetic shear, the eikonal form given by equation (2.24) contradicts with the demand of periodicity in the poloidal angle across all values of r, unless we assume $F(r,\chi)$ is not a slowly varying function. To reconcile this contradiction, in 1979, Connor, Hastie, and Taylor proposed the following ballooning mode transformation [101]

$$\varphi(r,\theta) = \sum_{m=-\infty}^{+\infty} e^{im\theta} \int_{-\infty}^{+\infty} e^{-im\eta}\hat{\varphi}(r,\eta)d\eta, \tag{2.25}$$

so that if $\hat{\varphi}(r,\eta)$ is a solution of

$$L(r,\eta)\hat{\varphi}(r,\eta) = \lambda\hat{\varphi}(r,\eta), \tag{2.26}$$

then $\varphi(r,\theta)$ will be a solution of

$$L(r,\theta)\varphi(r,\theta) = \lambda\varphi(r,\theta), \tag{2.27}$$

where $L(r,\theta)$ and $\varphi(r,\theta)$ are periodic in θ. This transformation effectively map the domain of $\theta \in (-\pi,\pi)$ onto the covering space of $\eta \in (-\infty,\infty)$, with η interpreted as the coordinate in the

main field direction. After eliminating the periodicity requirement for $\hat{\varphi}$, it is feasible to express it in the eikonal form

$$\hat{\varphi}(r,\eta,\phi) = \varphi_0(r,\eta)\exp\left[-in\left(\phi - q\eta\right)\right], \tag{2.28}$$

where $\int^{\eta} \nu d\eta$ is approximated as $q\eta$ (i.e., the phase shift is neglected). Substituting equation (2.28) into equation (2.24), we obtain [104]

$$\varphi(r,\theta) = \sum_{m=-\infty}^{+\infty} \varphi_m(r, nq-m)e^{im\theta}, \tag{2.29}$$

where φ_m is defined as

$$\varphi_m(r, nq-m) = \int_{-\infty}^{+\infty} \frac{d\eta}{2\pi}\varphi_0(r,\eta)e^{i(nq-m)\eta}. \tag{2.30}$$

Since φ_0 is a slowly varying function of η, its Fourier transform φ_m is localized near the resonant surface where $q(r_{m,n}) = m/n$. Equation (2.29) indicates that a ballooning mode $\varphi(r,\theta)$ can be viewed as a coupling of a sequence of poloidal harmonics φ_m, as sketched in figure 2.2. This clearly demonstrates the resemblance between a quasi-mode wave-packet in a cylinder (or slab) and a ballooning mode in a torus. Therefore, by studying the quasi-mode in a stochastic magnetic field, we can provide instructive insights into the effects of stochastic magnetic field on ballooning mode.

2.3 Model development

In this section, a multi-scale model for the quasi-mode in a stochastic magnetic field is presented. We show that the small-scale convective cells, i.e., the microturbulence, are driven when the stochastic magnetic field is introduced to the dynamics of the quasi-mode, so as to maintain $\nabla \cdot \boldsymbol{J} = 0$ at all scales. The correlation between the velocity fluctuations and the magnetic perturbations, the correction to the growth rate of the quasi-mode, and the scaling of the turbulent viscosity are also given.

2.3.1 Generation of the microturbulence

Compared to the eigenmode equation (2.8), the vorticity equation is better suited to demonstrate the generation of the microturbulence, as it is actually the equation $\nabla \cdot \boldsymbol{J} = 0$ in detail [105], and thus naturally guarantees quasi-neutrality. Taking the curl of the momentum equation (2.3), the vorticity equation is written as

$$\underbrace{-\frac{\rho_0}{B_0^2}\frac{\partial}{\partial t}\nabla_\perp^2\varphi}_{\nabla_\perp\cdot\boldsymbol{J}_{pol}}\underbrace{-\frac{1}{\eta}\left(\boldsymbol{b}_0\cdot\nabla\right)^2\varphi}_{\nabla_\parallel J_\parallel}\underbrace{+\frac{g}{B_0}\frac{\partial}{\partial y}\rho}_{\nabla_\perp\cdot\boldsymbol{J}_{PS}}=0, \tag{2.31}$$

where φ is the electrostatic potential. $J_\parallel$ is eliminated by exploiting the linearized Ohm's law [106]

$$J_\parallel = \frac{1}{\eta}\left(\boldsymbol{b}_0\cdot\nabla\right)\varphi = \frac{1}{4\pi}\left(\nabla\times\boldsymbol{B}\right)_\parallel, \tag{2.32}$$

in the $\beta \ll 1$ limit (electrostatic case). Combining it with the continuity equation (2.5), we get

$$\rho_0\eta\frac{\partial^2}{\partial t^2}\nabla_\perp^2\varphi + \frac{\partial}{\partial t}B_0^2\left(\boldsymbol{b_0}\cdot\nabla\right)^2\varphi - \alpha g\rho_0\eta\frac{\partial^2}{\partial y^2}\varphi = 0. \tag{2.33}$$

Although there may appear to be a slight difference, equation (2.33) is, in fact, equivalent to equation (2.8), as

$$\left|\frac{\rho_0\eta\,\partial_t^2\left(\boldsymbol{b}_0\cdot\nabla\right)^2\varphi}{\partial_t B_0^2\left(\boldsymbol{b}_0\cdot\nabla\right)^2\varphi}\right| = \frac{\rho_0\eta\gamma}{B_0^2} = \varepsilon^2\frac{\gamma_{\boldsymbol{k}}^2}{\alpha g} \ll 1, \quad \left|\frac{\partial_z^2\varphi}{\partial_y^2\varphi}\right| \cong (s\delta)^2 \ll 1. \tag{2.34}$$

With the introduction of the magnetic perturbations, magnetic field lines become chaotic. Following a standard low-β, normal aspect ratio ordering, we have

$$\tilde{b}_\perp = \tilde{B}_\perp/B_0 \sim \varepsilon, \quad \tilde{b}_\parallel = \tilde{B}_\parallel/B_0 \sim \varepsilon^2, \quad \nabla_\perp \sim 1, \quad \nabla_\parallel \sim \varepsilon, \tag{2.35}$$

where ε is a small number [57]. Then we introduce the stochastic magnetic potential $\tilde{A}$ and rewrite the perturbed magnetic as

$$\tilde{\boldsymbol{b}} = \tilde{\boldsymbol{B}}/B_0 = \hat{\boldsymbol{z}} \times \nabla \tilde{A} + \tilde{b}_{\parallel} \hat{\boldsymbol{z}}, \tag{2.36}$$

whose divergence is then

$$\nabla \cdot \tilde{\boldsymbol{b}} = \partial_{\parallel} \tilde{b}_{\parallel} \sim \varepsilon^3. \tag{2.37}$$

Hence, with the neglect of $\tilde{B}_{\parallel}$ and its effects, $\nabla \cdot \tilde{\boldsymbol{b}} = 0$ remains accurate to the second order. Effects of $\tilde{B}_{\parallel}$ need to be reconsidered in the case of stochasticity in a spherical torus [58]. Then, the total magnetic field is approximated as the sum of a main field $\boldsymbol{B}_0$ and a perturbed field $\tilde{\boldsymbol{B}}_{\perp}$, i.e., $\boldsymbol{B}_{tot} = \boldsymbol{B}_0 + \tilde{\boldsymbol{B}}_{\perp}$. Here $\tilde{\boldsymbol{B}}_{\perp}$ is constituted by a series of high-$\boldsymbol{k}$ magnetic perturbations that are highly localized at resonant surfaces and densely packed, i.e., $\sigma_{\text{Chirikov}} \gg 1$ (strong chaos). The horizontal plane in figure 2.4 depicts one such perturbation at a specific resonant surface. The stochastic magnetic field is incorporated into our model by modifying the parallel gradient operator to

$$\nabla_{\parallel} = \nabla_{\parallel}^{(0)} + \tilde{\boldsymbol{b}} \cdot \nabla_{\perp}, \tag{2.38}$$

where $\nabla_{\parallel}^{(0)} = \partial_{\zeta}$ is the gradient along the main field, $\tilde{\boldsymbol{b}} = \tilde{\boldsymbol{B}}_{\perp}/B_0$, and $\tilde{\boldsymbol{b}} \cdot \nabla_{\perp}$ is the gradient along the perturbed field. With this modification, the parallel current density becomes

$$\boldsymbol{J}_{\parallel} = -\frac{1}{\eta} \left[\nabla_{\parallel}^{(0)} + \tilde{\boldsymbol{b}} \cdot \nabla_{\perp} \right] \bar{\varphi} \left(\boldsymbol{b}_0 + \tilde{\boldsymbol{b}} \right), \tag{2.39}$$

where $\bar{\varphi}$ denotes the electrostatic potential of the low $\boldsymbol{k}$ quasi-mode. Equation (2.39) implies that the plasma flow along the chaotic magnetic field lines results in a small-scale current density fluctuation $\tilde{\boldsymbol{J}}_{\parallel}$, whose divergence is

$$\nabla \cdot \tilde{\boldsymbol{J}}_{\parallel} = -\frac{1}{\eta} \left[\left(\tilde{\boldsymbol{b}} \cdot \nabla_{\perp} \right) \nabla_{\parallel}^{(0)} \bar{\varphi} + \nabla_{\parallel}^{(0)} \left(\tilde{\boldsymbol{b}} \cdot \nabla_{\perp} \right) \bar{\varphi} \right]. \tag{2.40}$$

Since the quasi-neutrality requires $\nabla \cdot \boldsymbol{J} = 0$ at all scales, equation (2.40) is supposed to be equal to 0 if $\tilde{\boldsymbol{J}}_{\parallel}$ is the only contribution to the microscopic current. To verify this point, we take the Fourier expansion of $\tilde{\boldsymbol{b}}$ and $\bar{\varphi}$, yielding

$$\begin{aligned}
&\bar{\varphi} = \bar{\varphi}_{\boldsymbol{k}}(\zeta) \exp\left[\gamma_{\boldsymbol{k}} t + i k_y \chi\right], \\
&\tilde{\boldsymbol{b}} = \sum_{\boldsymbol{k_1}} \tilde{\boldsymbol{b}}_{\boldsymbol{k_1}}(x) \exp\left[i\left(k_{1y} y - k_{1z} z\right)\right] = \sum_{\boldsymbol{k_1}} \tilde{\boldsymbol{b}}_{\boldsymbol{k_1}}\left(\hat{\xi}_{\boldsymbol{k_1}}\right) \exp\left[\left(i k_{1y} \chi + i k_{1\parallel} \zeta\right)\right],
\end{aligned} \tag{2.41}$$

where $k_{1\parallel} = s k_{1y} \hat{\xi}_{\boldsymbol{k}_1}$, $\hat{\xi}_{\boldsymbol{k}_1} = \xi - \xi_{\boldsymbol{k}_1}$, $\xi_{\boldsymbol{k}_1} = k_{1z}/k_{1y}$. The twisted coordinate system (equation (2.9)) is employed here. As mentioned in section 2.2.2, the quasi-mode is assumed to be independent of ξ. Then by plugging equation (2.41) into equation (2.40), we have

$$\begin{aligned}
&\left(\tilde{\boldsymbol{b}} \cdot \nabla_{\perp}\right) \nabla_{\parallel}^{(0)} \bar{\varphi} + \nabla_{\parallel}^{(0)} \left(\tilde{\boldsymbol{b}} \cdot \nabla_{\perp}\right) \bar{\varphi} \\
=&\sum_{\boldsymbol{k}_1} \Bigg\{ 2 i k_y \left[-s\zeta \tilde{b}_{x_{\boldsymbol{k}_1}}\left(\hat{\xi}_{\boldsymbol{k}_1}\right) + \tilde{b}_{y_{\boldsymbol{k}_1}}\left(\hat{\xi}_{\boldsymbol{k}_1}\right)\right] \frac{\partial \bar{\varphi}_{\boldsymbol{k}}(\zeta)}{\partial \zeta} \\
&- s k_y k_{1y} \hat{\xi}_{\boldsymbol{k}_1} \left[-s\zeta \tilde{b}_{x_{\boldsymbol{k_1}}}\left(\hat{\xi}_{\boldsymbol{k}_1}\right) + \tilde{b}_{y_{\boldsymbol{k}_1}}\left(\hat{\xi}_{\boldsymbol{k}_1}\right)\right] \bar{\varphi}_{\boldsymbol{k}}(\zeta) + i k_y \left[-s \tilde{b}_{x_{\boldsymbol{k}_1}}\left(\hat{\xi}_{\boldsymbol{k}_1}\right)\right] \bar{v}_{x\boldsymbol{k}}(\zeta) \Bigg\} \times \\
&\exp\left[\gamma_{\boldsymbol{k}} t + i\left(k_{1y} + k_y\right)\chi + i k_{1\parallel} \zeta\right].
\end{aligned} \tag{2.42}$$

To simplify equation (2.42), we consider the "ground state" of the quasi-mode given in equation (2.14) ($j = 0$), and assume the stochastic magnetic potential $\tilde{A}$ has a Gaussian profile across the resonant surface, i.e.

$$\begin{aligned}
\bar{\varphi}_{\boldsymbol{k}}(\zeta) &= \bar{\varphi}_0 \exp\left(-\zeta^2/2\Delta^2\right), \\
\tilde{A}_{\boldsymbol{k_1}}\left(\hat{\xi}_{\boldsymbol{k}_1}\right) &= \tilde{A}_{0\boldsymbol{k}_1} \exp\left(-\hat{\xi}_{\boldsymbol{k_1}}^2/2o_{\boldsymbol{k_1}}^2\right),
\end{aligned} \tag{2.43}$$

where $o_{\boldsymbol{k}_1}$ is the island width. By integrating equation (2.43) into equation (2.42), we observe that for $\nabla\cdot\tilde{\boldsymbol{J}}=0$ to hold, the following equations

$$\left(2\frac{\zeta^2}{\Delta^2}-1\right)+\frac{\xi_{\boldsymbol{k}_1}^2}{o_{\boldsymbol{k}_1}^2}=0,\quad \frac{2}{\Delta^2 o_{\boldsymbol{k}_1}^2}-s^2k_{1y}^2=0 \tag{2.44}$$

must be satisfied for arbitrary $\boldsymbol{k}_1$, which is clearly impossible. This brings us back to the narrative we developed in our previous study on resistive interchange modes in a stochastic magnetic field [79], i.e., small-scale convective cells must be driven by the beat of stochastic magnetic field with quasi-mode, which further generate a current density fluctuation $\tilde{\boldsymbol{J}}_\perp$ so as to keep $\nabla\cdot(\tilde{\boldsymbol{J}}_\parallel+\tilde{\boldsymbol{J}}_\perp)=0$. Figure 2.5 provides a heuristic illustration of the physical mechanism underpinning the formation of small-scale convective cells. According to the continuity equation of charge, $\nabla\cdot\tilde{\boldsymbol{J}}_\parallel\neq 0$ implies the accumulation of the polarization charge. Consider the term $\nabla_\parallel^{(0)}\left(\tilde{b}_y\partial_y\bar{\varphi}\right)$ on the R.H.S of equation (2.40) as an example, which actually serves as the main drive of the small-scale convective cells. With the profiles provided in equation (2.43), it turns out that this term leads to a polarization charge fluctuation, whose profile across the resonant surface is proportional to $\xi_{\boldsymbol{k}_1}^2/o_{\boldsymbol{k}_1}^2\exp(-\xi_{\boldsymbol{k}_1}^2/2o_{\boldsymbol{k}_1}^2)$. This accumulation of polarization charge is responsible for the emergence of the electrostatic potential fluctuation $\tilde{\varphi}$ and the resulting convective cells $\tilde{v}_{x_{\boldsymbol{k}_1}}$, as sketched by the purple dotted line in figure 2.5. Since the generation of small-scale convective cells is an outcome of the introduction of $\tilde{\boldsymbol{b}}$, it's to be expected that there exists a non-trivial correlation $\langle\tilde{\boldsymbol{b}}\tilde{v}_x\rangle$. This correlation is further calculated in section 2.3.3.

2.3.2 Formulation of a multi-scale system

As depicted in figure 2.6, a large-scale quasi-mode, a background stochastic magnetic field, and the microturbulence are the three main "players" in our model. Hence, the vorticity equation and the continuity equation are modified to

$$\left(\frac{\partial}{\partial t}-\nu_T\nabla_\perp^2\right)\nabla_\perp^2(\bar{\varphi}+\tilde{\varphi})+\frac{S}{\tau_A}\left(\frac{\partial}{\partial\zeta}+\tilde{\boldsymbol{b}}\cdot\nabla_\perp\right)^2(\bar{\varphi}+\tilde{\varphi})-\frac{gB_0}{\rho_0}\frac{\partial(\bar{\rho}+\tilde{\rho})}{\partial y}=0, \tag{2.45}$$

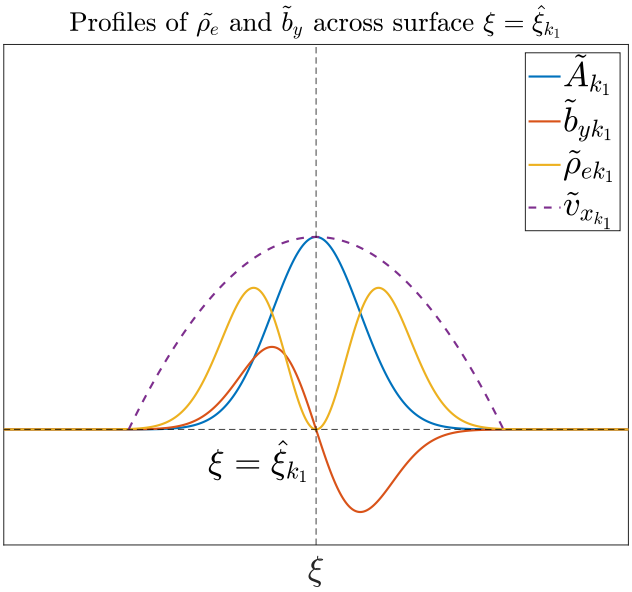

Figure 2.5. The profiles of $\tilde{A}_{\boldsymbol{k}_1}$, $\tilde{b}_{y_{\boldsymbol{k}_1}}$, $\tilde{\rho}_{e_{\boldsymbol{k}_1}}$ and $\tilde{v}_{x_{\boldsymbol{k}_1}}$ across the resonant surface $\xi = \xi_{\boldsymbol{k}_1}$. The stochastic magnetic field gives rise to the polarization charge fluctuation, which further induces a velocity fluctuation. Obviously, there is a non-zero correlation between $\tilde{A}$ and $\tilde{v}_x$.

and

$$\left(\frac{\partial}{\partial t} - D_T \nabla_\perp^2\right)(\bar{\rho} + \tilde{\rho}) = -(\bar{v}_x + \tilde{v}_x)\,\alpha\rho_0. \tag{2.46}$$

Here $\bar{\rho}$, $\bar{\varphi}$, and $\bar{\boldsymbol{v}}$ are the plasma mass density, electrostatic potential, and resultant $E \times B$ drift velocity fluctuations of the quasi-mode, $\tilde{\rho}$, $\tilde{\varphi}$ and $\tilde{\boldsymbol{v}}$ are the density, electrostatic potential and resultant $E \times B$ drift velocity fluctuations of the microturbulence. The expressions for the operators in equation (2.45) and (2.46) are given by equation (2.83) in 2.B. With the emergence of the small-scale convective cells, the time derivative ∂_t in equation (2.5) and (2.31) should be modified to $\partial_t + \tilde{\boldsymbol{v}} \cdot \nabla$ to account for the random advection of the quasi-mode by small-scale convective cells. This random advection $\tilde{\boldsymbol{v}} \cdot \nabla$ can be renormalized as a diffusion operator $-\nu_T \nabla_\perp^2$ or $-D_T \nabla_\perp^2$ [64]. The turbulent viscosity ν_T and the turbulent diffusivity D_T thus enter our model. In this work, the Schmidt number Sc is set to 1, i.e., $\nu_T = D_T$, as their physical mechanisms are the same.

In both section 2.2 and the prior work, the slow interchange approximation is utilized for

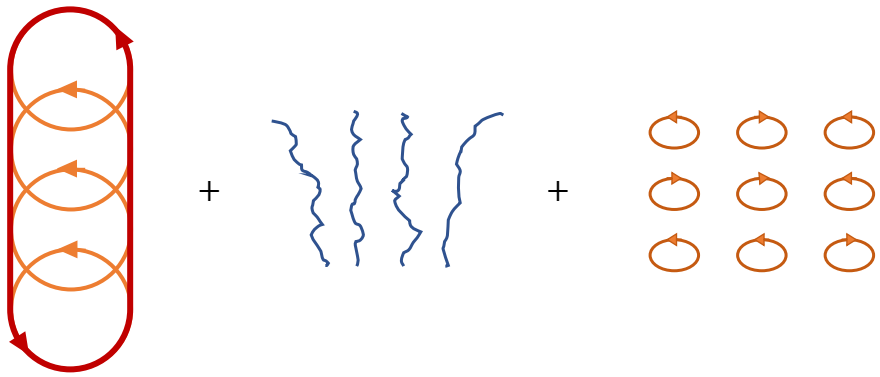

Figure 2.6. A sketch of the multi-scale model in this work: a large-scale quasi-mode (red envelope curves), a small-scale background stochastic magnetic field (blue curves), and small-scale convective cells (orange cells).

the large-scale resistive interchange mode and the quasi-mode. So for consistency and simplicity, the same setup is adopted in our model, namely $k_y \ll 1/\delta_{\boldsymbol{k}}$, where $\delta_{\boldsymbol{k}}$ is the width of the localized interchange mode defined in equation (2.21). Owing to the small spatial scales of $\tilde{\boldsymbol{b}}$ and the fact that $\tilde{\boldsymbol{v}}$ emerges as a response to $\tilde{\boldsymbol{b}}$, $\tilde{\boldsymbol{v}}$ also exhibits small spatial scales. More specifically, as the wavenumbers of $\tilde{\boldsymbol{b}}$ and $\tilde{\boldsymbol{v}}$ in the y direction are very large, it is reasonable to posit that those small-scale convective cells are fast interchange. It means $k_{1y} \gg 1/\delta_{\boldsymbol{k}_1}$, where $\delta_{\boldsymbol{k}_1}$ is the characteristic width of $\tilde{\boldsymbol{v}}_{k_1}$. In addition, based on the definition, $1/\Delta \cong sk_y\delta_{\boldsymbol{k}} \ll sk_{1y}\delta_{\boldsymbol{k}_1} \cong k_{1\parallel}$. And by requiring the magnitudes of $\tilde{b}_x$ and $\tilde{b}_y$ are of the same order, it follows that $k_{1y} \cong o_{\boldsymbol{k}_1}$. According to the above discussion, the spatial ordering of our system is

$$\begin{aligned}
&\underbrace{\left|\frac{1}{\bar{\varphi}}\frac{\partial\bar{\varphi}}{\partial\xi}\right|}_{=0} \ll \left|\frac{1}{\bar{\varphi}}\frac{\partial\bar{\varphi}}{\partial\zeta}\right| \ll \left|\frac{1}{\bar{\varphi}}\frac{\partial\bar{\varphi}}{\partial\chi}\right| \ll \left|\frac{1}{\tilde{\varphi}}\frac{\partial\tilde{\varphi}}{\partial x}\right| \ll \left|\frac{1}{\tilde{\varphi}}\frac{\partial\tilde{\varphi}}{\partial\chi}\right|, \\
&\left|\frac{1}{\bar{\varphi}}\frac{\partial}{\partial\zeta}\bar{\varphi}\right| \ll \left|\frac{1}{\tilde{\varphi}}\frac{\partial}{\partial\zeta}\tilde{\varphi}\right| \ll \left|\frac{1}{\tilde{\varphi}}\frac{\partial}{\partial\chi}\tilde{\varphi}\right|.
\end{aligned} \tag{2.47}$$

In our prior work, it was highlighted that the growth of small-scale convective cells, recognized as fast interchange, is over-saturated by ν_T and D_T. This implies that the fast interchange growth

rate $\gamma_{\boldsymbol{k}_1} = (\alpha g)^{1/2}$, is smaller than the turbulent damping rates $\nu_T k_{1y}^2$. In contrast, due to the small magnitude of the magnetic perturbation, we can treat its effect on the quasi-mode as a perturbation, and thus have $\nu_T k_y^2 \ll \gamma_{\boldsymbol{k}}$. Then the temporal ordering of our model is

$$\nu_T k_y^2 \ll \gamma_{\boldsymbol{k}} \ll \gamma_{\boldsymbol{k}_1} < \nu_T k_{1y}^2. \tag{2.48}$$

Inequalities (2.47) and (2.48) indicate a separation of the spatio-temporal scales in this model. For such as multi-scale system, we can employ the method of averaging to separate the dynamics of different scales. By adopting the spatial averaging defined as

$$\langle A \rangle = \bar{A} = \frac{1}{L_y} \int_{-L_y/2}^{L_y/2} e^{-ik_y \chi} A d\chi, \tag{2.49}$$

where χ is the coordinate defined in equation (2.9), the full set of equations for this model is given as follows:

$$\left(\frac{\partial}{\partial t} - \nu_T \nabla_\perp^2\right) \nabla_\perp^2 \bar{\varphi} + \frac{S}{\tau_A} \frac{\partial^2}{\partial \zeta^2} \bar{\varphi}$$
$$+ \frac{B_0^2}{\eta} \left\{ \underbrace{\left\langle \left(\tilde{\boldsymbol{b}} \cdot \nabla_\perp\right)^2 \right\rangle \bar{\varphi}}_{(a)} + \underbrace{\left\langle \frac{\partial}{\partial \zeta} \left(\tilde{\boldsymbol{b}} \cdot \nabla_\perp\right) \tilde{\varphi} \right\rangle}_{(b)} + \underbrace{\left\langle \left(\tilde{\boldsymbol{b}} \cdot \nabla_\perp\right) \frac{\partial}{\partial \zeta} \tilde{\varphi} \right\rangle}_{(c)} \right\} - \frac{g B_0}{\rho_0} \frac{\partial}{\partial y} \bar{\rho} = 0, \tag{2.50a}$$
$$\left(\frac{\partial}{\partial t} - \nu_T \nabla_\perp^2\right) \nabla_\perp^2 \tilde{\varphi} + \frac{S}{\tau_A} \frac{\partial^2}{\partial \zeta^2} \tilde{\varphi}$$
$$+ \frac{S}{\tau_A} \left\{ \frac{\partial}{\partial \zeta} \left(\tilde{\boldsymbol{b}} \cdot \nabla_\perp\right) \bar{\varphi} + \left(\tilde{\boldsymbol{b}} \cdot \nabla_\perp\right) \frac{\partial}{\partial \zeta} \bar{\varphi} \right\} - \frac{g B_0}{\rho_0} \frac{\partial}{\partial y} \tilde{\rho} = 0, \tag{2.50b}$$
$$\left(\frac{\partial}{\partial t} - D_T \nabla_\perp^2\right) \bar{\rho} = -\bar{v}_x \alpha \rho_0, \tag{2.50c}$$
$$\left(\frac{\partial}{\partial t} - D_T \nabla_\perp^2\right) \tilde{\rho} = -\tilde{v}_x \alpha \rho_0. \tag{2.50d}$$

As can be seen from these equations, dynamics of the large-scale quasi-mode and the small-scale convective cells are coupled to each other. On the one hand, terms involving the beat of $\tilde{\boldsymbol{b}}$ and

$\bar{\varphi}$ act as the source of equation (2.50b), driving the microturbulence $\tilde{\varphi}$. On the other hand, in equation (2.50a), terms involving $\tilde{\varphi}$ can react on the evolution of the quasi-mode $\bar{\varphi}$.

The workflow of the remaining calculations in this paper can be summarized by figure 2.7. After using the method of averaging to separate the dynamics at different scales, the next step is to get the linear response of $\tilde{v}_x$ to the beat of $\tilde{\boldsymbol{b}}$ with $\bar{v}_x$ by solving the small-scale dynamics. The correlation between $\tilde{v}_x$ and $\tilde{\boldsymbol{b}}$ is calculated by exploiting this linear response. Then, upon plugging the linear response into equation (2.50a), the revised eigenmode equation for the quasi-mode, which includes all the effects of the stochastic magnetic field, is obtained. Subsequently, the corrected growth rate of the quasi-mode is computed via perturbation theory. Finally, a simple nonlinear closure model is used to compute the scaling of the turbulent viscosity and the turbulent diffusivity arising from the microturbulence.

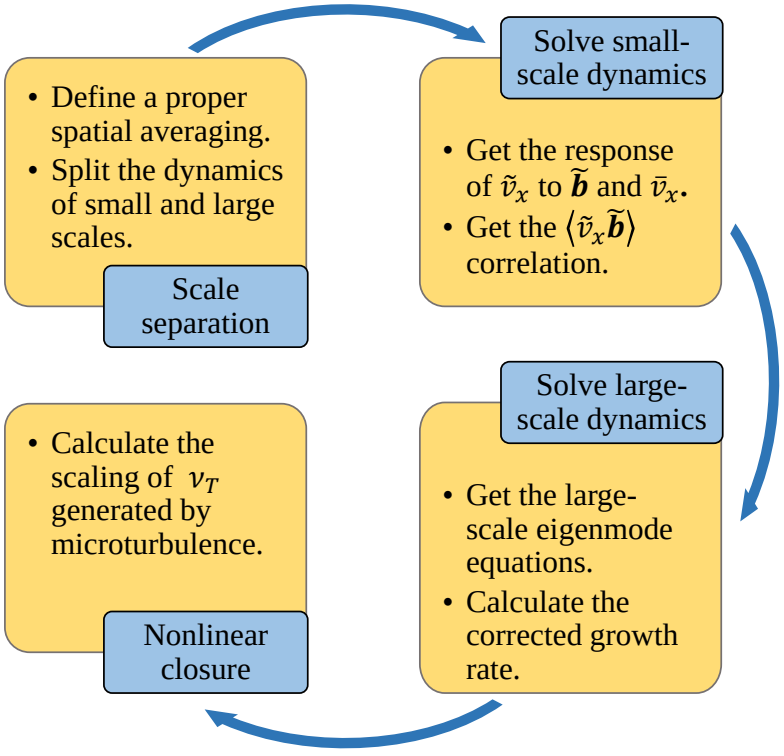

Figure 2.7. The workflow of the remaining calculation.

2.3.3 Correlation between $\tilde{v}_x$ and $\tilde{\boldsymbol{b}}$

To determine the effect of the stochastic magnetic field on the growth rate of the quasi-mode, the unknown quantity, $\tilde{\varphi}$, must be eliminated from equation (2.50a). This requires us to find the response of $\tilde{\varphi}$ to $\tilde{\boldsymbol{b}}$, which can be obtained from equation (2.50b). Similar to the Fourier series of $\tilde{\boldsymbol{b}}$ given in equation (2.41), the Fourier series of $\tilde{\varphi}$ and $\tilde{\rho}$ are

$$\begin{aligned}\tilde{\varphi} &= \sum_{\boldsymbol{k}_1} \tilde{\varphi}_{\boldsymbol{k}_1}\left(\hat{\tilde{\xi}}_{\boldsymbol{k}_1}, \zeta\right) \exp\left[\gamma_{\boldsymbol{k}} t + ik_{1y}\chi + ik_{1\parallel}\zeta\right], \\ \tilde{\rho} &= \sum_{\boldsymbol{k}_1} \tilde{\rho}_{\boldsymbol{k}_1}\left(\hat{\tilde{\xi}}_{\boldsymbol{k}_1}, \zeta\right) \exp\left[\gamma_{\boldsymbol{k}} t + ik_{1y}\chi + ik_{1\parallel}\zeta\right],\end{aligned} \tag{2.51}$$

where $\tilde{\varphi}_{\boldsymbol{k}_1}$ and $\tilde{\rho}_{\boldsymbol{k}_1}$ are slowly varying functions of ζ. Note that the growth rates of $\tilde{\varphi}$ and $\tilde{\rho}$ are the slow interchange growth rate $\gamma_{\boldsymbol{k}}$, rather than the fast interchange growth rate $\gamma_{\boldsymbol{k}_1}$. This is because the growth of $\tilde{\varphi}$ and $\tilde{\rho}$ is over-saturated by the turbulent viscosity ν_T and the turbulent diffusivity D_T, and adiabatically modulated by the growth of the quasi-mode. As a result, both sides of equation (2.50b) grow at the same rate.

Since the quasi-mode is not periodic in the main field direction, it is challenging to define an appropriate averaging over ζ. Therefore, the spatial averaging employed in this work, as defined by equation (2.49), differs from the one used for the resistive interchange mode. In our previous work, the averaging was carried out in both toroidal and poloidal directions. While this averaging scheme is able to separate the dynamics of large and small scales, it only provides the relation between a spectrum of $\tilde{\varphi}_{\boldsymbol{k}_1}$ with the same k_{1y} and a spectrum of $\tilde{\boldsymbol{b}}_{k_2}$ with the same k_{2y}, rather than the response of a single $\tilde{\varphi}_{\boldsymbol{k}_1}$ to a single $\tilde{\boldsymbol{b}}_{k_2}$. To address this issue, we suppose that only magnetic perturbations $\tilde{\boldsymbol{b}}_{k_2}$ that are located at the same resonance surface as $\tilde{\varphi}_{\boldsymbol{k}_1}$ can drive $\tilde{\varphi}_{\boldsymbol{k}_1}$. In other words, only the *coherent response* of $\tilde{\varphi}_{\boldsymbol{k}1}$ to $\tilde{\boldsymbol{b}}_{k2}$ is considered. Since both of $\tilde{\varphi}_{\boldsymbol{k}_1}$ and $\tilde{\boldsymbol{b}}_{k_2}$ are highly localized near the resonant surfaces, this is a fair assumption. Substituting equation (2.50d) and (2.51) into equation (2.50b), and simplifying it according to the scale orderings given

by inequalities (2.47) and (2.48), we get

$$-2\nu_T k_{1y}^2 \frac{\partial^2}{\partial \xi^2}\tilde{v}_{x\boldsymbol{k_1}} + \frac{S}{\tau_A} s^2 k_{1y}^2 \hat{\xi}_{\boldsymbol{k_1}}^2 \tilde{v}_{x\boldsymbol{k_1}} - \left(\frac{\alpha g}{D_T} - \nu_T k_{1y}^4\right)\tilde{v}_{x\boldsymbol{k_1}}$$
$$= \frac{S}{\tau_A} i k_{1y}\left[-s\tilde{b}_{\boldsymbol{k_2}}\left(2\zeta\partial_\zeta + 1\right) + 2\tilde{b}_{y_{\boldsymbol{k_2}}}\partial_\zeta\right]\bar{v}_{x\boldsymbol{k}} - \frac{S}{\tau_A} k_{1y} k_{2\parallel}\left[-s\zeta\tilde{b}_{x_{\boldsymbol{k_2}}} + \tilde{b}_{y_{\boldsymbol{k_2}}}\right]\bar{v}_{x\boldsymbol{k}}, \quad (2.52)$$

where $\tilde{v}_{x\boldsymbol{k}_1} = -ik_{1y}\tilde{\varphi}_{\boldsymbol{k}_1}/B_0$, $\bar{v}_{x\boldsymbol{k}} = -ik_y\bar{\varphi}_{\boldsymbol{k}}/B_0$, and $\boldsymbol{k}_1$ and $\boldsymbol{k}_2$ satisfy relations

$$k_{1y} = k_{2y} + k_y, \quad \frac{k_{2z}}{sk_{2y}} = \frac{k_{1z}}{sk_{1y}}. \quad (2.53)$$

The extra Fourier factor $\exp(-isk_y\zeta\hat{\xi}_{\boldsymbol{k}_1})$ on the R.H.S is set to unity as the scale $sk_y\zeta \sim sk_y\Delta \sim 1/\delta_{\boldsymbol{k}}$ is irrelevant to the small-scale dynamics. It is more straightforward to see the significance of the drive by the beat of $\tilde{\boldsymbol{b}}$ and $\bar{v}_x$ from equation (2.52). If we retain the temporal variation of $\tilde{v}_{x\boldsymbol{k}_1}$, divide it by k_{1y}^2, and exploit the spatial-temporal ordering given by inequalities (2.47) and (2.48), equation (2.52) can be rewritten into the following heuristic form

$$\frac{\partial}{\partial t}\tilde{v}_{x\boldsymbol{k}_1} + \lambda\tilde{v}_{x\boldsymbol{k_1}} = \hat{D}\left[\tilde{\boldsymbol{b}}\bar{v}_x\right], \quad (2.54)$$

where

$$\lambda = \nu_T k_{1y}^2 - \frac{\alpha g}{D_T k_{1y}^2} \approx \nu_T k_{1y}^2 - (\alpha g)^{1/2}, \quad (2.55)$$

$\hat{D}$ denotes the drive by $\tilde{\boldsymbol{b}}\bar{v}_x$ beats on the R.H.S of equation (2.52). The first term in the expression for λ represents the turbulent damping, and the second term is the linear drive by the mean density gradient. As small-scale convective cells grow fast under the drive of mean density gradient, the nonlinear effect, i.e., the renormalized turbulent viscosity, will also increase so that at a point ν_T becomes large enough to over-saturate the linear drive, i.e., $\lambda > 0$. The processes of the linear growth and the over-saturation of $\tilde{v}_{x\boldsymbol{k}}$ both happen on a very short time scale $\sim \mathcal{O}(1/\gamma_{\boldsymbol{k}_1})$. On the longer time scale $\sim \mathcal{O}(1/\gamma_{\boldsymbol{k}})$, as the quasi-mode $\bar{v}_{x\boldsymbol{k}}$ varies with time, the drive $\hat{D}$ on the R.H.S of equation (2.54) will modulate the microturbulence $\tilde{v}_{x\boldsymbol{k}_1}$ adiabatically. One may

notice that equation (2.54) is similar in structure to a Langevin equation, which further suggests a fluctuation-dissipation balance. The stochastic magnetic field $\tilde{\boldsymbol{b}}$ thus has dual identities: on the one hand, it serves as the drive (recall the random kicks in Brownian motion) to excite the microturbulence; on the other hand, the turbulence viscosity arising from $\tilde{\boldsymbol{b}}$ damps the growth of the small-scale convective cell, akin to the drag term in the Langevin equation.

Observing that the L.H.S of equation (2.52) is homogeneous in $\tilde{\varphi}_{\boldsymbol{k}_1}$ and resembles the equation for the quantum harmonic oscillator, the corresponding Green's function of equation (2.52) is [107]

$$G\left(\hat{\xi}_{\boldsymbol{k}_1}, \hat{\xi}'_{\boldsymbol{k}_1}\right) = \sum_l \frac{\psi^l_{\boldsymbol{k}_1}\left(\hat{\xi}_{\boldsymbol{k}_1}\right)\psi^l_{\boldsymbol{k}_1}\left(\hat{\xi}'_{\boldsymbol{k}_1}\right)}{\Lambda^l_{\boldsymbol{k}_1} - \Lambda_{\boldsymbol{k}_1}}, \tag{2.56}$$

where

$$\begin{aligned}
&\psi^l_{\boldsymbol{k}_1}(\hat{\xi}_{\boldsymbol{k}_1}) = \frac{H_l\left(\frac{\hat{\xi}_{\boldsymbol{k}_1}}{w'}\right)}{\pi^{\frac{1}{4}} w'^{\frac{1}{2}}\sqrt{2^l l!}} \exp\left[-\frac{1}{2}\left(\frac{\hat{\xi}_{\boldsymbol{k}_1}}{w'}\right)^2\right], \\
&\Lambda^l_{\boldsymbol{k}_1} = \frac{4\rho_0 \nu_T k_{1y}^2}{w'^2}\left(l+\frac{1}{2}\right) \ll \Lambda_{\boldsymbol{k}_1} = -\rho_0 \nu_T k_{1y}^4, \quad w' = w_{\boldsymbol{k}_1} = \left(\frac{2\tau_A \nu_T}{Ss^2}\right)^{\frac{1}{4}}.
\end{aligned} \tag{2.57}$$

Note that $w_{\boldsymbol{k}_1}/\delta_{\boldsymbol{k}_1} = (2\nu_T k_{1y}^2/\gamma_{\boldsymbol{k}_1})^{1/4} > 1$, which indicates the turbulent viscosity can broaden the width of $\tilde{\varphi}_{\boldsymbol{k}_1}$. But as $w_{\boldsymbol{k}_1}/\delta_{\boldsymbol{k}} = (\nu_T k_y^2/\gamma_{\boldsymbol{k}})^{1/4} < 1$, the spatial ordering given by equation (2.47) remains valid. Utilizing this Green's function, we obtain the approximate solution of equation (2.52) given as follows

$$\begin{aligned}
&\tilde{v}_{x\boldsymbol{k}_1} \approx \tilde{v}^{(l=0)}_{x\boldsymbol{k}_1} + \tilde{v}^{(l=1)}_{x\boldsymbol{k}_1}, \\
&\tilde{v}^{(l=0)}_{x\boldsymbol{k}_1} \approx \frac{S}{\tau_A \nu_T k_{1y}^4}\frac{\sqrt{2}o_{\boldsymbol{k}_2}\tilde{A}_{0\boldsymbol{k}_2}}{w'}\left[-2sk_{1y}k_{2y}\zeta\,\partial_\zeta \bar{v}_{x\boldsymbol{k}}(\zeta)\right]\exp\left[-\frac{1}{2}\left(\frac{\hat{\xi}_{\boldsymbol{k}_1}}{w'}\right)^2\right], \\
&\tilde{v}^{(l=1)}_{x\boldsymbol{k}_1} \approx -\frac{S}{\tau_A \nu_T k_{1y}^4}\frac{\sqrt{2}o_{\boldsymbol{k}_2}\tilde{A}_{0\boldsymbol{k}_2}}{w'}\left[2ik_{1y}\partial_\zeta \bar{v}_{x\boldsymbol{k}}(\zeta) + is^2 k_{1y}k_{2y}^2 o^2_{\boldsymbol{k}_2}\zeta\,\bar{v}_{x\boldsymbol{k}}(\zeta)\right]\frac{2x}{w'}\exp\left[-\frac{1}{2}\left(\frac{\hat{\xi}_{\boldsymbol{k}_1}}{w'}\right)^2\right].
\end{aligned} \tag{2.58}$$

Without loss of physics and for simplicity, only the first two terms of the Green's function (i.e., $l = 0$ and $l = 1$ terms) are retained, representing the even and odd parity of the solution, respectively. With this solution, the correlation between $\tilde{v}_x$ and $\tilde{\boldsymbol{b}}$, which is a function of ζ, can be expressed as

$$\begin{aligned}
\langle \tilde{v}_x \tilde{b}_x \rangle &= \sum_{\boldsymbol{k}_1} \tilde{v}_{x(\boldsymbol{k}-\boldsymbol{k}_1)} \tilde{b}_{x\boldsymbol{k}_1} = \frac{iL_y L_z}{(2\pi)^2} \int dk_{1y} \frac{s^2 k_y S \left|\tilde{A}_{0\boldsymbol{k}_1}\right|^2}{\tau_A \nu_T \left|k_{1y}\right|} \frac{12\sqrt{\pi} o_{\boldsymbol{k}_1}^2}{w'} \zeta \partial_\zeta \bar{v}_{x\boldsymbol{k}}, \\
\langle \tilde{v}_x \tilde{b}_y \rangle &= \sum_{\boldsymbol{k}_1} \tilde{v}_{x(\boldsymbol{k}-\boldsymbol{k}_1)} \tilde{b}_{y\boldsymbol{k}_1} = -\frac{iL_y L_z}{(2\pi)^2} \int dk_{1y} \frac{s^3 k_y S \left|\tilde{A}_{0\boldsymbol{k}_1}\right|^2}{\tau_A \nu_T \left|k_{1y}\right|} \frac{12\sqrt{\pi} o_{\boldsymbol{k}_1}^4}{w'^3} \zeta \bar{v}_{x\boldsymbol{k}},
\end{aligned} \tag{2.59}$$

where the summation over $\boldsymbol{k}_1$ is transformed into an integral over k_{1y} and $\xi_{\boldsymbol{k}_1}$, i.e.

$$\sum_{\boldsymbol{k}_1} = \frac{L_z L_y}{(2\pi)^2} \int dk_{1y} s \left|k_{1y}\right| \int d\xi_{\boldsymbol{k}_1}. \tag{2.60}$$

This is a fair transformation as magnetic perturbations $\tilde{\boldsymbol{b}}_{k_1}$ at different resonant surfaces are densely packed.

The non-trivial correlation between $\tilde{v}_x$ and $\tilde{\boldsymbol{b}}$ given in equation (2.59) could serve as a cause for the reduction in the Jensen-Shannon complexity of the edge turbulence during the RMP ELM suppression phase. $\langle \tilde{v}_x \tilde{\boldsymbol{b}} \rangle \neq 0$ means that when RMP is applied, high-$\boldsymbol{k}$ fluctuations are generated and coupled to the stochastic magnetic field. In other words, the microturbulence "locks on" to the ambient stochasticity, and thus the statistical characteristics of the edge turbulence are changed by the externally prescribed magnetic perturbations. As mentioned in section 2.1, noisy signals have lower complexity. If we think of the magnetic perturbations as external noise, then the non-trivial correlation $\langle \tilde{v}_x \tilde{\boldsymbol{b}} \rangle$ makes statistics of edge turbulence more akin to those of noise, which is manifested as the reduction in its complexity in experiments. This can be interpreted as the suppression of the instability characteristic of a chaotic system by external noise [100]. Of course, we acknowledge that stochastic magnetic fields are not noise in the strict sense, but rather deterministic chaos. The effects of the stochastic magnetic field on the statistics of edge

turbulence indeed provides a possible explanation for the experimental phenomena. A deeper approach for further justification for our claim would be to study the changes in complexity when two chaotic systems are superposed. This will be discussed in more detail in section 2.4.3 as a direction for future study.

2.3.4 Correction to the quasi-mode growth rate and scaling of the turbulent viscosity

Using the spatial averaging defined by equation (2.49), the Fourier series of $\tilde{\boldsymbol{b}}$ and $\tilde{\varphi}$ given in equation (2.41) and (2.51), the response of $\tilde{v}_x$ to $\tilde{\boldsymbol{b}}$ given in equation (2.58), and replacing the summation over $\boldsymbol{k}_1$ by integral, the three correlations in equation (2.50a) are equal to

$$(a) = \left\langle \left(\tilde{\boldsymbol{b}} \cdot \nabla_\perp\right)^2 \right\rangle \bar{\varphi} = \left[-s^2\zeta^2 k_y^2 \left|\tilde{b}_x^2\right| + 2s\zeta k_y^2 \left|\tilde{b}_x \tilde{b}_y\right| - k_y^2 \left|\tilde{b}_y^2\right|\right] \bar{\varphi}_{xk}, \tag{2.61}$$

$$\begin{aligned}
&(b)+(c) = \left\langle \partial_\zeta \left(\tilde{\boldsymbol{b}} \cdot \nabla_\perp\right) \tilde{\varphi} + \left(\tilde{\boldsymbol{b}} \cdot \nabla_\perp\right) \partial_\zeta \tilde{\varphi} \right\rangle^{(l=0)} + \left\langle \partial_\zeta \left(\tilde{\boldsymbol{b}} \cdot \nabla_\perp\right) \tilde{\varphi} + \left(\tilde{\boldsymbol{b}} \cdot \nabla_\perp\right) \partial_\zeta \tilde{\varphi} \right\rangle^{(l=1)}, \\
&\left\langle \partial_\zeta \left(\tilde{\boldsymbol{b}} \cdot \nabla_\perp\right) \tilde{\varphi} + \left(\tilde{\boldsymbol{b}} \cdot \nabla_\perp\right) \partial_\zeta \tilde{\varphi} \right\rangle^{(l=0)} \\
&\approx -\frac{L_z L_y}{(2\pi)^2} \int dk_{1y} \left\{ \frac{S s^3 k_y^2 \left|\tilde{A}_{0\boldsymbol{k_1}}\right|^2}{\tau_A \nu_T \left|k_{1y}\right|} \frac{8\sqrt{\pi}\left|o_{\boldsymbol{k_1}}\right|^2}{w'} \right\} \zeta \partial_\zeta \bar{\varphi}_{\boldsymbol{k}}, \\
&\left\langle \partial_\zeta \left(\tilde{\boldsymbol{b}} \cdot \nabla_\perp\right) \tilde{\varphi} + \left(\tilde{\boldsymbol{b}} \cdot \nabla_\perp\right) \partial_\zeta \tilde{\varphi} \right\rangle^{(l=1)} \\
&\approx -\frac{L_z L_y}{(2\pi)^2} \int dk_{1y} \left\{ \frac{S s^3 k_y^2 \left|\tilde{A}_{0\boldsymbol{k_1}}\right|^2}{\tau_A \nu_T \left|k_{1y}\right|} \frac{8\sqrt{\pi}\left|o_{\boldsymbol{k_1}}\right|^4}{w'^3} \right\} \left(\bar{\varphi}_{\boldsymbol{k}} + \zeta \partial_\zeta \bar{\varphi}_{\boldsymbol{k}}\right).
\end{aligned} \tag{2.62}$$

Since

$$\frac{[(b)+(c)]^{(l=0)}}{[(b)+(c)]^{(l=1)}} \sim \frac{\left|o_{\boldsymbol{k_1}}\right|^2}{w'^2} \sim \frac{1}{k_{1y}^2 w'^2} \ll 1, \tag{2.63}$$

we can use the $l=0$ term to approximate the sum of correlation (b) and (c). After substituting equation (2.50c), (2.61) and (2.62) into equation (2.50a), the large-scale vorticity equation

becomes

$$\hat{H}_0 \bar{\varphi}_{\boldsymbol{k}} = \hat{H}_1 \bar{\varphi}_{\boldsymbol{k}}, \tag{2.64}$$

where

$$\hat{H}_0 = \frac{\partial^2}{\partial \zeta^2} - \frac{\gamma_{\boldsymbol{k}} \tau_A}{S} s^2 \zeta^2 k_y^2 + \frac{\gamma_{\boldsymbol{k}} \tau_A k_y^2}{S} \left(\frac{\alpha g}{\gamma_{\boldsymbol{k}}^2} - 1 \right), \tag{2.65}$$

$$\begin{aligned} \hat{H}_1 = & \left[s^2 \zeta^2 k_y^2 \left| \tilde{b}_x^2 \right| - 2 s \zeta k_y^2 \left| \tilde{b}_x \tilde{b}_y \right| + k_y^2 \left| \tilde{b}_y^2 \right| \right] \\ & + \frac{L_z L_y}{(2\pi)^2} \int dk_{1y} \frac{S s^3 k_y^2 \left| \tilde{A}_{0k_1} \right|^2}{\tau_A \nu_T \left| k_{1y} \right|} \frac{8\sqrt{\pi} \left| o_{\boldsymbol{k_1}} \right|^2}{w'} \zeta \partial_\zeta \\ & + \frac{\alpha g \tau_A D_T k_y^4 \left(1 + s^2 \zeta^2 \right)}{S \gamma_{\boldsymbol{k}}^2} + \frac{\tau_A}{S} \nu_T k_y^4 \left(1 + s^2 \zeta^2 \right)^2. \end{aligned} \tag{2.66}$$

Clearly the L.H.S of equation (2.65) is exactly the equation (2.13). By using perturbation theory, the first order growth rate correction $\gamma_{\boldsymbol{k}}^{(1)}$ is given by

$$\gamma_{\boldsymbol{k}}^{(1)} = \frac{\int_{-\infty}^{\infty} \bar{\varphi}_{\boldsymbol{k}}^{(0)}(\zeta) \hat{H}_1 \bar{\varphi}_{\boldsymbol{k}}^{(0)}(\zeta) d\zeta}{\int_{-\infty}^{\infty} \bar{\varphi}_{\boldsymbol{k}}^{(0)}(\zeta) \left[\partial_{\gamma_k^{(0)}} \hat{H}_0 \right] \bar{\varphi}_{\boldsymbol{k}}^{(0)}(\zeta) d\zeta}. \tag{2.67}$$

Plugging the expressions for $\hat{H}_0$, $\hat{H}_1$, and the 0th-order solution $\bar{\varphi}_{\boldsymbol{k}}^{(0)}$ into equation (2.67), the growth rate correction of the quasi-mode is

$$\gamma_{\boldsymbol{k}}^{(1)} = \underbrace{-\frac{5}{6} \nu_T s^2 \Delta^2 k_y^2 \left(1 + \frac{8}{5} \frac{1}{s^2 \Delta^2} \right)}_{①} - \frac{1}{3} \frac{S}{\tau_A} \Big[\underbrace{\left| \tilde{b}_x^2 \right|}_{②} - \underbrace{f \left| \tilde{b}_x^2 \right|}_{③} + \underbrace{\frac{2}{s^2 \Delta^2} \left| \tilde{b}_y^2 \right|}_{④} \Big], \tag{2.68}$$

where

$$f = \frac{\left\langle \left(\tilde{\boldsymbol{b}} \cdot \nabla_\perp \partial_\zeta + \partial_\zeta \tilde{\boldsymbol{b}} \cdot \nabla_\perp \right) \tilde{\varphi} \right\rangle}{\left\langle (\tilde{\boldsymbol{b}} \cdot \nabla)(\tilde{\boldsymbol{b}} \cdot \nabla) \bar{\varphi} \right\rangle} \sim 8 \underbrace{\frac{\nu_T k_y^2}{\gamma_{\boldsymbol{k}}^{(0)}}}_{f_1} \underbrace{\frac{\alpha g}{\nu_T^2 k_{1y}^4}}_{f_2} \underbrace{\frac{\left| o_{\boldsymbol{k_1}} \right|}{w'}}_{f_3}. \tag{2.69}$$

The sign of $\gamma_{\boldsymbol{k}}^{(1)}$ will be determined in section 2.4.1. Another useful output of our calculation is the scaling of the turbulent viscosity ν_T. As discussed in section 2.3.2, the turbulent viscosity ν_T and the turbulent diffusivity D_T originate from the microturbulence. Hence, the scaling of ν_T and D_T can be calculated through the following closure model [62, 63]

$$\nu_T = \sum_{\boldsymbol{k_1}} \left|\tilde{v}_{x\boldsymbol{k_1}}\right|^2 \tau_{\boldsymbol{k_1}}. \tag{2.70}$$

Here $\tau_{\boldsymbol{k}_1}$ is the turbulence correlation time, which can be estimated as $1/\gamma_{\boldsymbol{k}_1}$. Substituting equation (2.58) into equation (2.70) yields the following scaling of ν_T

$$\nu_T \cong \left[\frac{L_z L_y}{(2\pi)^2} \int dk_{1y} \frac{s^3 S^2 \left|\tilde{A}_{\boldsymbol{k_1}}\right|^2}{\tau_A^2 \left|k_{1y}\right|^3} \frac{4\sqrt{\pi}\left|o_{\boldsymbol{k_1}}\right|^2 \bar{v}_{x\boldsymbol{k}}(0)^2}{w'(\alpha g)^{1/2}} \left\{ \underbrace{2}_{\text{old}} + \underbrace{\left(\frac{k_{1y} o_{\boldsymbol{k}_2}^2}{k_y \delta_{\boldsymbol{k}} w'} \right)^2}_{\text{new}} \right\} \right]^{\frac{1}{3}}. \tag{2.71}$$

2.4 Discussion and conclusion

Given the fact that here a quasi-mode is a wave-packet consisting of localized resistive interchange modes, it's not surprising that this study would yield results somewhat similar to our prior research on the resistive interchange mode. *Nevertheless, due to the difference in the mode structure between the quasi-mode and the interchange mode, certain distinctions result.* In this section, we analyze the results obtained in section 2.3, with an emphasis on the *differences*. This paper concludes with a list of lessons that can deepen our comprehension of the effects of stochastic magnetic fields on the ballooning mode. In addition, suggested experiments and directions for future theoretical studies are provided.

2.4.1 Analysis of results

The term ① of the growth rate correction given by equation (2.68) is negative definite and proportional to ν_T. Except for an increment proportional to $1/(s\Delta)^2$, this term matches the

first term of the growth rate correction for the resistive interchange mode given in our prior work [79]. The physics behind this term can be interpreted as the damping by the turbulent viscosity. Specifically, since the small-scale convective cells drive a turbulent background, the resultant turbulent viscosity ν_T and turbulent diffusivity D_T can promote mixing, thereby damping the growth of the quasi-mode. It can be observed that inside the braces of the scaling of ν_T, there are two terms labeled as "old" and "new" respectively. If only the "old" term is retained, the scaling of ν_T reverts to that given by equation (38) in [79]. In this study, due to the changes in the mode structure and the spatial scaling ordering, both $\tilde{b}_x$ and $\tilde{b}_y$ enter the calculation of the scaling of ν_T. This leads to the emergence of the "new" term in equation (2.71), which is positive. *The resultant new ν_T is larger than that obtained in our previous research on the resistive interchange mode*.

While term ② and term ④ are negative definite, term ③ is positive. Since term ③ stems from the terms (b) and (c) in equation (2.50a), it implies that *the microturbulence has a destabilizing effect on the quasi-mode, in contrast to the case of the resistive interchange mode*. Again, this is due to the fact that the quasi-mode is much broader radially than the resistive interchange mode. Therefore, the sign of the sum of terms ②, ③, and ④ in equation (2.68) depends on the magnitude of parameter f, which is defined as the ratio of the sum of term (b) and term (c) to term (a) appearing in equation (2.50a). Equation (2.69) is an approximate expression for f, which is composed of three dimensionless factors, f_1, f_2, and f_3. The first factor f_1 is the ratio of the turbulent viscosity damping rate to the zeroth-order growth rate of the quasi-mode. As indicated in formula (2.48), due to the small magnitude of the magnetic perturbations, the effect of the stochastic magnetic field on the quasi-mode is considered as a small perturbation, which yields $\nu_T k_y^2 \ll \gamma_{\boldsymbol{k}}^{(0)}$ and thereby $f_1 \ll 1$. The second factor f_2 is equal to the square of the ratio of the 0th-order growth rate to the turbulent viscosity damping rate of the small-scale convective cells. As discussed in section (1.25), the growth of the small-scale convective cells is over-saturated by the turbulent viscosity and the turbulent diffusivity, which indicates $f_2 < 1$. As for the third factor f_3, given that we assume the magnitudes of $\tilde{b}_x$ and $\tilde{b}_y$ to be of the same

order, the island width $o_{\boldsymbol{k}_1}$ is comparable to $1/k_{1y}$. Consequently, f_3 can be approximated as $1/(k_{1y}w')$, which is much smaller than unity, as the fast interchange approximation applies to the small-scale convective cells. The constant 8 multiplying these three factors originates from two sources: the Gaussian integrals in the calculation of the linear response of $\tilde{v}_x$ to $\tilde{\boldsymbol{b}}$, and the fact that the number of terms involving both $\tilde{\boldsymbol{b}}$ and $\tilde{v}_x$ (terms (b) and (c)) is double that of the terms involving $\tilde{\boldsymbol{b}}$ alone (term (a)) in equation (2.50a) . Since $f_1 \ll 1$, $f_2 < 1$, and $8f_3 \leq 1$ (or at least $\sim \mathcal{O}(1)$), it follows that $f \ll 1$, indicating the sum of term ②, ③ and ④ is also negative definite. *Therefore, we can conclude that the net effect of the stochastic magnetic field on the quasi-mode is to slow its growth.*

The stabilization effect of term ② and term ④ becomes clearer if only the term (a) are retained in equation (2.50a). Then the eigenmode equation for the quasi-mode reduces to

$$\frac{\partial^2}{\partial \zeta^2}\bar{v}_{x\boldsymbol{k}} - \frac{\rho_{\text{eff}}\eta}{B_0^2}\gamma_{\boldsymbol{k}}k_y^2 s^2 \zeta^2 \bar{v}_{x\boldsymbol{k}} + \frac{\rho_0 \eta}{B_0^2}\frac{\alpha_{\text{eff}} g}{\gamma_{\boldsymbol{k}}}k_y^2 \bar{v}_{x\boldsymbol{k}} = 0, \tag{2.72}$$

where expressions for effective plasma inertia ρ_{eff} and effective drive α_{eff} are

$$\begin{aligned}
\rho_{\text{eff}} &= \rho_0 \left(1 + \frac{S}{\tau_A \gamma_{\boldsymbol{k}}} \left|\tilde{b}_x^2\right|\right) > \rho_0, \\
\alpha_{\text{eff}} &= \alpha \left(1 - \frac{S\gamma_{\boldsymbol{k}}}{\tau_A \gamma_{\boldsymbol{k}_1}^2} \left|\tilde{b}_y^2\right|\right) < \alpha.
\end{aligned} \tag{2.73}$$

The $|\tilde{b}_x \tilde{b}_y|$ cross term is omitted since it has no contribution to the growth rate correction. Here, ρ_{eff} and α_{eff} are defined as the effective mass density and the effective density gradient, respectively. According to equation (2.73), *it is evident that stochastic magnetic fields can stabilize the mode growth by enhancing the effective plasma inertia and reducing the effective drive.* Furthermore, by balancing the stochastic bending term to the linear bending term, the

critical island width for which this stabilization effect becomes significant is given as

$$o_{\boldsymbol{k}_1} \sim \delta_{\boldsymbol{k}} \left(\frac{k_y}{k_{1y}} \right)^{1/2}. \tag{2.74}$$

This result is a reminiscent of Rutherford's 1973 work on the nonlinear tearing mode [56]. In that paper, the growing perturbed magnetic field can generate a torque that drives the tearing mode against plasma inertia. But when the system enters the nonlinear regime, the nonlinear force induced by the perturbed magnetic field will produce another torque opposing the mode growth. The magnitudes of the torque produced by the linear and nonlinear forces become comparable when the island width is comparable to the width of the tearing layer, i.e., when $o_{\boldsymbol{k}_1} \sim \delta_{\boldsymbol{k}}$. As compared to Rutherford's model, equation (2.74) contains an additional factor of $(k_y/k_{1y})^{1/2}$, which is a footprint of the multi-scale nature of our model. The same criterion was also derived in our previous work.

2.4.2 Lessons learned for ballooning mode in a stochastic magnetic field

In this study, we constructed a comprehensive model for the dynamics of a low-$\boldsymbol{k}$ quasi-mode in a high-$\boldsymbol{k}$ stochastic magnetic field. For such an intrinsically multi-scale system, a standard procedure based on the quasi-linear theory is employed. By exploiting the resemblance between the quasi-mode and the ballooning mode, we can circumvent the difficulty posed by the differences in geometries between that used in theories of the ballooning mode and stochastic fields in a cylinder. Ultimately, we gain valuable physical insights into the dynamics of the ballooning mode in a stochastic magnetic field. These insights are consistent the existing simulations and experiments. The key takeaways from our study are:

1. To maintain quasi-neutrality ($\nabla \cdot \bar{\boldsymbol{J}} = 0$) at all scales, small-scale convective cells must be driven by the beat of the magnetic perturbations with the ballooning mode. In the simulation of the electrostatic resistive ballooning mode in a stochastic magnetic field by Beyer et al. [67], small-scale structures in the pressure fluctuation profile were observed.

The emergence of these small-scale structures can be explained by the microturbulence predicted by our theory. In addition, these small-scale convective cells could potentially allow for the possibility of enhanced nonlinear transfer by increasing the number of triad interactions. This picture provides another interpretation of the increase in the bicoherence of the pedestal temperature fluctuations in the stochastic layer, in addition to Waelbroeck et al.'s theory [108].

2. As indicated by equation (2.59), a non-trivial correlation develops between the velocity fluctuations $\tilde{v}_x$ and the magnetic perturbations $\tilde{\boldsymbol{b}}$. *Note that due to the change in the spatial ordering, a non-vanishing correlation* $\langle \tilde{b}_y \tilde{v}_x \rangle$ *appears in this work. Thus was absent in our previous work.* In other words, the microturbulence *"locks on"* to the externally prescribed stochastic magnetic field, and thus the edge plasma turbulence becomes more *"noisy"*. This theoretical prediction is consistent with the reduction of the Jensen-Shannon complexity of the temperature fluctuations during the RMP ELM suppression phase [68]. As previously discussed in section 2.1, the Jensen-Shannon complexity provides a metric for a system's predictability. Consequently, a decrease in the Jensen-Shannon complexity indicates an increase in the system's randomness. In other words, the chaotic behavior of the edge plasma turbulence is suppressed by an external noise, i.e., the stochastic magnetic field.

3. According to our discussion in section 2.4.1, it is reasonable to expect the stochastic magnetic field to impede the growth of the ballooning mode. This is also borne out by Beyer's simulation, in which a suppression of the large-scale fluctuations is observed [67]. More specifically, the stochastic magnetic field can slow the mode growth in three different ways: enhancing the effective plasma inertia (magnetic braking effect), reducing the effective drive, and boosting turbulent damping. *The second channel is newly discovered in this work.* The multi-scale nature of the system lowers the threshold for the magnitude of magnetic perturbations at which the magnetic braking effect becomes prominent, as

compared with Rutherford's criterion [56].

4. In equation (2.3), mode coupling (represented by the convective term $\boldsymbol{v}\cdot\nabla\boldsymbol{v}$) is omitted to first order accuracy. However, the appearance of the microturbulence restores the time derivative ∂_t to a nonlinear operator $\partial_t+\tilde{\boldsymbol{v}}\cdot\nabla$, which is further renormalized as $\partial_t-\nu_T\nabla_\perp^2$. In other words, *the microturbulence drives a turbulent background in which plasma instabilities—including the ballooning mode—reside.* This conclusion remains unchanged from our previous research. Yet, the broad radial structure of the ballooning mode alters the influence of the microturbulence on the mode itself. Firstly, the magnitude of the turbulent viscosity ν_T and the turbulent diffusivity D_T is *larger* than what we obtained in our study on the radially-localized resistive interchange mode. Secondly, the electrostatic scattering caused by the microturbulence tends to destabilize the ballooning mode, which is *opposite to* our conclusion for the resistive interchange mode. This destabilizing effect has been proved to be much weaker than the magnetic braking effect.

2.4.3 Suggested experiments and future plan

While this paper focuses primarily on the quasi-mode, our findings are broadly applicable to other models, such as drift waves and ITG, as $\nabla\cdot\boldsymbol{J}=0$ is a universal constraint for all types of modes. Thus, regardless of what the dominant mode at the edge is, when RMP is switched on, the microturbulence is inevitably driven, and the correlation between the microturbulence and the magnetic perturbations will be encountered. This further reinforces the validity of using our theory to explain the reduction in the complexity. However, as Jensen-Shannon complexity is a somewhat abstract concept, it is necessary to relate it to dynamical quantities, for practical purposes. Therefore, to validate our theory and enhance our understanding of plasma dynamics in a stochastic magnetic field, the following RMP experiments are suggested:

1. Beam emission spectroscopy (BES) velocimetry is a high-resolution plasma diagnostic for plasma velocity fluctuations [109]. By using the BES velocimetry, we are able to calculate

the of ratio of the turbulent heat flux to the total heat flux across the separatrix as a function of the strength of the magnetic perturbations (or, equivalently, the RMP coil current). The total heat flux could be obtained from the power budget. With the increase of the RMP coil current, the heat transport along the stochastic magnetic field would increase. At the same time, since we predict that the stochastic magnetic field can suppress the plasma instability, the turbulent heat flux would decrease. Hence, the decrease in the complexity of the edge turbulence should be accompanied by a reduction in the ratio of turbulent heat flux to the total heat flux.

2. Since Choi et al. used the electron cyclotron emission imaging (ECEI) as their pedestal turbulence diagnostic [110], their complexity analysis is based on electron temperature fluctuations. It might be enlightening to perform a similar analysis for the data of velocity fluctuations collected from BES velocimetry during both the RMP ELM suppression phase and the natural ELM-free phase. This is not only complementary to Choi's results, but also a straightforward verification of our theory. Considering both Choi's observations and the non-trivial correlation $\langle \tilde{v}_x \tilde{\boldsymbol{b}} \rangle$ in our theory, a decrease in the Jensen-Shannon complexity in the RMP ELM suppression phase is anticipated.

3. Direct examination of the presence of the correlation $\langle \tilde{v}_x \tilde{\boldsymbol{b}} \rangle$ also warrants further investigation. Using the velocity fluctuations gathered from BES and the magnetic fluctuation obtained from either simulations or experiments, we can calculate the correlation between $\tilde{v}_x$ and $\tilde{\boldsymbol{b}}$, and compare it to our theoretical prediction given by equation (2.59).

In addition to the experiments suggested above, two potential directions for future theoretical research have also been identified.

1. One may notice that zonal flow, a critical player in L-H transition, is missing from our model. In fact, it has been found that the stochastic magnetic field can indeed affect the zonal flow and the radial electric field [41, 111]. Many phenomena in RMP experiments,

such the increase in the L-H transition power threshold, can be attributed to the weakening of the shear flow. Hence, our next step will be to incorporate the zonal flow into our model. As is well known, zonal flow is driven by the Reynolds stress, which is represented as $\langle \tilde{v}_x \tilde{v}_y \rangle$. A non-vanishing Reynolds stress indicates a non-trivial correlation between k_x and k_y, i.e., $\langle k_x k_y \rangle \neq 0$. In the predator-prey model for zonal flow and drift wave turbulence [16], a non-trivial $\langle k_x k_y \rangle$ can develop from an initial weak velocity shear, i.e.,

$$\frac{dk_x}{dt} = -\langle v_E \rangle' k_y. \tag{2.75}$$

For years velocity shear has been recognized as the primary seed of zonal flow. However, k_x and k_y can also develop a non-trivial correlation from magnetic shear. With the presence of the magnetic shear, we have the equation

$$\frac{dk_x}{dz} = -sk_y, \tag{2.76}$$

which is similar in form to equation (2.75). This fact gives us some insights into future studies in this direction.

2. In section 1.25, the quasi-linear theory [112] is utilized to obtain the linear response of $\tilde{v}_x$ to $\tilde{\boldsymbol{b}}$. While doing so, we must be aware that the validity of the quasi-linear theory requires

$$Ku \approx \left(\frac{l_{ac}}{l_c} \right)^2 < 1. \tag{2.77}$$

Here Ku is a dimensionless number known as Kubo number. l_{ac} and l_c denote the auto-correlation length and decorrelation length of the stochastic magnetic field, respectively. However, the reality in tokamak is $Ku \sim 1$ [113]. Currently, almost all theories concerning stochastic magnetic fields are limited to the case where $Ku < 1$, while the $Ku > 1$ case is rarely studied. Therefore, another potential direction for future research is to investigate the

effects of the stochastic magnetic fields on plasma instabilities and turbulence in the $Ku \gg 1$ regime. Then, by decreasing Ku, we can approach the $Ku \sim 1$ regime asymptotically. In such cases, the quasi-linear theory is no longer available so we must look for new paradigms. Taylor and McNamara's work on 2D guiding center plasma and purely random array of discrete charged rods [114, 115] could be a good starting point. The behavior of their system is more like percolation process rather than diffusion process. Hence, it would be beneficial to seek inspiration from percolation theory [116, 117]. This work is expected to enhance our understanding of the actual situation by providing a perspective entirely different from the $ku < 1$ case.

3. As discussed in section 1.25, we use the non-trivial correlation $\langle \tilde{v}_x \tilde{\boldsymbol{b}} \rangle$ and the idea of the suppression of the instability characteristic of a chaotic system by external noise to explain the reduction in the complexity of the edge turbulence in the RMP ELM suppression phase. But we should recognize that the stochastic magnetic field is actually *not noise, but deterministic chaos*. Therefore, a deeper approach to justify our claim is to study how one chaotic system can affect the complexity of another. For simplicity, we can take 1D as a starting point. Suppose there are two different chaotic systems with different Lyapunov exponents, each producing a signal. We can then calculate the Jensen-Shannon complexity for each of these signals, as well as for their superposition. The point is to see whether the complexity of this superposed signal is reduced relative to the complexity of each individual signal, under certain conditions. This numerical experiment can be easily done and would serve as a further justification of our conclusion.

2.A Calculation of the Jensen-Shannon complexity

Given a series of data with N data points, we can use a sliding window of length d to capture the segments of the data. For instance, as shown in figure 2.8, when $d = 3$, consecutive segments such as (a_1, a_2, a_3), (a_2, a_3, a_4), (a_3, a_4, a_5) can be extracted. We can then map an

arbitrary segment $(s) \equiv (a_{s-2}, a_{s-1}, a_s)$ at time s to an "ordinary" pattern, which is a permutation $\pi = (b_1, b_2, b_3)$ of $(0,1,2)$ defined by $(a_{s-b_3} \leq a_{s-b_2} \leq a_{s-b_1})$. If $a_2 = 7$, $a_3 = 8$, $a_4 = 9$, $a_5 = 6$, then the corresponding "ordinary patterns" of (a_2, a_3, a_4) and (a_3, a_4, a_5) are $(0,1,2)$ and $(1,2,0)$, respectively. In the case of $d = 3$, there are $d! = 6$ possible permutations. By executing this mapping to all the segments, we can obtain a probability distribution $P = \{p(\pi)\}$ defined by

$$p(\pi) = \frac{\#\{s | d \leq s \leq N;\ \text{map}(s) = \pi\}}{N - d + 1}, \tag{2.78}$$

where # is the number of segments satisfying condition inside the braces. For the distribution function to be meaningful, N should be significantly larger than $d!$. Using this distribution function, the normalized Shannon entropy is equal to

$$H[P] = -\sum_{i=1}^{d!} p_i \ln(p_i)/S_{\max}, \tag{2.79}$$

where $S_{\max} = \ln(d!)$ is the entropy of the uniform distribution $P_e = \{p_i = 1/d!\}$. And the Jensen-Shannon divergence is calculated as

$$Q = Q_0\{S[(P + P_e)/2] - S[P]/2 - S[P_e]/2\}, \tag{2.80}$$

where Q_0 is a normalization constant. The Jensen-Shannon complexity C_{JS} is defined by equation (2.1), namely, the product of H and Q.

In Choi et al.'s work, C_{JS} is rescaled by the complexity of fractional Brownian noise or fractional Gaussian noise C_0 as

$$\hat{C} = \frac{C_{\text{JS}} - C_0}{\left| C_{\text{bdry}} - C_0 \right|}, \tag{2.81}$$

where C_{bdry} is the maximum (if $C_{\text{JS}} > C_0$) or minimum (if $C_{JS} < C_0$) Jensen-Shannon complexity at the given H. The rescaled $\hat{C}$ ranges from -1 to 1.

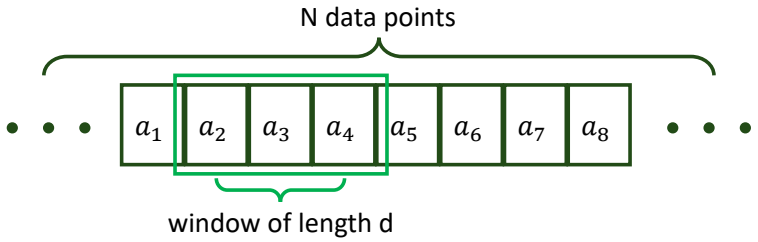

Figure 2.8. The sketch of the calculation of the Jensen-Shannon complexity for signal data.

2.B Expressions for the operators in this work

The derivatives in twisted slicing coordinate are

$$\begin{aligned}
\frac{\partial}{\partial x} &= \frac{\partial}{\partial \xi} - s\zeta \frac{\partial}{\partial \chi}, \\
\frac{\partial}{\partial y} &= \frac{\partial}{\partial \chi}, \\
\frac{\partial}{\partial z} &= \frac{\partial}{\partial \zeta} - s\xi \frac{\partial}{\partial \chi}.
\end{aligned} \tag{2.82}$$

The expressions for the operators used in this paper are

$$\begin{aligned}
\nabla^2 &= \frac{\partial^2}{\partial \xi^2} + \frac{\partial^2}{\partial \chi^2} + \frac{\partial^2}{\partial \zeta^2} + s^2\xi^2 \frac{\partial^2}{\partial \chi^2} + s^2\zeta^2 \frac{\partial^2}{\partial \chi^2} - 2s\xi \frac{\partial^2}{\partial \chi \partial \zeta} - 2s\zeta \frac{\partial^2}{\partial \xi \partial \chi}, \\
\nabla_\perp^2 &= \frac{\partial^2}{\partial \xi^2} + \frac{\partial^2}{\partial \chi^2} + s^2\zeta^2 \frac{\partial^2}{\partial \chi^2} - 2s\zeta \frac{\partial^2}{\partial \xi \partial \chi}, \\
\frac{\partial^2}{\partial y^2} + \frac{\partial^2}{\partial z^2} &= \frac{\partial^2}{\partial \chi^2} + \frac{\partial^2}{\partial \zeta^2} + s^2\xi^2 \frac{\partial^2}{\partial \chi^2} - 2s\xi \frac{\partial^2}{\partial \chi \partial \zeta}, \\
\boldsymbol{B}_0 \cdot \nabla &= \frac{\partial}{\partial z} + sx \frac{\partial}{\partial y} = \frac{\partial}{\partial \zeta}, \\
\tilde{\boldsymbol{b}} \cdot \nabla_\perp &= \tilde{b}_x \left(\frac{\partial}{\partial \xi} - s\zeta \frac{\partial}{\partial \chi} \right) + \tilde{b}_y \frac{\partial}{\partial \chi}.
\end{aligned} \tag{2.83}$$

Chapter 2, in full, is a reprint of the material as it appears in *Nuclear Fusion* 64(3):036003 (2024). Cao, Mingyun; Diamond, P.H., IOP Publishing, 2024. The dissertation author was the primary investigator and author of this paper.

Chapter 3

Physics of Edge-Core Coupling by Inward Turbulence Propagation

3.1 Introduction

Turbulence is often thought of as a multi-ingredient concoction—a "soup" that contains eddys, waves, structures, etc. Here "structures" may refer to vortices, density blobs, phase space holes, etc [118, 119, 120, 121, 122]. Structures are distinguished from ordinary eddys by extended lifetimes and a self-binding character that maintains them against stochastic shear stresses. The well-known and physically appealing Okubo-Weiss criterion gives one measure of the resilience of a vortex structure [123, 124]. In confined plasmas, the creation of structure has been traced to relaxation events, such as gradient turnovers near the plasma edge. These are observed to generate pairs of plasma filaments—blobs (density excesses) and voids (density depletions)—which propagate in opposite directions, down and up the mean gradient, respectively [33, 28]. Thus, edge gradient relaxation events pervade plasma boundary turbulence with structures. Here, we explore how inward-propagating voids energize edge turbulence beyond expected levels of intensity.

The dynamics of edge-core coupling is critically important to the optimization of magnetically confined fusion plasmas [125]. To this end, the physics of what sets the width of the edge-core coupling region, where the turbulence level exceeds the prediction of standard Fickian gyrokinetic models, remains an important "known unknown". This is sometimes referred to as

the "shortfall problem" [126, 127]. The edge-core coupling region is also named as "no man's land" (NML) because it falls between the domains of the conventional core and edge models and codes [122]. Since early proposals by B.B. Kadomtsev [128], there has been persistent speculation that inward propagation of turbulence from the boundary is a means to energize the NML [129]. However, no work has set forth a detailed calculation that explains how the tail (edge) wags the dog (core). No reasonable estimates of the inward turbulence intensity flux and the width of the NML have been proposed, either. Here, by developing a model incorporating coherent structures—more precisely, density voids—into turbulence dynamics, we demonstrate that the Cherenkov emission of drift waves from inward-moving voids generated at the edge drives substantial inward turbulence spreading. We show this is comparable to local turbulence production, and so drives a broad turbulent layer of width $\sim 100\ \rho_s$ for typical parameters (ρ_s is the ion sound speed gyroradius).

Recent beam emission spectroscopy (BES) studies observed that regular, intense gradient relaxation events (GREs) generated blob-void pairs very close to the last closed flux surface (LCFS) in tokamaks [32]. This occurred in low confinement mode. In particular, blobs propagate outward and detach from the bulk plasma, while voids propagate inward and so stir the NML. Recently, it has been found that the shortfall is resolved in flux-driven gyrokinetic simulations, where relaxation of mean gradients is allowed [130]. This suggests a correlation between GREs and the formation of NML. As a concrete entity produced from GREs and delivered from edge to core, a void is a promising mediator of the inward turbulence spreading.

The physical picture of our model can be illustrated by the cartoon in figure 3.1. After being generated from GREs at ψ_0, inward-moving voids (deep blue circles) will excite a "radiation field", which can be divided into a near field and a far field. In the near field, the void drives an interchange response, which converts to a drift wave turbulence (light blue shades) in the far field. While voids "evaporate" at ψ_1, void-induced turbulence can propagate deeper and energize the NML in the range from ψ_2 to ψ_1. This turbulence is regulated by self-generated zonal flow, originating due to radiation-driven Reynolds stress. Concomitantly, the (ambient) turbulence

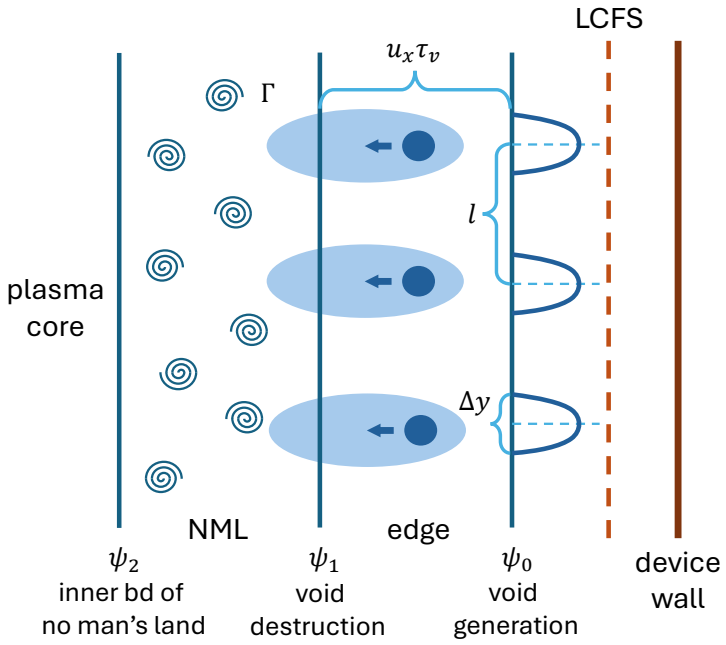

Figure 3.1. Illustration of the energization of the no man's land by inward-moving voids. The confined plasma core is to the left of the magnetic surface ψ_2. The wall of the device are to the right of the LCFS.

and zonal flow can smear or shear the void, thereby constraining its lifetime, and so regulating turbulence production. For typical parameters, our theory predicts:

1. the width of the NML, which is determined by ratio of the void-induced turbulence spreading and the local production, and thus depends on the void parameters, is of order 100 ρ_s;
2. the shearing rate of the void-driven zonal flow is comparable to or even exceeds the ambient shear. This qualitatively explains the observed zonal flow power bursts following the detection of voids in experiments [131];
3. the void lifetime ranges from a few to 100 μs, which encompasses the observed experimental values reasonably well.

3.2 Model development

When developing a new model from scratch, it is always valuable to draw inspiration from "golden oldies". Recall that an accelerating charged particle radiates electromagnetic waves [132]. In the context of plasma physics, another example is that a moving screened plasma test particle (macro particle) radiates plasma waves [133]. Similarly, if we think of a void as a macro particle, it is natural to consider that it would also emit waves while moving through the background plasma. The next question is: what kind of waves does the moving void emit? One way to address this is to identify which dynamical processes are relevant at the spatiotemporal scales of the voids. Experimental results indicate that the radial propagation speed of voids is comparable to the electron diamagnetic drift velocity v_* [31, 134]. This suggests that a moving void can excite drift waves, which motivates us to start from Hasegawa-Wakatani equation, the simplest model for drift waves [135].

3.2.1 Formulation of the model based on Hasegawa-Wakatani model

Equation 3.1 is the Hasegawa-Wakatani equation with the curvature drive:

$$\begin{aligned}
&\frac{d}{dt}\nabla_\perp^2\varphi + 2\kappa\frac{1}{n_0}\frac{\partial n}{\partial y} = D_\parallel\nabla_\parallel^2\left(\varphi - \frac{n}{n_0}\right),\\
&\frac{1}{n_0}\frac{d}{dt}n = D_\parallel\nabla_\parallel^2\left(\varphi - \frac{n}{n_0}\right),
\end{aligned} \tag{3.1}$$

where

$$\frac{d}{dt} = \frac{\partial}{\partial t} + \boldsymbol{v}_{E\times B}\cdot\nabla,\ D_\parallel = \frac{v_{the}^2}{\nu_{ee}}\frac{1}{\rho_s^2\omega_{ci}},\ n = n_0 + \tilde{n}. \tag{3.2}$$

For simplicity, the electrostatic potential φ, spatial and temporal coordinates, and velocities are nondimensionalized by T_e/e, ion sound speed gyroradius ρ_s, ion gyrofrequency ω_{ci}, and sound speed c_s, respectively. Here n is the plasma density, n_0 is the mean plasma density, $\kappa = \rho_s/R_c$ is the dimensionless magnetic curvature (R_c is the curvature radius of the magnetic field), v_{the} is the electron thermal velocity, and ν_{ee} is the electron-electron collision rate. To be compatible with

the presence of drift waves, the adiabatic limit ($\alpha = D_{\|} k_{\|}^2/\omega > 1$) should hold in regions away from the void. Here, $k_{\|}$ and ω are the wave vector in the direction parallel to the magnetic field and the frequency of the drift wave. In the region near the void, however, adiabatic electrons are unfavorable, as they prohibit density mixing, which is indispensable to coherent structure formation. This implies that the hydrodynamic limit ($\alpha < 1$) is relevant in the vicinity of the void, instead. Therefore, as illustrated in figure 3.2, the space of concern should be partitioned into two regimes: the near field regime where $\alpha < 1$ and the far field regime where $\alpha > 1$. By taking the corresponding limits, equation 3.1 reduces to

$$\begin{aligned} &\frac{d}{dt}\nabla_{\perp}^2 \varphi + 2\kappa \frac{1}{n_0}\frac{\partial n}{\partial y} = 0, \\ &\frac{1}{n_0}\frac{d}{dt} n = 0, \end{aligned} \tag{3.3}$$

in the near field regime and

$$\frac{d}{dt}\left(\nabla_{\perp}^2 \varphi - \varphi\right) - v_* \frac{\partial \varphi}{\partial y} = \frac{1}{n_0}\frac{dn_v}{dt} \tag{3.4}$$

in the far field regime, respectively. Note that equation 3.3 is identical to the classical two-field model (without dissipation) used to study self-propelled convection of coherent structures [34, 136, 35]. At the same time, the L.H.S. of equation 3.4 is exactly the Hasegawa-Mima (HM) equation [137]. Voids enter the model via profile modulation, i.e., $n = n_0 + n_v + \tilde{n}$, where n_v is the void density. Akin to test particle model [64], for tractability, we employ the delta-function-shaped expression for the void,

$$\frac{n_v}{n_0} = 2\pi h \Delta x \Delta y \delta\left(x + u_x t\right) \delta\left(y - u_y t\right) H\left(t\right) H\left(\tau_v - t\right), \tag{3.5}$$

where $h = |n_v|/n_0 \in (0.1, 1)$ is the void magnitude, u_x and u_y are its radial and poloidal propagation speed. The spatial extent of the void Δx and Δy appear as the weight of the delta function.

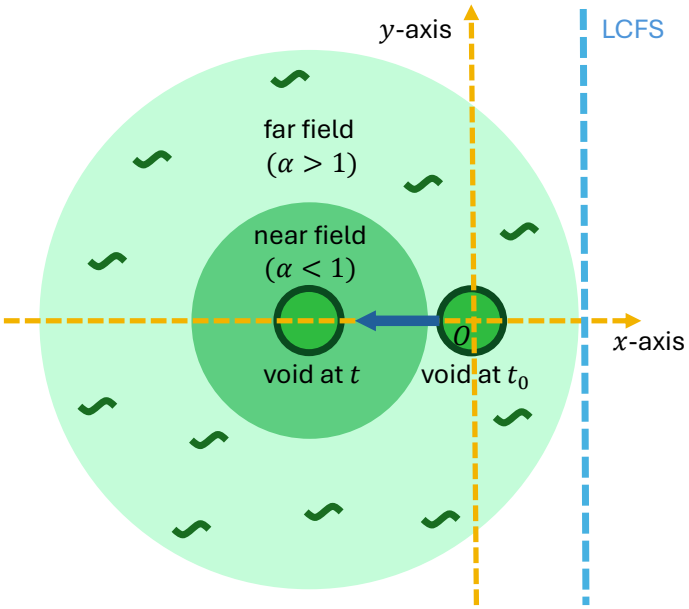

Figure 3.2. The space of concern in our model can be divided into two regimes: the near field regime near the void ($\alpha < 1$) and the far field regime away from the void ($\alpha > 1$).

In addition, a product of two Heaviside step functions is introduced to account for the finite void lifetime τ_v. Throughout the rest of the letter, we focus primarily on the far field region, where turbulence excited by voids ultimately resides.

Treating the R.H.S. of equation 3.4 as the source, we can solve the potential φ of the far field using the Green's function of the (linearized) HM equation. This approach follows that used in the dressed test particle model. See Appendix 3.A for a detailed discussion on the linearization of equation 3.4. From this solution, we can further calculate the velocity field ($\tilde{\boldsymbol{v}} = \hat{\boldsymbol{z}} \times \nabla\varphi$) and the inward turbulence intensity flux Γ_I, yielding an evaluation of void-induced spreading and the extent of the NML. The Reynolds stress ($\langle \tilde{v}_x \tilde{v}_y \rangle$) and the shearing rate of void-driven zonal flow ($\omega_s^v = -\int \partial_x^2 \langle \tilde{v}_x \tilde{v}_y \rangle dt$) can also be calculated. These allow for a direct comparison between ω_s^v and the ambient shear ω_s^a.

3.2.2 Green's function of the linearized Hasegawa-Mima equation

Given the significance of the HM equation in plasma theory, surprisingly little literature exists on its Green's function. Fortunately, the Green's function of the linearized Rossby waves equation with a finite Rossby deformation radius, which is homotopic to the linearized HM equation, has been calculated in geophysics [138, 139]. Thus the Green's function of the linearized HM equation is

$$G\left(\boldsymbol{r},t;\boldsymbol{r'},t'\right)=-\int_{c-i\infty}^{c+i\infty}\frac{ds}{2\pi i}\exp\left(s\tau+\frac{v_*\chi}{2s}\right)\frac{1}{2\pi s}\mathrm{K}_0\left[\left(1+\left(\frac{v_*}{2s}\right)^2\right)^{\frac{1}{2}}\rho\right], \tag{3.6}$$

where

$$\xi=x-x',\ \chi=y-y',\ \tau=t-t',\ \rho=\left|\boldsymbol{r}-\boldsymbol{r'}\right|, \tag{3.7}$$

and K_0 is the modified Bessel function of the second kind. As equation 3.6 is in integral form, a direct implementation of it is impractical. If we focus on the dynamics after the destruction of the void, we can utilize the asymptotic form of the Green's function in the limit of $\tau\to\infty$,

$$G\to-\frac{1}{2\pi}\frac{1}{\sqrt{v_*\rho\tau}}\cos\left[\sqrt{2v_*(\rho-\chi)\tau}\right]\quad\text{as }\tau\to\infty. \tag{3.8}$$

3.2.3 Local solutions of three limiting cases

Even so, this expression is still too complex for analytical computation. And the fact that the motion of the void has both radial and poloidal components makes solving the far field equation even more challenging. To gain physical insight, we decide to seek only the local solution for cases where the void moves purely in the radial or the poloidal direction. As labeled in figure 3.3, the three specific cases we consider and their spatial orderings are:

(a). void moving in the radial direction ($u_y=0$)

(1) the solution away from x-axis but near y-axis

$$(x \lesssim x' \sim u_x \tau_h \sim \Delta x \sim \Delta y \ll y); \tag{3.9}$$

(2) the solution near x-axis but away from y-axis

$$(y \lesssim x' \sim u_x \tau_h \sim \Delta x \sim \Delta y \ll x); \tag{3.10}$$

(b). void moving in the poloidal direction ($u_x = 0$)

(3) the solution away from x-axis but near y-axis

$$(x \lesssim y' \sim u_y \tau_v \sim \Delta x \sim \Delta y \ll y). \tag{3.11}$$

Here, $x = 0$ refers to the birth zone of the void, and $y = 0$ can be thought of as the midplane. All three cases share the same temporal ordering,

$$1/\omega_* \ll t' \sim \tau_v \ll t. \tag{3.12}$$

Note that in each case, we have $\rho < v_* \tau$ to maintain causality. And as supported by experimental results [31], we also take $u_x, u_y \lesssim v_*$ so that the perturbation excited by voids could propagate ahead of the void.

3.3 Analysis of results

3.3.1 Estimate of the the no man's land width

The far field solution φ we calculate is effectively the turbulence field excited by voids and responsible for the void-induced inward spreading. As shown in figure 3.1, compared with the penetration depth of voids, the effects of the turbulence they excite could extend deeper into

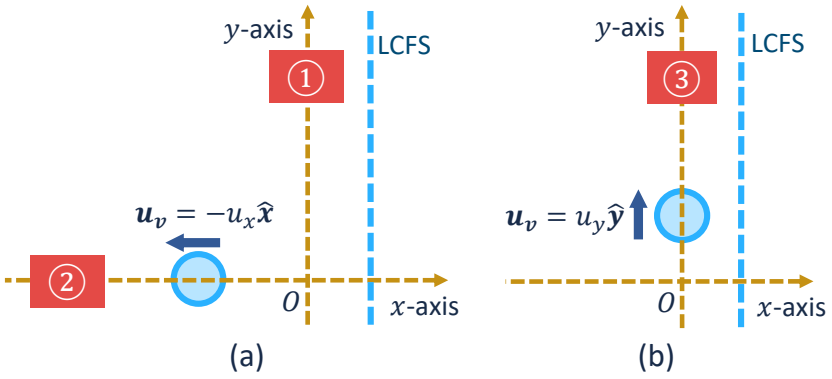

Figure 3.3. Schematic of the specific cases we examine in this work: (a) void moves purely in the radial direction; (b) void moves purely in the poloidal direction.

the main plasma ($\sim \psi_2$), and enhance the turbulence level in the NML. The balance equation for the turbulence intensity (without dissipation) is

$$\frac{\partial}{\partial t}\langle \tilde{v}^2 \rangle = -\frac{\partial}{\partial x}\langle \bar{\Gamma}_I \rangle + \kappa \langle \tilde{v}\tilde{n} \rangle . \tag{3.13}$$

On the R.H.S., $\langle \bar{\Gamma}_I \rangle$ is the turbulence intensity flux after poloidal and time averaging, and second term represents the local turbulence production rate. By integrating over the NML spanning from ψ_2 to ψ_1, we define the turbulence production ratio of turbulence spreading into the NML to overall local production in the NML as:

$$R_a = \frac{\langle \bar{\Gamma}_I \rangle\big|_{\psi_1}}{\kappa \int_{\psi_2}^{\psi_1} \langle \tilde{v}\tilde{n} \rangle \, dr}. \tag{3.14}$$

Here $\langle \bar{\Gamma}_I \rangle\big|_{\psi_2}$ is neglected, as $x = \psi_2$ can be thought of as the cutoff line of voids' influence.

Our model provides us with an approximation of Γ_I. As illustrated in figure 3.1, the gradient relaxation events, or, the edge instabilities, contain N troughs in the poloidal direction, each of which can be considered as a void emitter. The spacing between individual emitters is denoted by l, and the width of the emitter is assumed to be of the order Δy, the characteristic size of voids. After each waiting time τ_w, N voids are emitted simultaneously. If each individual void contributes a pulse with a magnitude ΔI, a duration of τ_v, and a poloidal extent of Δy, then the

total turbulence intensity flux can be estimated by the superposition of these pulses, i.e.,

$$\Gamma_I \sim \sum_{i,j} u_x \Delta I 2\pi \Delta y \tau_v \delta\left(y - il\right) \delta\left(t - j\tau_w\right), \tag{3.15}$$

where the indices i and j represent voids generated at different locations and times, respectively. Here we adopt u_x as the propagating speed of these pulses. We can think of this process as bulldozers (voids) pushing soil (turbulence pulses) at a speed of u_x. The magnitude ΔI can be obtained from the local solution at $x \to \psi_1^-$ in region 2 of figure 3.3. Consequently, the ratio given in equation 3.14 can be rewritten into

$$R_a = \left(\frac{h\Delta x \Delta y}{u_x \tau_v}\right)^2 \frac{2\pi}{v_* \tau_v^2} \frac{\Delta y}{a} \frac{\tau_v}{\tau_w} \Big/ \left(\kappa \left\langle \tilde{v}\tilde{n} \right\rangle w_{nml}\right), \tag{3.16}$$

where a is the minor radius of a tokamak. Here we adopt $N \sim \mathscr{O}(1)$, as edge instabilities are usually concentrated in the outer midplane due to the toroidal shape of fusion devices. We approximate the local turbulence production as $\kappa \left\langle \tilde{v}\tilde{n} \right\rangle w_{nml}$, where $w_{nml} = \psi_1 - \psi_2$ is the width of the NML. Since NML is a region where the effect of turbulence spreading is significant, requiring $Ra \sim 1$ defines w_{nml} as

$$w_{nml} \sim \frac{2\pi}{\kappa \left\langle \tilde{v}\tilde{n} \right\rangle} \left(\frac{h\Delta x \Delta y}{u_x \tau_v}\right)^2 \frac{1}{v_* \tau_v^2} \frac{\Delta y}{a} \frac{\tau_v}{\tau_w}. \tag{3.17}$$

Obviously, w_{nml} depends on the void magnitude, void size, and waiting time (note that u_x and τ_v are also functions of h and Δx [28]). These parameters for voids can be further related to the amplitude, spatial scale, and frequency of GREs. The fact that w_{nml} is positively correlated with h and negatively correlated with τ_w implies that the stronger and more frequent the GREs, the wider the NML. To get a better sense of how big w_{nml} is, a specific set of parameters is adopted for an estimate. When $a \sim 10^3$, $\Delta x \sim \Delta y \sim 10$, $\tau_w \sim \tau_v \sim 10^3$, $v_* \sim u_x \sim 10^{-2}$, $\tilde{v} \sim \tilde{n} \sim 10^{-2}$, $\kappa/2\pi \sim 10^{-4}$, $h \sim 0.1$, we can see $w_{nml}/\rho_s \sim \mathscr{O}(10^2)$, which is quite sensible.

3.3.2 Comparison of shearing rate of void-driven flow to ambient shear

Following the aforementioned procedure, the ratios of the resulting shearing rate of void-driven flow ω_s^v to the ambient shear ω_s^a in these three cases are also calculated and summarized by table 3.1. For $h \in (0.1, 1)$, it can be seen that ω_s^v could be comparable to ω_s^a in all three cases, and can exceed it in case (2). This result could (qualitatively) explain the correlation between zonal flow power bursts and the detection of voids in experiments [131]. We should emphasize that, although we choose a specific set of parameters for order-of-magnitude estimates of both w_{nml} and ω_s^v/ω_s^a, the conclusions do not lose generality. In practice, the values of these parameters, of course, vary across different experiments and devices. Nevertheless, the flexibility in our choice of parameters indicates that sufficiently large w_{nml} and ω_s^v/ω_s^a should exist in a considerably large portion of the parameter space. See Appendix 3.B for a brief sensitivity analysis of the quantitative results.

Table 3.1. The ratio of the shearing rate of the void-driven zonal flow to the ambient shear in all three cases. Here v_F^a and Δ_F^a are the characteristic speed and width of the ambient shear, respectively. For evaluations of ω_s^v/ω_s^a, we assume $v_F^a \sim 10^{-2}$ and $\Delta_F^a \sim 10$. See the evaluation of w_{nml} and column 3 of this table for the values of other parameters.

Case	ω_s^v/ω_s^a	Parameters
①	$\left(\frac{h\Delta x\Delta y}{v_* u_x \tau_v a}\right)^2 \frac{\Delta_F^a}{v_F^a/v_*} \sim 10h^2$	$v_*, u_x \sim 10^{-2}, x \to 0,$ $y \sim 10^2, t \sim a/v_* \sim 10^5$
②	$\left(\frac{h\Delta x\Delta y}{v_* u_x \tau_v}\right)^2 \frac{2\ln(a/v_*)\,\Delta_F^a}{x^3 v_F^a/v_*} \sim (10h)^2$	$v_*, u_x \sim 10^{-2}, x \sim 10^2,$ $y \to 0, t \sim a/v_* \sim 10^5$
③	$\frac{\pi}{2}\left(\frac{h\Delta x\Delta y}{v_* u_y \tau_v}\right)^2 \frac{x}{a^3}\frac{\Delta_F^a}{v_F^a/v_*} \sim h^2$	$v_*, 2u_y \sim 10^{-2}, x \sim 10,$ $y \sim 10^2, t \sim a/v_* \sim 10^5$

3.3.3 Prediction of the void lifetime

At this point, we already know that voids can drive drift wave turbulence and zonal flow, and thus account for the formation of a turbulent layer. But to close the feedback loop of the edge dynamics, we need to complete the other half of the story: the effects of turbulence and zonal flow on voids. One intuitive conjecture is that turbulence and flow can smear or shear the void, hence constraining the void lifetime. This process can be formulated by a diffusion equation

$$\frac{\partial}{\partial t} n_v = D \nabla_\perp^2 n_v, \tag{3.18}$$

where D is the turbulence diffusivity. Because of the properties of the diffusion equation, the magnitude of a given void will gradually decay. A practical definition of the void lifetime is the time it takes for its magnitude to decay to half of its initial value, which yields

$$\tau_v = \frac{2\Delta x^2}{D}. \tag{3.19}$$

If we consider a purely diffusive model, i.e., in the absence of shear, the turbulent diffusivity scales as $D \sim \tilde{v} l_{\mathrm{mix}}$, where the mixing length $l_{\mathrm{mix}} = L_n \rho_*^\delta$ ($\rho_* = \rho_s / L_n$, and L_n is the characteristic length of the mean density gradient) [114]. However, in the presence of ambient shear (with the same shearing rate ω_s^a as above) and assuming $\rho_* \sim 10^{-2}$, a new form of the diffusivity emerges. The ratio of D to Bohm diffusivity $D_B \sim c_s \rho_s$ and void lifetime in these two branches are:

1. in the purely diffusive regime ($D k_\perp^2 > \omega_s^a$ or $\frac{1}{2} < \delta < 1$):

$$D/D_B \simeq \rho_*^\delta, \quad \tau_v \propto \rho_*^{-\delta}; \tag{3.20}$$

2. in the shearing dominant regime ($D k_\perp^2 < \omega_s^a$ or $0 < \delta < \frac{1}{2}$):

$$D/D_B \simeq \rho_*^{(1+2\delta)/4}, \quad \tau_v \propto \rho_*^{-(1+2\delta)/4}. \tag{3.21}$$

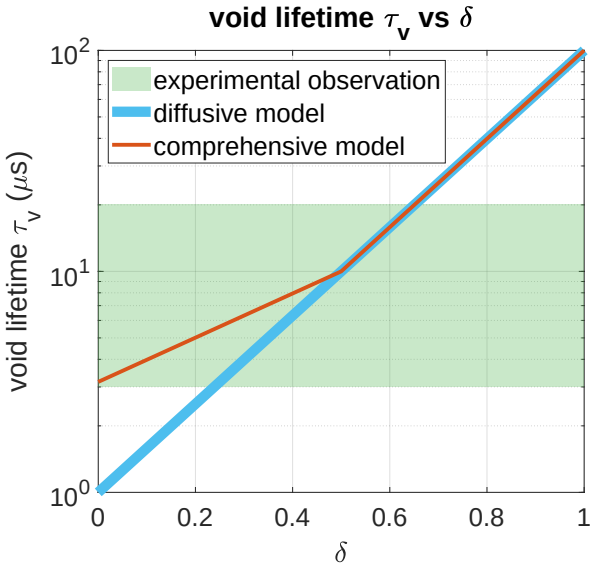

FIG. 3.4. Plot of the void lifetime as a function of δ. $\delta = \ln(l_{\text{mix}}/L_n)/\ln(\rho_*)$ is a dimensionless measure of the mixing length l_{mix} of the turbulence.

Figure 3.4 plots the predicted void lifetime as a function of δ. As can be seen, the comprehensive model (red line), which includes the ambient shear, raises the lower limit of our prediction compared with the purely diffusive model (blue line). For $\omega_{ci} \sim 10^8$ s^{-1}, the calculated void lifetime ranges from a few to 100 μs, which agrees well with experimental results on MAST (green shade) [131].

3.4 Conclusion and future plan

To summarize, by incorporating density voids into edge dynamics, we obtain quantitative estimates of the void-induced inward turbulence intensity flux, NML width, shearing rate of void-driven flow, and void lifetime. Once generated from GREs, voids can excite drift waves via Cherenkov emission, creating a edge-core coupling region of width $\sim 100\ \rho_s$, as derived from equation 3.17 for typical parameters. This picture explains the emergence of the shortfall in profile-driven gyrokinetic simulations, i.e., these suffer from the absence of GREs, void generation, and void-induced turbulence spreading. The fact that voids can drive zonal flow suggests a new mechanism of edge transport regulation. Under the effects of turbulence and zonal

flow, the void lifetime is predicted to be between a few to 100 μs. Voids, drift waves and zonal flow, constitute a new feedback loop that goes well beyond the traditional drift wave—zonal flow paradigm [16, 15]. We expect that our model applies not only to low confinement mode but also provides insights into high confinement mode, where GREs are also present as edge-localized modes. For future research, we'd like to consider the scattering of the void by the renormalized turbulent field to construct a fully self-consistent model. Since voids lose energy by emitting drift waves, this consideration may further restrain the upper limit of the predicted void lifetime. We also recommend looking for direct evidence of void—turbulence and/or void—zonal flow interactions in experiments by using wavelet bispectrum analysis.

3.A Discussion on the validity of the approximations for far field equation

Equation 3.4 is responsible for the evolution of the electrostatic potential φ in the far field region, where turbulence excited by voids ultimately resides. It is worth mentioning that in our calculation, the total derivative $d_t n_v$ on the R.H.S. of equation 3.4 is retained and approximated as $-n_v/\tau_v$, which contrasts with the linearization of the HM equation on the L.H.S ($d_t \to \partial_t$). This apparent contradiction can be reconciled as follows: although equation 3.4 describes far field evolution, the potential φ in the convection term on its R.H.S. indeed corresponds to the near field value due to the spatial localization of the void. This enables us to adopt different treatments for the convection terms on both sides of the equation.

It should also be noted that the linearization of the HM equation is strictly valid only in the $Ku < 1$ regime. Here Ku stands for the Kubo number of the turbulence and is defined as

$$Ku = \frac{\tau_{ac}\tilde{V}}{\Delta_c}, \tag{3.22}$$

where τ_{ac} and Δ_c are the auto-correlation time and the decorrelation length of the fluctuating field. $\tilde{V}$ is the root mean square of the fluctuating velocity. Regarding the validity of $Ku < 1$

assumption, it should be noted that no systematic study of edge turbulence Kubo number is as yet available. Some relevant simulation studies focus on near marginal, weak turbulence regimes, which are the characteristics of the plasma core. For such cases, the finding $Ku < 1$ is no surprise. However, the fluctuation levels do increase approaching the last closed flux surface, so it's likely that Ku does also, and at least approaches unity at the boundary.

Even so, the theory presented in this work is still defensible. Since we are focusing on the far field region, the deeper into the no man's land (NML) the void-induced turbulence penetrates, the weaker the ambient turbulence becomes. Thus the linear/quasi-linear ansatz's validity in the NML improves as void-induced turbulence penetrates. In the $Ku \sim 1$ region at the boundary (since $Ku \sim 1$ means that linear and non-linear time scales are comparable), the existing theory can be expected to be qualitatively valid, modulo a numerical correction.

An improved theory should address the nonlinear dynamics in the $Ku \sim 1$ region at the boundary. Besides computational studies, an analytically tractable possibility is to relate the problem to propagation of waves in a random media. Here, a fixed ensemble of scattering fluctuations, with profile tailored to that of the assumed Ku profile, could be posited ab-initio. Drift wave propagation could then be studied as a model of strong wave scattering.

3.B Sensitivity analysis of the quantitative predictions to parameters

In this paper, we make order-of-magnitude estimates of the NML width w_{nml}, the ratio of the shearing rate of void-driven zonal flow to the ambient shear ω_s^v/ω_s^a, and the void lifetime τ_v. As these variables depend on the void properties and other plasma parameters, their values necessarily vary across different experiments and devices. Herein we attempt to discuss the sensitivity of these quantitative predictions.

At first glance, equation 3.17 indicates that w_{nml} is very sensitive to the spatial extent of the voids. For regular voids with $\Delta x \sim \Delta y$, it appears that $w_{nml} \propto \Delta y^5$. In addition, as $w_{nml} \propto h^2$,

w_{nml} is also sensitive to the void magnitude. But, recall that u_x and τ_v are also functions of Δy and h. By using expressions for u_x and τ_v obtained from two-field model [34] and equation 3.19, respectively, we have

$$w_{nml} \propto \frac{\varepsilon R}{\rho_*^{3(1-\delta)}} \frac{h}{\Delta y^2 \tau_w}, \tag{3.23}$$

Here the magnetic curvature radius R_c is taken as the major radius R, and $\varepsilon = R/a$ is a geometric factor of fusion devices called aspect ratio. Since now $w_{nml} \propto h\Delta y^{-2}\tau_w^{-1}$, the sensitivity of w_{nml} to h and Δy is appreciably reduced, though Δy remains the most sensitive parameter of voids for w_{nml}. As voids are generated from GREs, parameters h, Δy, and τ_w^{-1} can be physically mapped to the magnitude A_g, spatial scale λ_g, and frequency f_g of the edge instabilities (GREs), respectively. This leads to the scaling $w_{nml} \propto A_g \lambda_g^{-2} f_g$. In equation 3.23, there are other parameters that also influence w_{nml}. For conventional tokamaks, ε varies very little, resulting in a negligible effect on w_{nml}. There is a weak dependence of w_{nml} on the device size as $w_{nml} \propto R$. As $0 < \delta < 1$, w_{nml} may also exhibit a moderate dependence on ρ_*, or equivalently, L_n.

The same idea applies to the analysis of ω_s^v/ω_s^a. Here, we concentrate on the case (2) in table 3.1, in which ω_s^v/ω_s^a manifests its strongest value and is used to explain the experimental observation. After substituting the expressions for u_x and τ_v, the scaling of ω_s^v/ω_s^a becomes

$$\frac{\omega_s^v}{\omega_s^a} \propto \frac{hR}{\Delta y} \rho_*^{(2\delta-1)} \frac{\Delta_F^a}{v_F^a} \frac{1}{x^3}, \tag{3.24}$$

where the logarithm factor is omitted for a sensitivity analysis. Clearly, ω_s^v/ω_s^a is the most sensitive to x, the distance to the void birth zone. The deeper into the core and the farther from the void birth zone, the weaker the void's influence—including the zonal flow driven by it—becomes, which aligns with physical intuition. In this study, we select $x \sim 100\rho_s$ as a reference. This choice not only places the coordinate point within the NML—where the void's influence remains significant—but also fulfills the required spatial ordering in case (2). As for the other parameters in equation 3.24, given that $|2\delta - 1| < 1$, their exponents are all ≤ 1. Therefore,

since the parameter values adopted in the order-of-magnitude estimates of this work are typical, we expect that the variations of these parameters in different experiments and devices will not cause a drastic variation in ω_s^v/ω_s^a.

Last, based on equation 3.19, the void lifetime is sensitive to the void size as $\tau_v \propto \Delta x^2 \sim \Delta y^2$. In experiments, the size of coherent structures is usually on the order of $10\rho_s$. Consequently, voids with larger sizes tend to exhibit longer lifetimes compared to the void with $\Delta x \sim 10\rho_s$ examined in this work. Nevertheless, as discussed at the end of the text, voids can lose energy and thus decay faster by emitting drift waves. For larger voids, while being passively destructed by turbulence, this mechanism will further constrain their lifetime. Constructing a fully self-consistent model which could possibly reduce the dispersion of the predicted τ_v caused by the size variation of voids will be a topic for future research.

Chapter 3, in full, is a reprint of the material as it appears in *Physical Review Letters* 134:235101 (2025). Cao, Mingyun; Diamond, P.H., American Physical Society, 2025. The dissertation author was the primary investigator and author of this paper.

Chapter 4

Summary and Future Research

At present, one major direction of fusion development lies in reconciling good confinement with adequate power handling and boundary control. This calls a further enrichment of the theoretical framework of plasma turbulence. As plasma turbulence can be treated as a multi-ingredient "soup", this dissertation adds three new "ingredients" to the recipe of "plasma soup".

4.1 Impact of magnetic stochasticity and toroidicity on instability evolution and transport

The first ingredient we add is magnetic stochasticity. In Chapter 1, we present a detailed analytic theory of an electrostatic resistive interchange mode in an externally-prescribed, static, and ambient stochastic magnetic field. This work is motivated by the discovery that resonant magnetic perturbations (RMPs) increases the power threshold of L-H transition while mitigating and suppressing edge-localized modes (ELMs). A microturbulence is driven by the beat of the large-scale cell and the small-scale magnetic perturbations to produce a perpendicular current density fluctuation $\tilde{\boldsymbol{J}}_{\perp}$ so as to maintain the quasi-neutrality. The microturbulence can react on the large-scale cell via an effective turbulent viscosity and diffusivity, as well as electrostatic scattering. In this way, dynamics at large and small scales are coupled. The net effect of magnetic stochasticity is predicted to suppress the growth of the resistive interchange mode via magnetic

braking, enhanced turbulent mixing, and electrostatic scattering. The first-order correction to the mode growth rate is calculated using a perturbation method. Another important finding is a non-trivial correlation between the velocity fluctuations $\tilde{v}_x$ and magnetic perturbations $\tilde{b}_x$, indicating that the edge turbulence becomes more "noisy" with the presence of a stochastic magnetic field. This physical picture qualitatively explains the reduction in the Jensen-Shannon complexity during the RMP-ELM suppression phase in experiments. The scaling of the turbulent viscosity and diffusivity is calculated via a simple nonlinear closure theory.

On top of our analysis of stochasticity effects on plasma instabilities, we take a further step in Chapter 2 by blending in a new ingredient, i.e., toroidicity. Given that peeling-ballooning mode is a quite probable mechanism for ELMs, understanding how a stochastic magnetic field affects ballooning mode is crucial for boundary control. However, one reality is that models for ballooning mode are set up in a toroidal geometry while theories involving RMPs typically focus on resonant surfaces in a cylindrical geometry. This geometry disparity is reconciled by exploiting the resemblance between the quasi-mode and the ballooning mode. The quasi-mode is a wave-packet composed of resistive interchange modes in a cylinder, owning a mode structure similar to that of the ballooning mode in a torus. This allows us to first study the dynamics of quasi-mode in a stochastic magnetic field, and then extend the results to the toroidal case. Duo to the broader mode structure of the quasi-mode (compared to the resistive interchange mode), several conclusions drawn in the Chapter 1 are changed, suggesting the effects of toroidicity on the instability relaxation in a background stochastic magnetic field. While the micro-turbulent still "locks on" to the ambient stochasticity, a new correlation $\langle \tilde{b}_y \tilde{v}_x \rangle$ develops. The turbulent viscosity and diffusivity resulting from the microturbulence turn out to be larger. A new mechanism for the stabilization of plasma instabilities by stochastic magnetic fields is identified—namely, through the reduction in the effective drive.

Although this dissertation focuses on the effects of stochasticity on MHD instabilities, such as resistive interchange modes and quasi-modes, our conclusions are broadly applicable to other types of instabilities, including drift waves, due to the universality of the quasi-neutral

condition $\nabla \cdot \boldsymbol{J} = 0$. Therefore, no matter what the dominant mode at the edge is, once RMP is turned on, the microturbulence will inevitably be driven and correlation between the microturbulence and the magnetic stochasticity will emerge. Accordingly, extending this analysis to a kinetic description constitutes a logical next step. Since the ambient stochastic magnetic fields will scatter particle streaming, we should modify the parallel derivative operator in the drift kinetic equation: $v_\parallel \nabla_\parallel \to v_\parallel \left(\nabla_\parallel^{(0)} + \tilde{\boldsymbol{b}} \cdot \nabla_\perp \right)$. Another promising theoretical direction is to incorporate zonal flow into the model, which is currently absent. The observed increase in the L-H transition power threshold with applied RMPs may be attributed to the weakening of zonal flows by stochastic magnetic fields. As discussed in section 0.2.3, zonal flow is driven by the Reynolds stress $\langle \tilde{v}_x \tilde{v}_y \rangle$, which indicates a non-zero correlation between k_x and k_y, i.e., $\langle k_x k_y \rangle \neq 0$. Figure 3 illustrates how a non-trivial $\langle k_x k_y \rangle$ can develop from an initially weak velocity shear $\bar{v}$, as described by

$$\frac{dk_x}{dt} = -k_y \frac{\partial \bar{v}}{\partial x}. \tag{4.1}$$

It should be noted, however, that, the geometric effects can also couple k_x and k_y through

$$\frac{dk_x}{dz} = -\frac{k_y}{L_s}, \tag{4.2}$$

where L_s is the characteristic length of the magnetic shear. The similarity in structure between equation 4.1 and equation 4.2 offers useful insight for future studies.

The development of plasma turbulence diagnostics opens the possibility of experimentally validating our theoretical predictions. We can perform the complexity-entropy analysis—introduced in section 2.A—for the data of velocity fluctuations collected from BES velocimetry during both RMP ELM suppression phase and natural ELM-free phase. This not only complements existing experimental results, but also provides a direct test of our theory. A lower Jensen-Shannon complexity is anticipated in the RMP ELM suppression phase, in which the turbulence "locks on" to the ambient magnetic stochasticity and thereby becomes more "noisy".

4.2 Edge-core coupling by void-induced inward turbulence spreading

The last ingredient we introduce to the recipe is the nonlocality of plasma turbulence—more specifically, turbulence spreading. In Chapter 3, we turn our attention to the dynamics of edge-core coupling, which is critically important to optimal plasma performance. Nevertheless, the physics of what sets the width of the edge-core coupling region—where local gyrokinetic simulations sometimes under-predict the turbulence level—has long been a "known unknown". Recent experiments revealed that gradient relaxation events (GREs) very close to the separatrix generate blobs and voids in pairs. Here blobs and voids are plasma filaments with large-amplitude positive or negative density fluctuations and long lifetimes. While blobs propagate outward and detach from the bulk plasma, voids move inward, and so energize the core plasma, in accord with a long-standing, albeit broader speculation by B.B. Kadomtsev. Here, by developing a model incorporating voids into turbulence dynamics, we demonstrate that the Cherenkov emission of drift waves from voids can drive substantial inward turbulence spreading that couples the edge and core. These drift waves are ultimately regulated by a self-generated zonal flow, whose shearing rate could match or even exceed the ambient shear. The turbulent layer—where the contribution of nonlocal turbulence spreading to the turbulence level is comparable to that of the local turbulence production—has a width of$\sim 100\ \rho_s$ for typical parameters. Another outcome of this work is the prediction of the void lifetime τ_v as a function of $\delta = \ln(l_{mix}/L_n)/\ln(\rho_*)$, a dimensionless measure of the mixing length l_{mix} of the turbulence. The estimated τ_v, ranging from a few to 100 μs, is consistent with experimental findings. Our model could potentially explain the emergence of the shortfall problem in profile-driven gyrokinetic simulations—i.e., they suffer from the absence of GREs and void-induced turbulence spreading. While the model in this chapter is developed in the context of L-mode, we believe that it also provides insights into H-mode. ELMs in H-mode can also be viewed as a type of gradient relaxation events. The plasma filaments arising from ELMs exhibit structures similar to the blobs and voids in L-mode,

but with larger amplitude.

It is worth noting that the closure of the model presented in Chapter 3 is simplified. As indicated by equation 3.18, voids only passively under the smearing of the background turbulence. However, as voids lose energy via the emission of drift waves, the present model likely overestimates their lifetime. Then, a future direction is to construct a fully self-consistent model. The "radiation field" excited by the void is expected to exert a reaction force on it, which in turn accelerates its decay. Given that the physical picture of this work suggests that voids can excite drift wave turbulence and zonal flows, We also propose using wavelet bispectrum analysis in experiments to seek direct evidence of void—turbulence and/or void—zonal flow interactions.

4.3 Epilogue: Kubo number

The three studies included in this dissertation have substantially expanded our understanding of plasma turbulence, Yet they barely mark the halfway point toward what could be considered a full success. In retrospect, both the adoption of quasi-linear methods in Chapters 1 and 2 and the linearization of Hasegawa-Mima equation in Chapter 3 rely on the assumption that the Kubo number (Ku) of edge turbulence is less than unity. However, since the fluctuation levels do increase toward the last closed flux surface, it is likely that Ku increases as well and at least approaches one at the boundary. For a long time, the dynamics of plasma turbulence with $Ku \sim 1$ has remained largely unexplored. With the dynamics of $Ku < 1$ regime now well understood, it would be beneficial to explore the $Ku \sim 1$ regime from another perspective—namely, by extending theories developed for $Ku > 1$ regime to the $Ku \sim 1$ regime. For the study of plasma dynamics in a stochastic magnetic field, valuable insights could be drawn from the work on 2D guiding center plasma, in which the transport behaves more like a percolation process rather than a diffusion process. Regarding the study of void-induced inward turbulence spreading, the $Ku > 1$ scenario can be related to wave propagation in random media. Then the propagation of drift waves will be strongly scattered by a fixed ensemble of fluctuations, whose profile can be

set manually to match the assumed Ku profile.

Bibliography

[1] R. Toschi. Nuclear fusion, an energy source. *Fusion Engineering and Design*, 36(1):1–8, Apr 1997.

[2] S. Yang, F. Zhang, H. Ding, P. He, and H. Zhou. Lithium metal extraction from seawater. *Joule*, 2(9):1648–1651, Sep 2018.

[3] A.M. Bradshaw, T. Hamacher, and U. Fischer. Is nuclear fusion a sustainable energy form? *Fusion Engineering and Design*, 86(9):2770–2773, Oct 2011.

[4] M. Kikuchi, K. Lackner, and M.Q. Tran. *Fusion Physics*. IAEA, Sep 2012.

[5] M.L.E. Oliphant, P. Harteck, and E. Rutherford. Transmutation effects observed with heavy hydrogen. *Proceedings of the Royal Society of London. Series A, Containing Papers of a Mathematical and Physical Character*, 144(853):692–703, May 1934.

[6] G. Xu, Z. Lu, D. Chen, and B. Wan. A promising approach to steady-state fusion: High-temperature superconducting strong-field stellarator with precise omnigenity. *The Innovation*, 5(1), Jan 2024.

[7] M.R. Wade and J.A. Leuer. Cost drivers for a tokamak-based compact pilot plant. *Fusion Science and Technology*, 77(2):119–143, 2021.

[8] J. Wesson and D.J. Campbell. *Tokamaks*. International series of monographs on physics. Clarendon Press-Oxford, 2004.

[9] N.J. Peacock, D.C. Robinson, M.J. Forrest, P.D. Wilcock, and V.V. Sannikov. Measurement of the electron temperature by thomson scattering in tokamak t3. *Nature*, 224(5218):488–490, Nov 1969.

[10] Jr. L. Spitzer. Particle diffusion across a magnetic field. *The Physics of Fluids*, 3(4):659–661, 07 1960.

[11] D. Gough. The current state of stellar mixing-length theory. *International Astronomical Union Colloquium*, 38:15–56, 1977.

[12] H. Eubank, R. Goldston, V. Arunasalam, M. Bitter, K. Bol, D. Boyd, N. Bretz, J.-P. Bussac, S. Cohen, P. Colestock, S. Davis, D. Dimock, H. Dylla, P. Efthimion, L. Grisham, R. Hawryluk, K. Hill, E. Hinnov, J. Hosea, H. Hsuan, D. Johnson, G. Martin, S. Medley,

E. Meservey, N. Sauthoff, G. Schilling, J. Schivell, G. Schmidt, F. Stauffer, L. Stewart, W. Stodiek, R. Stooksberry, J. Strachan, S. Suckewer, H. Takahashi, G. Tait, M. Ulrickson, S. von Goeler, M. Yamada, C. Tsai, W. Stirling, W. Dagenhart, W. Gardner, M. Menon, and H. Haselton. Neutral-beam-heating results from the princeton large torus. *Phys. Rev. Lett.*, 43:270–274, Jul 1979.

[13] R.J. Goldston. Energy confinement scaling in tokamaks: some implications of recent experiments with ohmic and strong auxiliary heating. *Plasma Physics and Controlled Fusion*, 26(1A):87, Jan 1984.

[14] F. Wagner, G. Becker, K. Behringer, D. Campbell, A. Eberhagen, W. Engelhardt, G. Fussmann, O. Gehre, J. Gernhardt, G. v. Gierke, G. Haas, M. Huang, F. Karger, M. Keilhacker, O. Klüber, M. Kornherr, K. Lackner, G. Lisitano, G.G. Lister, H.M. Mayer, D. Meisel, E.R. Müller, H. Murmann, H. Niedermeyer, W. Poschenrieder, H. Rapp, H. Röhr, F. Schneider, G. Siller, E. Speth, A. Stäbler, K.H. Steuer, G. Venus, O. Vollmer, and Z. Yü. Regime of improved confinement and high beta in neutral-beam-heated divertor discharges of the asdex tokamak. *Physical Review Letters*, 49:1408–1412, Nov 1982.

[15] P.H. Diamond, Y.-M. Liang, B.A. Carreras, and P.W. Terry. Self-regulating shear flow turbulence: A paradigm for the l to h transition. *Physical Review Letters*, 72:2565–2568, Apr 1994.

[16] P.H. Diamond, S.-I. Itoh, K. Itoh, and T.S. Hahm. Zonal flows in plasma—a review. *Plasma Physics and Controlled Fusion*, 47(5):R35–R161, Apr 2005.

[17] K. Itoh, S.-I. Itoh, P.H. Diamond, T.S. Hahm, A. Fujisawa, G.R. Tynan, M. Yagi, and Y. Nagashima. Physics of zonal flowsa). *Physics of Plasmas*, 13(5):055502, 05 2006.

[18] T.S. Hahm, G.J. Choi, S.J. Park, and Y.-S. Na. Fast ion effects on zonal flow generation: A simple model. *Physics of Plasmas*, 30(7):072501, 07 2023.

[19] G.I. Taylor and W.N. Shaw. I. eddy motion in the atmosphere. *Philosophical Transactions of the Royal Society of London. Series A, Containing Papers of a Mathematical or Physical Character*, 215(523-537):1–26, 1915.

[20] A.I. Smolyakov and P.H. Diamond. Generalized action invariants for drift waves-zonal flow systems. *Physics of Plasmas*, 6(12):4410–4413, 12 1999.

[21] D.G. Whyte, A.E. Hubbard, J.W. Hughes, B. Lipschultz, J.E. Rice, E.S. Marmar, M. Greenwald, I. Cziegler, A. Dominguez, T. Golfinopoulos, N. Howard, L. Lin, R.M. McDermott, M. Porkolab, M.L. Reinke, J. Terry, N. Tsujii, S. Wolfe, S. Wukitch, Y. Lin, and the Alcator C-Mod Team. I-mode: an h-mode energy confinement regime with l-mode particle transport in alcator c-mod. *Nuclear Fusion*, 50(10):105005, Oct 2010.

[22] A.M. Messiaen, J. Ongena, U. Samm, B. Unterberg, P.E. Vandenplas, G. Van Oost, G. Van Wassenhove, J. Winter, D. Boucher, P. Dumortier, F. Durodie, H.G. Esser, H. Euringer, B. Giesen, E. Hintz, M. Lochter, M.Z. Tokar, G.H. Wolf, G. Fuchs, D.L. Hillis, F. Hoenen,

P. Huttemann, R. Koch, L. Konen, H.R. Koslowski, A. Kramer-Flecken, D. Pettiaux, A. Pospieszczyk, B. Schweer, H. Soltwisch, G. Telesca, R. Uhlemann, R. van Nieuwenhove, M. Vervier, G. Waidmann, and R.R. Weynants. Improved confinement with edge radiative cooling at high densities and high heating power in textor. *Nuclear Fusion*, 34(6):825, Jun 1994.

[23] P.A. Robinson. Nonlinear wave collapse and strong turbulence. *Rev. Mod. Phys.*, 69:507–574, Apr 1997.

[24] T.E. Evans, R.A. Moyer, K.H. Burrell, M.E. Fenstermacher, I. Joseph, A.W. Leonard, T.H. Osborne, G.D. Porter, M.J. Schaffer, P.B. Snyder, P.R. Thomas, J.G. Watkins, and W.P. West. Edge stability and transport control with resonant magnetic perturbations in collisionless tokamak plasmas. *Nature Physics*, 2(6):419–423, Jun 2006.

[25] K.H. Burrell, M.E. Austin, D.P. Brennan, J.C. DeBoo, E.J. Doyle, C. Fenzi, C. Fuchs, P. Gohil, C.M. Greenfield, R.J. Groebner, L.L. Lao, T.C. Luce, M.A. Makowski, G.R. McKee, R.A. Moyer, C.C. Petty, M. Porkolab, C.L. Rettig, T.L. Rhodes, J.C. Rost, B.W. Stallard, E.J. Strait, E.J. Synakowski, M.R. Wade, J.G. Watkins, and W.P. West. Quiescent double barrier high-confinement mode plasmas in the diii-d tokamak. *Physics of Plasmas*, 8(5):2153–2162, 05 2001.

[26] J.W. Connor, R.J. Hastie, and J.B. Taylor. Shear, periodicity, and plasma ballooning modes. *Phys. Rev. Lett.*, 40:396–399, Feb 1978.

[27] E.A. Frieman and L. Chen. Nonlinear gyrokinetic equations for low-frequency electromagnetic waves in general plasma equilibria. *The Physics of Fluids*, 25(3):502–508, 03 1982.

[28] D.A. D'Ippolito, J.R. Myra, and S.J. Zweben. Convective transport by intermittent blob-filaments: Comparison of theory and experiment. *Physics of Plasmas*, 18(6):060501, 06 2011.

[29] F. Laggner. *Inter-ELM pedestal structure development in ASDEX Upgrade*. PhD thesis, Max-Planck-Institut für Plasmaphysik, 2017.

[30] H. Zohm. Edge localized modes (elms). *Plasma Physics and Controlled Fusion*, 38(2):105, Feb 1996.

[31] T. Long, P.H. Diamond, R. Ke, Z. Chen, M. Cao, X. Xu, M. Xu, R. Hong, W. Tian, J. Yuan, Y. Liu, Q. Yan, Q. Yang, C. Shen, W. Guo, L. Wang, L. Nie, Z. Wang, G. Hao, N. Wang, Z. Chen, Y. Pan, J. Li, W. Chen, and W. Zhong. On how structures convey non-diffusive turbulence spreading. *Nuclear Fusion*, 64(6):064002, May 2024.

[32] F.O. Khabanov, R. Hong, P.H. Diamond, G.R. Tynan, Z. Yan, G.R. McKee, C. Chrystal, F. Scotti, G. Yu, S.A. Zamperini, and Y. Zhu. Density fluctuation statistics and turbulence spreading at the edge of l–mode plasmas. *Nuclear Fusion*, 64(12):126056, Oct 2024.

[33] S.I. Krasheninnikov, D.A. D'Ippolito, and J.R. Myra. Recent theoretical progress in understanding coherent structures in edge and sol turbulence. *Journal of Plasma Physics*, 74(5):679–717, 2008.

[34] O.E. Garcia, N.H. Bian, V. Naulin, A.H. Nielsen, and J.J. Rasmussen. Mechanism and scaling for convection of isolated structures in nonuniformly magnetized plasmas. *Physics of Plasmas*, 12(9):090701, 09 2005.

[35] J.R. Myra, D.A. Russell, and D.A. D'Ippolito. Collisionality and magnetic geometry effects on tokamak edge turbulent transport. i. a two-region model with application to blobs. *Physics of Plasmas*, 13(11):112502, 11 2006.

[36] J.B. Taylor. Relaxation of toroidal plasma and generation of reverse magnetic fields. *Physical Review Letters*, 33:1139–1141, Nov 1974.

[37] F. Wagner. A quarter-century of h-mode studies. *Plasma Physics and Controlled Fusion*, 49(12B):B1, Nov 2007.

[38] M. Kikuchi, T. Takizuka, S. Medvedev, T. Ando, D. Chen, J.X. Li, M. Austin, O. Sauter, L. Villard, A. Merle, M. Fontana, Y. Kishimoto, and K. Imadera. L-mode-edge negative triangularity tokamak reactor. *Nuclear Fusion*, 59(5):056017, Apr 2019.

[39] E. Wang, X. Xu, J. Candy, R.J. Groebner, P.B. Snyder, Y. Chen, S.E. Parker, W. Wan, Gaimin Lu, and J.Q. Dong. Linear gyrokinetic analysis of a DIII-d h-mode pedestal near the ideal ballooning threshold. *Nuclear Fusion*, 52(10):103015, Sep 2012.

[40] C.-C. Chen, P.H. Diamond, R. Singh, and S.M. Tobias. Potential vorticity transport in weakly and strongly magnetized plasmas. *Physics of Plasmas*, 28(4):042301, Apr 2021.

[41] W. Guo, M. Jiang, P.H. Diamond, C.-C. Chen, M. Cao, H. Li, and T. Long. Theory of mean exb shear in a stochastic magnetic field: ambipolarity breaking and radial current. *Plasma Physics and Controlled Fusion*, 64(12):124001, Oct 2022.

[42] C.-C. Chen and P.H. Diamond. Potential vorticity mixing in a tangled magnetic field. *The Astrophysical Journal*, 892(1):24, Mar 2020.

[43] D. Sharma, Y. Feng, and F. Sardei. 3d study of energy transport and role of stochasticity in the w7-x edge. *Plasma Physics and Controlled Fusion*, 48(1):157–167, Dec 2005.

[44] K. Ida, T. Kobayashi, M. Yoshinuma, Y. Suzuki, Y. Narushima, T.E. Evans, S. Ohdachi, H. Tsuchiya, S. Inagaki, and K. Itoh. Bifurcation physics of magnetic islands and stochasticity explored by heat pulse propagation studies in toroidal plasmas. *Nuclear Fusion*, 56(9):092001, Jul 2016.

[45] A.H. Boozer. Theory of tokamak disruptions. *Physics of Plasmas*, 19(5):058101, 2012.

[46] A.B. Rechester and M.N. Rosenbluth. Electron heat transport in a tokamak with destroyed magnetic surfaces. *Physical Review Letters*, 40:38–41, Jan 1978.

[47] K. Ida, Y. Miura, K. Itoh, S. I. Itoh, and A. Fukuyama. Thickness of ExB velocity shear at the plasma edge in the JFT-2m h-mode. *Plasma Physics and Controlled Fusion*, 36(7A):A279–A284, Jul 1994.

[48] P. K. Kaw, E. J. Valeo, and P.H. Rutherford. Tearing modes in a plasma with magnetic braiding. *Physical Review Letters*, 43:1398–1401, Nov 1979.

[49] H.R. Strauss. Hyper-resistivity produced by tearing mode turbulence. *The Physics of Fluids*, 29(11):3668–3671, 1986.

[50] A. Bhattacharjee and E. Hameiri. Self-consistent dynamolike activity in turbulent plasmas. *Physical Review Letters*, 57:206–209, Jul 1986.

[51] X.Q. Xu, B. Dudson, P.B. Snyder, M.V. Umansky, and H. Wilson. Nonlinear simulations of peeling-ballooning modes with anomalous electron viscosity and their role in edge localized mode crashes. *Physical Review Letters*, 105:175005, Oct 2010.

[52] B.B. Kadomtsev and O.P. Pogutse. Electron heat conductivity of the plasma across a 'braided' magnetic field. In *Plasma Physics and Controlled Nuclear Fusion Research 1978*, volume 1, pages 649–662, January 1979.

[53] R. Singh and P.H. Diamond. A unified theory of zonal flow shears and density corrugations in drift wave turbulence. *Plasma Physics and Controlled Fusion*, 63(3):035015, Jan 2021.

[54] C.J. McDevitt, X.-Z. Tang, and Z. Guo. Turbulence-driven bootstrap current in low-collisionality tokamaks. *Physical Review Letters*, 111:205002, Nov 2013.

[55] A. Ishizawa and N. Nakajima. Excitation of macromagnetohydrodynamic mode due to multiscale interaction in a quasi-steady equilibrium formed by a balance between microturbulence and zonal flow. *Physics of Plasmas*, 14(4):040702, 2007.

[56] P.H. Rutherford. Nonlinear growth of the tearing mode. *The Physics of Fluids*, 16(11):1903–1908, 1973.

[57] H.R. Strauss. Nonlinear, three-dimensional magnetohydrodynamics of noncircular tokamaks. *The Physics of Fluids*, 19(1):134–140, 1976.

[58] Y-K.M. Peng and D.J. Strickler. Features of spherical torus plasmas. *Nuclear Fusion*, 26(6):769–777, Jun 1986.

[59] H.P. Furth, J. Killeen, and M.N. Rosenbluth. Finite-resistivity instabilities of a sheet pinch. *The Physics of Fluids*, 6(4):459–484, 1963.

[60] B. Coppi, J.M. Greene, and J.L. Johnson. Resistive instabilities in a diffuse linear pinch. *Nuclear Fusion*, 6(2):101–117, Jun 1966.

[61] B.A. Carreras, V.E. Lynch, L. Garcia, and P.H. Diamond. Resistive pressure-gradient-driven turbulence with self-consistent flow profile evolution. *Physics of Fluids B: Plasma Physics*, 5(5):1491–1505, 1993.

[62] T.H. Dupree. A perturbation theory for strong plasma turbulence. *The Physics of Fluids*, 9(9):1773–1782, 1966.

[63] B.A. Carreras, L. Garcia, and P.H. Diamond. Theory of resistive pressure-gradient-driven turbulence. *The Physics of Fluids*, 30(5):1388–1400, 1987.

[64] P.H. Diamond, S.-I. Itoh, and K. Itoh. *Modern Plasma Physics*, volume 1. Cambridge University Press, 2010.

[65] N.G. Van Kampen. *Stochastic processes in physics and chemistry*. Elsevier, 1992.

[66] J. Sethna. *Statistical mechanics: entropy, order parameters, and complexity*. Oxford University Press, 2021.

[67] P. Beyer, X. Garbet, and P. Ghendrih. Tokamak turbulence with stochastic field lines. *Physics of Plasmas*, 5(12):4271–4279, 1998.

[68] M.J. Choi, J.-M. Kwon, J. Kim, T. Rhee, J.-G. Bak, G. Shin, H.-S. Kim, H. Jhang, K. Kim, G.-S. Yun, M. Kim, S. Kim, H.H. Kaang, J.-K. Park, H.-H. Lee, Y. In, J. Lee, M. Kim, B.-H. Park, and H.-K. Park. Stochastic fluctuation and transport of tokamak edge plasmas with the resonant magnetic perturbation field. *Physics of Plasmas*, 29(12):122504, 12 2022.

[69] O.A. Rosso, H.A. Larrondo, M.T. Martin, A. Plastino, and M.A. Fuentes. Distinguishing noise from chaos. *Physical Review Letters*, 99:154102, Oct 2007.

[70] J. E. Hirsch, B. A. Huberman, and D. J. Scalapino. Theory of intermittency. *Phys. Rev. A*, 25:519–532, Jan 1982.

[71] K.V. Roberts and J.B. Taylor. Gravitational resistive instability of an incompressible plasma in a sheared magnetic field. *The Physics of Fluids*, 8(2):315–322, 1965.

[72] J.W. Connor, R.J. Hastie, and J.B. Taylor. Shear, periodicity, and plasma ballooning modes. *Physical Review Letters*, 40:396–399, Feb 1978.

[73] A.B. Rechester, M.N. Rosenbluth, and R.B. White. Calculation of the kolmogorov entropy for motion along a stochastic magnetic field. *Physical Review Letters*, 42:1247–1250, May 1979.

[74] T. Eich, A.W. Leonard, R.A. Pitts, W. Fundamenski, R.J. Goldston, T.K. Gray, A. Herrmann, A. Kirk, A. Kallenbach, O. Kardaun, A.S. Kukushkin, B. LaBombard, R. Maingi, M.A. Makowski, A. Scarabosio, B. Sieglin, J. Terry, A. Thornton, ASDEX Upgrade Team, and JET EFDA Contributors. Scaling of the tokamak near the scrape-off layer h-mode power width and implications for iter. *Nuclear Fusion*, 53(9):093031, Aug 2013.

[75] Y. Sun, Y. Liang, Y. Q. Liu, S. Gu, X. Yang, W. Guo, T. Shi, M. Jia, L. Wang, B. Lyu, C. Zhou, A. Liu, Q. Zang, H. Liu, N. Chu, H. H. Wang, T. Zhang, J. Qian, L. Xu, K. He, D. Chen, B. Shen, X. Gong, X. Ji, S. Wang, M. Qi, Y. Song, Q. Yuan, Z. Sheng,

G. Gao, P. Fu, and B. Wan. Nonlinear transition from mitigation to suppression of the edge localized mode with resonant magnetic perturbations in the east tokamak. *Physical Review Letters*, 117:115001, Sep 2016.

[76] F. Ryter, S.K. Rathgeber, L.B. Orte, M. Bernert, G.D. Conway, R. Fischer, T. Happel, B. Kurzan, R.M. McDermott, A. Scarabosio, W. Suttrop, E. Viezzer, M. Willensdorfer, E. Wolfrum, and the ASDEX Upgrade Team. Survey of the h-mode power threshold and transition physics studies in asdex upgrade. *Nuclear Fusion*, 53(11):113003, Sep 2013.

[77] Y. In, J.-K. Park, Y.M. Jeon, J. Kim, G.Y. Park, J.-W. Ahn, A. Loarte, W.H. Ko, H.H. Lee, J.W. Yoo, J.W. Juhn, S.W. Yoon, H. Park, and 3D Physics Task Force in KSTAR. Enhanced understanding of non-axisymmetric intrinsic and controlled field impacts in tokamaks. *Nuclear Fusion*, 57(11):116054, Aug 2017.

[78] L. Schmitz, D.M. Kriete, R.S. Wilcox, T.L. Rhodes, L. Zeng, Z. Yan, G.R. McKee, T.E. Evans, C. Paz-Soldan, P. Gohil, B. Lyons, C.C. Petty, D. Orlov, and A. Marinoni. L–h transition trigger physics in iter-similar plasmas with applied n=3 magnetic perturbations. *Nuclear Fusion*, 59(12):126010, Sep 2019.

[79] M. Cao and P.H. Diamond. Instability and turbulent relaxation in a stochastic magnetic field. *Plasma Physics and Controlled Fusion*, 64(3):035016, Feb 2022.

[80] G.R. McKee, Z. Yan, C. Holland, R.J. Buttery, T.E. Evans, R.A. Moyer, S. Mordijck, R. Nazikian, T.L. Rhodes, O. Schmitz, and M.R. Wade. Increase of turbulence and transport with resonant magnetic perturbations in elm-suppressed plasmas on diii-d. *Nuclear Fusion*, 53(11):113011, Sep 2013.

[81] C. Bandt, G. Keller, and B. Pompe. Entropy of interval maps via permutations. *Nonlinearity*, 15(5):1595, Aug 2002.

[82] K. Keller and M. Sinn. Kolmogorov–sinai entropy from the ordinal viewpoint. *Physica D: Nonlinear Phenomena*, 239(12):997–1000, Feb 2010.

[83] F. Serinaldi, L. Zunino, and O.A. Rosso. Complexity–entropy analysis of daily stream flow time series in the continental united states. *Stochastic Environmental Research and Risk Assessment*, 28(7):1685–1708, Oct 2014.

[84] L. Zunino, M. Zanin, B.M. Tabak, D.G. Pérez, and O.A. Rosso. Complexity-entropy causality plane: A useful approach to quantify the stock market inefficiency. *Physica A: Statistical Mechanics and its Applications*, 389(9):1891–1901, 2010.

[85] E. Estevez-Rams, A. Mesa-Rodriguez, and D. Estevez-Moya. Complexity-entropy analysis at different levels of organisation in written language. *PLOS ONE*, 14(5):1–16, 05 2019.

[86] J.E. Maggs and G.J. Morales. Permutation entropy analysis of temperature fluctuations from a basic electron heat transport experiment. *Plasma Physics and Controlled Fusion*, 55(8):085015, Jun 2013.

[87] J.E. Maggs, T.L. Rhodes, and G.J. Morales. Chaotic density fluctuations in l-mode plasmas of the diii-d tokamak. *Plasma Physics and Controlled Fusion*, 57(4):045004, Mar 2015.

[88] Z. Zhu, A.E. White, T.A. Carter, S.G. Baek, and J.L. Terry. Chaotic edge density fluctuations in the Alcator C-Mod tokamak. *Physics of Plasmas*, 24(4):042301, 04 2017.

[89] J.W. Connor, R.J. Hastie, H.R. Wilson, and R.L. Miller. Magnetohydrodynamic stability of tokamak edge plasmas. *Physics of Plasmas*, 5(7):2687–2700, 07 1998.

[90] R.B. White. *The Theory of Toroidally Confined Plasmas*. World Scientific Publishing Company, 2006.

[91] R. Fitzpatrick and T.C. Hender. The interaction of resonant magnetic perturbations with rotating plasmas. *Physics of Fluids B: Plasma Physics*, 3(3):644–673, 03 1991.

[92] A.H. Boozer. What is a stellarator? *Physics of Plasmas*, 5(5):1647–1655, 05 1998.

[93] C.C. Hegna and N. Nakajima. On the stability of Mercier and ballooning modes in stellarator configurations. *Physics of Plasmas*, 5(5):1336–1344, 05 1998.

[94] C.C. Hegna and S.R. Hudson. Ideal magnetohydrodynamic ballooning stability boundaries in three-dimensional equilibria. *Physics of Plasmas*, 9(5):2014–2019, 04 2002.

[95] C.C. Hegna. Healing of magnetic islands in stellarators by plasma flow. *Nuclear Fusion*, 51(11):113017, Oct 2011.

[96] C.C. Hegna. Plasma flow healing of magnetic islands in stellaratorsa). *Physics of Plasmas*, 19(5):056101, 03 2012.

[97] Y. Zhou, N.M. Ferraro, S.C. Jardin, and H.R. Strauss. Approach to nonlinear magneto-hydrodynamic simulations in stellarator geometry. *Nuclear Fusion*, 61(8):086015, Jul 2021.

[98] S.R. Hudson and J. Breslau. Temperature contours and ghost surfaces for chaotic magnetic fields. *Physical Review Letters*, 100:095001, Mar 2008.

[99] E.J. Paul, S.R. Hudson, and P. Helander. Heat conduction in an irregular magnetic field. part 2. heat transport as a measure of the effective non-integrable volume. *Journal of Plasma Physics*, 88(1):905880107, 2022.

[100] K. Matsumoto and I. Tsuda. Noise-induced order. *Journal of Statistical Physics*, 31(1):87–106, Apr 1983.

[101] J.W. Connor, R.J. Hastie, and J.B. Taylor. High mode number stability of an axisymmetric toroidal plasma. *Proceedings of the Royal Society of London. A. Mathematical and Physical Sciences*, 365(1720):1–17, 1979.

[102] W.M. Tang. Microinstability theory in tokamaks. *Nuclear Fusion*, 18(8):1089, Aug 1978.

[103] J.W. Connor, R.J. Hastie, and J.B. Taylor. Stability of general plasma equilibria. iii. *Plasma Physics*, 22(7):757, Jul 1980.

[104] M. Kikuchi and M. Azumi. *Fundamentals of Ballooning Modes in Tokamak*, pages 157–173. Springer International Publishing, 2015.

[105] P. Ricci, F.D. Halpern, S. Jolliet, J. Loizu, A. Mosetto, A. Fasoli, I. Furno, and C. Theiler. Simulation of plasma turbulence in scrape-off layer conditions: the gbs code, simulation results and code validation. *Plasma Physics and Controlled Fusion*, 54(12):124047, Nov 2012.

[106] B.A. Carreras and P.H. Diamond. Thermal diffusivity induced by resistive pressure-gradient-driven turbulence. *Physics of Fluids B: Plasma Physics*, 1(5):1011–1017, 05 1989.

[107] P.M. Morse, H. Feshbach, and E.L. Hill. Methods of Theoretical Physics. *American Journal of Physics*, 22(6):410–413, 09 1954.

[108] F.L. Waelbroeck, J.W. Connor, and H.R. Wilson. Finite larmor-radius theory of magnetic island evolution. *Physical Review Letters*, 87:215003, Nov 2001.

[109] G. McKee, R. Ashley, R. Durst, R. Fonck, M. Jakubowski, K. Tritz, K. Burrell, C. Greenfield, and J. Robinson. The beam emission spectroscopy diagnostic on the DIII-D tokamak. *Review of Scientific Instruments*, 70(1):913–916, 01 1999.

[110] G.S. Yun, W. Lee, M.J. Choi, J. Lee, M. Kim, J. Leem, Y. Nam, G.H. Choe, H.K. Park, H. Park, D.S. Woo, K.W. Kim, C.W. Domier, N.C. Luhmann Jr., N. Ito, A. Mase, and S.G. Lee. Quasi 3D ECE imaging system for study of MHD instabilities in KSTAR. *Review of Scientific Instruments*, 85(11):11D820, 07 2014.

[111] M. Leconte, P.H. Diamond, and Y. Xu. Impact of resonant magnetic perturbations on zonal modes, drift-wave turbulence and the l–h transition threshold. *Nuclear Fusion*, 54(1):013004, Nov 2013.

[112] A.A. Vedenov, E.P. Velikhov, and R.Z. Sagdeev. Nonlinear oscillations of rarified plasma. *Nuclear Fusion*, 1(2):82, Mar 1961.

[113] W. Lee. Turbulence analysis by estimating kubo number in l-mode, h-mode, and elms-suppressed h-mode plasmas. Master's thesis, Korea Advanced Institute of Science and Technology, 2019.

[114] J.B. Taylor and B. McNamara. Plasma Diffusion in Two Dimensions. *The Physics of Fluids*, 14(7):1492–1499, 07 1971.

[115] J.B. Taylor and W.B. Thompson. Fluctuations in guiding center plasma in two dimensions. *The Physics of Fluids*, 16(1):111–117, 01 1973.

[116] D. Stauffer. Scaling theory of percolation clusters. *Physics Reports*, 54(1):1–74, 1979.

[117] D. Bernard, G. Boffetta, A. Celani, and G. Falkovich. Conformal invariance in two-dimensional turbulence. *Nature Physics*, 2(2):124–128, Feb 2006.

[118] P.S. Marcus. Jupiter's great red spot and other vortices. *Annual Review of Astronomy and Astrophysics*, 31(Volume 31, 1993):523–569, 1993.

[119] J.A. Boedo, D. Rudakov, R. Moyer, S. Krasheninnikov, D. Whyte, G. McKee, G. Tynan, M. Schaffer, P. Stangeby, P. West, S. Allen, T. Evans, R. Fonck, E. Hollmann, A. Leonard, A. Mahdavi, G. Porter, M. Tillack, and G. Antar. Transport by intermittent convection in the boundary of the diii-d tokamak. *Physics of Plasmas*, 8(11):4826–4833, 11 2001.

[120] J.A. Boedo, D.L. Rudakov, R.A. Moyer, G.R. McKee, R.J. Colchin, M.J. Schaffer, P.G. Stangeby, W.P. West, S.L. Allen, T.E. Evans, R.J. Fonck, E.M. Hollmann, S. Krasheninnikov, A.W. Leonard, W. Nevins, M.A. Mahdavi, G.D. Porter, G.R. Tynan, D.G. Whyte, and X. Xu. Transport by intermittency in the boundary of the diii-d tokamak. *Physics of Plasmas*, 10(5):1670–1677, 05 2003.

[121] T.H. Dupree. Growth of phase-space density holes. *The Physics of Fluids*, 26(9):2460–2481, 09 1983.

[122] Y. Kosuga and P.H. Diamond. Drift hole structure and dynamics with turbulence driven flows. *Physics of Plasmas*, 19(7):072307, 07 2012.

[123] A. Okubo. Horizontal dispersion of floatable particles in the vicinity of velocity singularities such as convergences. *Deep Sea Research and Oceanographic Abstracts*, 17(3):445–454, 1970.

[124] J. Weiss. The dynamics of enstrophy transfer in two-dimensional hydrodynamics. *Physica D: Nonlinear Phenomena*, 48(2):273–294, 1991.

[125] S. Ding, A.M. Garofalo, H.Q. Wang, D.B. Weisberg, Z.Y. Li, X. Jian, D. Eldon, B.S. Victor, A. Marinoni, Q.M. Hu, I.S. Carvalho, T. Odstrčil, L. Wang, A.W. Hyatt, T.H. Osborne, X.Z. Gong, J.P. Qian, J. Huang, J. McClenaghan, C.T. Holcomb, and J.M. Hanson. A high-density and high-confinement tokamak plasma regime for fusion energy. *Nature*, 629(8012):555–560, May 2024.

[126] C. Holland, A.E. White, G.R. McKee, M.W. Shafer, J. Candy, R.E. Waltz, L. Schmitz, and G.R. Tynan. Implementation and application of two synthetic diagnostics for validating simulations of core tokamak turbulence. *Physics of Plasmas*, 16(5):052301, 05 2009.

[127] C. Holland, L. Schmitz, T. L. Rhodes, W. A. Peebles, J. C. Hillesheim, et al. Advances in validating gyrokinetic turbulence models against l- and h-mode plasmas a). *Physics of Plasmas*, 18(5):056113, 05 2011.

[128] B.B. Kadomtsev. Self-organization and transport in tokamak plasma. *Plasma Physics and Controlled Fusion*, 34(13):1931, Dec 1992.

[129] T.S. Hahm and P.H. Diamond. Mesoscopic transport events and the breakdown of fick's law for turbulent fluxes. *Journal of the Korean Physical Society*, 73(6):747–792, Sep 2018.

[130] G. Dif-Pradalier, P. Ghendrih, Y. Sarazin, E. Caschera, F. Clairet, Y. Camenen, P. Donnel, X. Garbet, V. Grandgirard, Y. Munschy, L. Vermare, and F. Widmer. Transport barrier onset and edge turbulence shortfall in fusion plasmas. *Communications Physics*, 5(1):229, Sep 2022.

[131] A. Sladkomedova, I. Cziegler, A.R. Field, A.A. Schekochihin, D. Dunai, and P.G. Ivanov. Intermittency of density fluctuations and zonal-flow generation in mast edge plasmas. *Journal of Plasma Physics*, 89(6):905890614, 2023.

[132] A. Garg. *Classical electromagnetism in a nutshell*, volume 13. Princeton University Press, 2012.

[133] N. Rostoker and M.N. Rosenbluth. Test particles in a completely ionized plasma. *The Physics of Fluids*, 3(1):1–14, 01 1960.

[134] G.S. Xu, V. Naulin, W. Fundamenski, C. Hidalgo, J.A. Alonso, C. Silva, B. Gonçalves, A.H. Nielsen, J. Juul Rasmussen, S.I. Krasheninnikov, B.N. Wan, M. Stamp, and JET EFDA Contributors. Blob/hole formation and zonal-flow generation in the edge plasma of the jet tokamak. *Nuclear Fusion*, 49(9):092002, Aug 2009.

[135] M. Wakatani and A. Hasegawa. A collisional drift wave description of plasma edge turbulence. *The Physics of Fluids*, 27(3):611–618, 03 1984.

[136] O.E. Garcia, N.H. Bian, and W. Fundamenski. Radial interchange motions of plasma filaments. *Physics of Plasmas*, 13(8):082309, 08 2006.

[137] A. Hasegawa and K. Mima. Pseudo-three-dimensional turbulence in magnetized nonuniform plasma. *The Physics of Fluids*, 21(1):87–92, 01 1978.

[138] G. Veronis. On the transient response of a β-plane ocean. *Journal of the Oceanographical Society of Japan*, 14(1):1–5, 1958.

[139] G.M. Webb, C.T. Duba, and Q. Hu. Rossby wave green's functions in an azimuthal wind. *Geophysical & Astrophysical Fluid Dynamics*, 110(3):224–258, 2016.